

Hyperspectral Speckle Imaging

by

Daniel Johns

Under the Direction of Fabien R. Baron, Ph.D.

A Dissertation Submitted in Partial Fulfillment of the Requirements for the Degree of

Doctor of Philosophy

in the College of Arts and Sciences

Georgia State University

2024

ABSTRACT

Imaging objects in space is of interest to both astronomers and government agencies alike. Various government agencies are interested in maintaining situational awareness in the final frontier by direct monitoring of space-based assets. Monitoring man-made objects requires *direct* imaging techniques. However, corruption by the Earth’s atmosphere makes direct imaging more difficult. Techniques such as speckle imaging have been employed to “freeze” the atmosphere and recover the underlying object with high fidelity. State-of-the-art speckle imaging techniques, namely Multi-Frame Myopic Deconvolution (MFMD), rely on wavefront sensing to provide accurate Point-Spread Functions (PSFs) for recovery of the underlying object. First, we show successful recoveries of simulated scenes with spatially-varying PSFs. We show that, for fields once considered isoplanatic, there are considerable advantages to including anisoplanatic effects in the recovery process, such as improved accuracy on recovered flux ratios and improved object morphology. This allows for full atmospheric tomography and improves the fidelity of both on- and off-axis sources. Typically, speckle images are collected across a narrow bandpass. Here we also extend speckle imaging to a broad spectral range ($\Delta\lambda \sim 600$ nm), i.e. hyperspectral speckle imaging, using numerical simulations of broadband speckle images. This brings with it vital gains in sensitivity and improved sampling of the wavefront from chromatic effects. From this, spectral information on the target is recovered, which could pave the way for future material aging studies. Finally, to complement these numerical studies we built a suite of optical experiments to simulate turbulence and simulate wavefront sensing instruments. We also develop and deploy the ARGOS 2-channel broadband imaging instrument on the Hard Labor Creek Observatory (HLCO) 0.7m telescope with limited success.

INDEX WORDS: Speckle Imaging, Wavefront Sensing, Instrumentation, Space Domain Awareness, Hyperspectral Imaging

Copyright by
Daniel Johns
2024

Hyperspectral Speckle Imaging

by

Daniel Johns

Committee Chair:

Fabien Baron

Committee:

Stuart Jefferies

Douglas Gies

Lewis Roberts

Steve Howell

Electronic Version Approved:

Office of Graduate Studies

College of Arts and Sciences

Georgia State University

December 2024

DEDICATION

This work is dedicated to the brave Alpao DM-97 that lost its life during my pursuit of scientific greatness. May all your wavefronts be flat in the afterlife...

ACKNOWLEDGMENTS

“What a long strange trip it’s been.”

– Pam Beesly, *The Office*

First, I’d like to thank my graduate advisors, Fabien Baron and Stuart Jefferies, for guiding me through this process, always going out of their way to answer my silly questions, meeting at odd hours when needed, and, most importantly, providing me the opportunity to work on this exciting, novel research. What I thought was going to be a simple visit to the optics lab has turned into this dissertation, and now, my career. Thank you to Dmitriy for helping me out in the lab and fighting the SLMs with me when they were misbehaving. Without my undergraduate advisor, Phill Reed, I would not be the astronomer I am today. He believed in me, gave me so many opportunities to thrive as a budding astronomer, and encouraged me to shoot for the stars. Without his encouragement I wouldn’t be where I am today. For that, I am eternally grateful.

To my fellow grad students, I’d like to thank you for the camaraderie, support, and unforgettable memories we made along the way. I’d like to especially thank my cohort: Emma, Julian, Fallon, Aman, and Varun. I’ve never met a funnier, more adventurous crew in my life. From Shrek Raves to daily cubicle chats to jumping out of airplanes, you guys are truly a different breed. To Caleb, without your mentorship I never would have gained my footing in the lab. Finally, to Leti, having you in the lab was truly a blast, from watching Roland Garros in the lab to chatting about anything and everything when

we got bored/frustrated. You challenged me as a mentor and pushed me to a deeper level of understanding.

Of course, none of this would be possible without the support of my family. My parents, Bill and Mary-Ellen, inspired me to work hard to achieve my dreams. After many long years, those dreams have become reality. For the lifelong love and support, I owe you guys everything. To Jess, Elliot, and Oaklynn, no matter where I am I know you guys will always be there for me, ready to take an impromptu road trip or plan an elaborate prank on the parents.

There are so many friends that kept me afloat throughout this process. First, my lifelong best friends John and Jordan. From kindergarten to now, you guys have always had my back and I truly couldn't have made it this far without you guys. Jake Clark, my brother from abroad, thank you for showing me that you can still crunch numbers by day and mosh and stage dive by night as an academic. To all the lovely people I met at the dog park, thank you for keeping me sane during the pandemic! Bridget, I don't think I'd have survived grad school without you. Between our late night drives through the city, our kayak trips to Stone Mountain, and our nights sitting in the dark watching American Horror Story, you truly brought a relieving light when things were tough and I can't think of anyone else I'd want in my corner. Finally, to my best boys Onyx and Arthur, all of the puppy snuggles and dog park trips made the days so much more enjoyable.

This material is based upon work supported by the Air Force Office of Scientific Research under award numbers FA9550-14-1-0178 and FA9550-21-1-0384, and award number FA9550-

21-1038 under the Defense University Research Instrumentation Program (DURIP). Any opinions, findings, conclusions, or recommendations expressed in this material are those of the authors and do not necessarily reflect the views of the United States Air Force. A portion of this research was funded by the Jet Propulsion Laboratory, California Institute of Technology, under a contract with the National Aeronautics and Space Administration (NASA).

TABLE OF CONTENTS

ACKNOWLEDGMENTS	v
LIST OF TABLES	xi
LIST OF FIGURES	xii
LIST OF ABBREVIATIONS	xviii
1 Introduction	1
1.1 Speckle Imaging	3
1.2 Astronomical Instrumentation	7
1.2.1 <i>Basic Components of an Optical System</i>	7
1.2.2 <i>Wavefront Manipulation</i>	12
1.3 Summary of Projects	15
2 Speckle Imaging of Scenes with Spatially-Varying PSFs	16
2.1 Introduction	16
2.2 Two-channel Speckle Imaging System	22
2.2.1 <i>Separation of Atmospheric Layers</i>	24
2.2.2 <i>Estimation of Layer Heights</i>	27
2.3 Reconstruction Method	29
2.3.1 <i>Deconvolution</i>	31
2.3.2 <i>Height Solver</i>	33
2.4 Simulated Observations	34
2.5 Results	36
2.6 Conclusions and Discussion	40
2.7 Table of Variables	43

3 Hyperspectral Speckle Imaging of Resolved Targets	46
3.1 Introduction	46
3.2 Numerical Simulations	48
3.3 Analysis Method	56
3.4 Results	60
3.5 Discussion & Conclusion	66
3.6 Table of Variables	70
4 Optics Experiments for Speckle Imaging	72
4.1 Advanced Reconnaissance of Earth-orbiting Satellites (ARES) Turbulence Simulator	72
4.1.1 Optical Design	73
4.1.2 Phase Wraps	76
4.1.3 Zero-Order Diffraction Spot (ZODS) Removal and Spatial Light Modulator (SLM) Flattening	76
4.1.4 Performance	80
4.2 SLM as an Imaging Shack-Hartmann (ISH)-Wavefront Sensor (WFS)	82
4.3 ARGOS 2-Channel Broadband Speckle Imager	85
4.3.1 Optical Design	85
4.3.2 Preliminary Results & Current Limitations	88
4.4 Table of Variables	93
5 Discussion, Conclusion, and Future Work	94
5.1 Closely Spaced Objects (CSOs)	94
5.2 Extension to 30 m Class Telescopes	96
5.3 Hybrid Optical Telescope Concept	97
5.4 Improvements to MFBD.jl	99
5.5 On-Sky Speckle Imaging Validation	101

5.6 Polychromatic Turbulence Generation	102
APPENDIX	104
A Analytic Gradients	104
REFERENCES	109

LIST OF TABLES

Table 2.1 Simulated Atmospheric and Detector Parameters	35
Table 2.2 Root Mean Square Error (RMSE) and SSIM _s values for each experiment. “Isoplanatic” and “anisoplanatic” here refer to the way the data are treated.	37
Table 2.3 Recovered flux ratios using different size windows (in pixels) around each source for the binary system at 3” and 20” separation.	40

LIST OF FIGURES

Figure 1.1 Taken from [1]. Shows the total number of space objects per year (black) between 1957–2022, broken down by active spacecraft (blue), dead spacecraft (red), leftover object (green), and space debris (grey).	2
Figure 1.2 Example atmospheric PSF showing speckles. These speckles retain diffraction-limited information.	5
Figure 1.3 Overview of mirror coatings from Edmund Optics.	12
Figure 1.4 Overview of anti-reflective lens coatings from Thorlabs.	13
Figure 2.1 Simple diagram displaying how tomography with a resolved source is enabled through the use of a scene-based Shack-Hartmann wave front sensor. See main text for details.	25
Figure 2.2 RMSE, in units of intensity, between atmospheric PSFs at two field points as a function of angular separation in units of arcsec ("") and number of isoplanatic angles ($\theta_0 = 2.97''$ for $r_0 = 18$ cm at 500 nm; Eqn. 2.1). The insets show the PSFs at the two extremes of the curve. In the 1" case the PSFs are visually indistinguishable. Differences are clearly seen between PSFs in the 20" case. These RMSE values are the ensemble average of 50 realizations of the atmosphere.	28
Figure 2.3 An example of how the error metric changes with the heights of the layers during the height solve part of the analysis. Here we use a 3-layer model to simulate observations. The layers are initially set at $h = 0$ km, with the lowest wind velocity layer fixed at ground height throughout the entire analysis. The layer with the highest wind velocity is varied first (blue triangles) and is assumed to be the high-altitude layer between 10 – 20 km. Then, the layer is fixed to the height that provides the lowest criterion value. Next, the mid-altitude layer is allowed to vary in height (red squares) between 5 – 10 km. Finally, with both layers at their respective heights the process is repeated. These results are without tip/tilt estimation on each layer.	30
Figure 2.4 Recoveries of a high-contrast binary ($F_{sec}/F_{pri} = 10^{-2}$) at 3" separation. The recovery with the isoplanatic model (bottom left) and with the anisoplanatic treatment of the data (bottom right) are shown against the ground truth (top left) and an example data frame (top right). All images are on a logarithmic scale.	38

Figure 3.4 The top row shows the truth object for five selected wavebands from the 20 wavebands that were used to build the broadband images. The middle row presents the corresponding theoretical diffraction-limited resolution images. The bottom row depicts the recovered objects from simulated ground-based observations taken at zenith, through a combined atmospheric turbulence of $D/r_0 = 21$. The ground-based observations incorporate Gaussian read noise ($\sigma_{RN} = 2 e^-$), shot noise for a magnitude +4 target brightness, and the restoration used estimated wavefronts from a Shack-Hartmann wavefront sensor. The recovery process reduces this wavefront error from 0.33 rad in the composite wavefront to 0.22 rad at 500 nm. The RMSE and SSIM, computed using Eqn. 3.8 and 3.9, respectively, are shown to the upper right of the recovered object at each wavelength.

61

Figure 3.5 Power spectrum of the truth object (left), recovered object (center), and diffraction-limited object (right) at wavebands 400 – 430 nm (top row), 685 – 715 nm (center row), and 970 – 1000 nm (bottom row) for observations taken at zenith with Gaussian read noise, shot noise, and with degraded wavefronts. The cutoff frequency at each wavelength is plotted in all three plots as a yellow circle. Within the cutoff frequency, we are recovering spatial frequencies in the object to their true amplitudes. Additionally, we see some meaningful recovery of spatial frequencies outside of the cutoff frequency. However, the discrepancies between the true and recovered spatial amplitudes increase with wavelength, particularly near and beyond the cutoff frequency. This is due to the reduction in spatial information available in the data as the wavelength increases. These discrepancies lead to artifacts in the recovered morphology, which in turn result in errors in the recovered spectra.

62

Figure 3.6 Recovered spectrum of each pixel in the object at 20 wavelengths (solid line) for noisy frames, degraded wavefronts, and observations at zenith ($\eta = 0^\circ$). The bottom half of the satellite is shown on the left and the top half on the right. Truth spectra are shown as dashed lines (and in the right panel of Fig. 3.2). Colors correspond to the materials in Fig. 3.2. Discrepancies in the recovered spectra around the bus of the satellite (center of figure) are the result of spatial mixing of adjacent pixels. Mixing increases towards larger wavelengths due to the loss in resolution.

64

Figure 3.7 Mean, recovered material reflectance for observations taken at zenith angle $\eta = 0^\circ$ where the frames are corrupted by read noise and shot noise, and the initial wavefronts estimates possess 0.332 ± 0.004 rad of wavefront error at 500 nm when compared to the truth. The initial wavefront estimates are updated in the recovery process and contain 0.217 ± 0.009 rad wavefront error at 500 nm at the end of the recovery process. The recovery was performed for $N_\lambda = 20$. These spectra are obtained by averaging all of the pixel spectra for each material and removing the solar spectrum and QE curve. The shaded region represents the standard-deviation of the mean RMSE for recoveries made with four different time series of data, each performed with $N_t = 102$. The truth spectra are shown by the dashed lines and the theoretical diffraction limited results for a 5-channel multi-spectral imager are shown as dotted lines with star markers.

65

Figure 3.8 Recovered object at 5 wavebands for observations taken at $\eta = 30^\circ$ with both Gaussian read noise and shot noise present, and with degraded wavefronts. The top row shows the truth object, the middle row shows the recovered object when dispersion is not corrected-for at the detector, and the bottom row shows the recovered object when a dispersion corrector is used. The RMSE and SSIM, computed using Eqn. 3.8 and 3.9, respectively, are shown to the upper right of each recovered object slice.

66

Figure 3.9 Mean, recovered material reflectance for observations taken at zenith angle $\eta = 30^\circ$ where the frames are corrupted by read noise and shot noise, and the initial wavefronts estimates possess 0.33 rad of wavefront error at 500 nm when compared to the truth. The initial wavefront estimates are updated in the recovery process and contain 0.21 rad wavefront error at 500 nm at the end of the recovery process. The recovery was performed for $N_\lambda = 20$. These spectra are obtained by averaging all of the pixel spectra for each material and removing the solar spectrum and QE curve. The truth spectra are shown by the dashed lines and the theoretical diffraction limited results for a 5-channel multi-spectral imager are shown as dotted lines with star markers.

67

Figure 4.1 Laser module that feeds ARES, composed of two lasers, one of which is on a translation stage to change the separation between sources.

74

Figure 4.2 Schematic of the ARES turbulence generator. The key components of ARES are SLM1 and SLM2, acting as the high altitude layer and ground layer of turbulence, respectively. The optical trombone, M2–M5, set the height of the upper layer.

75

Figure 4.3 ARES on the optical bench.

77

Figure 4.4 Comparison of the expected results without (top row) and with (bottom row) amplitude variations from phase wraps for 8 waves of defocus. The phase screens can be seen in the first column and the amplitudes are seen in the second column. The third column shows the simulated PSF formed by these phases and amplitudes and column four shows the common logarithm of the PSF. Finally, the last column shows the common logarithm of the fractional difference between the two PSFs (top) and a histogram of the logarithmic fractional differences (bottom).	78
Figure 4.5 Removal of the ZODS with defocus. Left shows the PSF from ARES with the ZODS present (within the red box). The center image shows the result of adding defocus to the phase screens. The right image shows the computer-generated PSF for comparison to evaluate any degradation in fidelity as a result of adding defocus.	79
Figure 4.6 The static phase in units of radians recovered at SLM1 and SLM2 using a phase diversity process.	81
Figure 4.7 Comparison of the observed PSF at each stage of flattening, starting with the simulated diffraction-limited PSF for an ideal system, then moving to the observed PSF before flattening, the PSF after flattening SLM1, and finally after flattening both SLMs 1 and 2. Each image is shown on a square-root scale. The RMSE between the simulated PSF and each observed PSF is shown in the upper right corner of each plot, in units of 10^{-4} intensity units.	81
Figure 4.8 Simulated (top row) vs observed (bottom row) PSFs generated with ARES for 1 atmospheric layer. PSFs are generated at D/r_0 values from 5–80, going from left to right. Images are thresholded so that the bright spot from phase wraps does not drown out the structure of the atmospheric PSF.	82
Figure 4.9 SSIM vs D/r_0 for the set of simulated and observed PSFs generated with ARES.	83
Figure 4.10 6×6 Fresnel lenslet array placed on the SLM to simulate a microlens array.	84
Figure 4.11 (left) Shows an example of a pupil-plane intensity image showing the amplitude variations from phase wrapping in the turbulent phase screens. (right) Shows a set of example lenslet images generated from the turbulent phase screens.	84
Figure 4.12 ARGOS 2-channel broadband speckle imager optical schematic.	86
Figure 4.13 ARGOS 2-channel imager attached to the Nasmyth port of the HLCO Planewave CK700 telescope.	88

Figure 4.14 Full-aperture data frame (left) and ISH data frame (right) of Vega acquired with the 2-channel broadband speckle imager on 24 August 2024. .	89
Figure 4.15 Full-aperture data frame (left) and ISH data frame (right) of Saturn acquired with the 2-channel broadband speckle imager on 22 September 2024. .	90
Figure 5.1 (left) The recovered morphology of the main satellite and the CSO to the lower right on a logarithmic scale. (right) The recovered spectrum of the CSO at 101 wavelengths.	95
Figure 5.2 Dark hole generated with a Hybrid Optical Telescope (HOT) aperture and SLM. The first column shows the computer generated diffraction-limited PSF with a dark hole indicated by the red arrow. This PSF is generated by performing a Zernike decomposition of the PSF with the hole and selecting the first 40 Zernike modes to reconstruct the phase. The middle column shows the observed PSF on the optical bench using this reconstructed phase. The final column shows the same PSF but with correction for static phase on the SLM, using the procedure given in Sec. 4.1.3. The first row shows the case of a single point source and the second row shows the case of a fainter secondary source within the dark hole. Finally, the numbers in the lower right corner of each plot are the contrast between the flux in the central spike of the PSF and the flux within the dark hole.	98

LIST OF ABBREVIATIONS

AO	Adaptive Optics
ARES	Advanced Reconnaissance of Earth-orbiting Satellites
CSO	Closely Spaced Object
DM	Deformable Mirror
EFF	Efficient Filter Flow
FOV	Field of View
FWHM	Full Width Half Max
GEO	Geostationary Orbit
GSU	Georgia State University
HLCO	Hard Labor Creek Observatory
HOT	Hybrid Optical Telescope
ISH	Imaging Shack-Hartmann
LEO	Low Earth Orbit
MEO	Medium Earth Orbit
MFBD	Multi-Frame Blind Deconvolution

MFMD	Multi-Frame Myopic Deconvolution
MLA	Micro Lens Array
OAP	Off Axis Parabola
OPD	Optical Path Difference
OTF	Optical Transfer Function
PSF	Point-Spread Function
QE	Quantum Efficiency
RMSE	Root Mean Square Error
RSSS	Remote Sensing for Space Sciences
SDA	Space Domain Awareness
SH	Shack Hartmann
SNR	Signal-to-Noise Ratio
SLM	Spatial Light Modulator
SSIM	Structural Similarity Index Measure
VMLMB	Variable Metric Limited Memory Bound
WFS	Wavefront Sensor
ZODS	Zero-Order Diffraction Spot

CHAPTER 1

Introduction

In the 1950s, we as a society made the first steps to explore the vast unknown that surrounds the Earth with the launch of Sputnik 1. Since then, humanity has set foot on the Moon, sent landers to Venus and rovers to Mars, and sent advanced instruments to the other planets and bodies in the Solar system. Additionally, we have chosen to enrich our day-to-day lives by connecting people and systems with wireless technology, such as the GPS for navigation and satellite TV for entertainment, among other things. In the military world, satellite technology helps maintain communication and situational awareness by relaying meteorological information to ground-based units, feeding military intelligence with satellite imagery, and by connecting remote operators to their far-away peers. Given the vast range of capabilities brought by satellite technology, it is of utmost importance to the common person, private corporations, and the military that these satellites are monitored and protected. This task makes up the field of Space Domain Awareness (SDA). According to the United Nations Office for Outer Space Affairs' Online Index of Objects Launched into Outer Space¹, there are over 13,000 satellites in orbit providing a variety of services and taking a variety of measurements, as of September 2024. All of these spacecraft have a finite shelf life, meaning that they could one day become a hazard to active satellites if they become inoperable or reach their end-of-life. As is seen in Fig. 1.1, the presence of space debris has increased significantly in recent decades, posing an ever-increasing threat as we launch more objects into orbit. These space objects are distributed into several different orbital

¹https://www.unoosa.org/oosa/osoindex/index.jspx?lf_id=

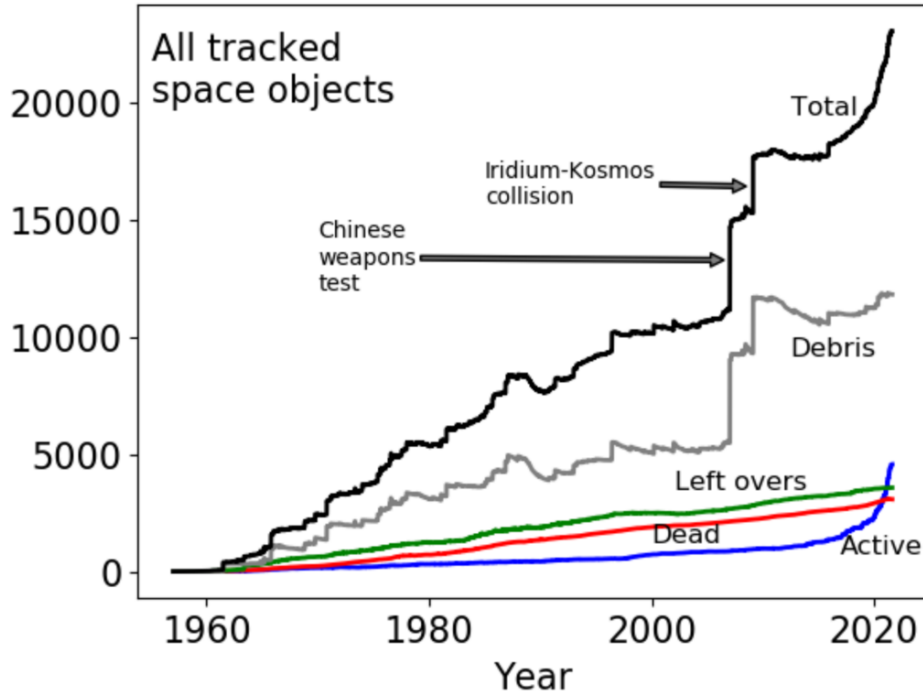


Figure 1.1 Taken from [1]. Shows the total number of space objects per year (black) between 1957–2022, broken down by active spacecraft (blue), dead spacecraft (red), leftover object (green), and space debris (grey).

regimes, namely Low Earth Orbit (LEO) (~ 300 km– 2000 km), Medium Earth Orbit (MEO) (~ 2000 km– $35,000$ km), and Geostationary Orbit (GEO) ($\sim 35,786$ km). Further regimes, such as Cislunar orbits and orbits at Lagrange points, are also of interest. LEO, however, is becoming increasingly crowded, most notably by the Starlink family of spacecraft, signaling an urgent need for accurate monitoring of this space. Compared to other orbital regimes, satellites in LEO will appear brightest in the visible when reflecting incident sunlight and will have the largest angular extent in the night sky due to their relatively-close proximity to Earth. For reference, a satellite measuring 15 m in length in LEO would appear $1.5''$ – $10''$ in extent, depending on orbital distance, while the same satellite in GEO would measure $0.08''$

in extent. This means that satellites in LEO are likely resolvable from the ground, where the diffraction limit of a 1 m telescope at 500 nm is roughly 0.13''. However, as will be explained in the next section, ground-based observatories rarely operate at this resolution and suffer at the hands of Earth's turbulent atmosphere.

1.1 Speckle Imaging

Those interested in observing, whether natural or man-made objects, must reconcile the fact that their observations will be corrupted by Earth's atmosphere. Variations in density, temperature, and pressure in the atmosphere cause variations in the index of refraction across the volume of air above the observer. When light traverses this volume and reaches a detector it is no longer the same as was when it first reached Earth's atmosphere. Turbulent cells each distort the incident wavefront independently, causing the beam of light to be spread around the detector on the ground. A telescope's theoretical resolution, or its diffraction-limit resolution, goes as $\theta \propto \frac{\lambda}{D}$ where θ is the angular resolution of the telescope, λ is the wavelength of light, and D is the diameter of the telescope. However, long exposure images under the effects of turbulence, i.e. seeing-limited conditions, experience a reduced resolution that goes as $\theta \propto \frac{\lambda}{r_0}$ where r_0 is the Fried parameter and describes the size of the turbulent cells, with 0.10 cm being typical in the visible for a site with favorable conditions [3]. For context, the strength of the turbulence is sometimes reported as D/r_0 , where D is again the diameter of the telescope. As can be seen, for any telescope above a few tens of cm in diameter there is an appreciable loss in angular resolution. For example, an 8 m

class telescope under 1" seeing conditions will have the same effective angular resolution as a 10 cm amateur telescope at 500 nm. Luckily, [3] theorized that the atmosphere is effectively frozen over short timescales, the coherence time τ_0 , typically on the order of a few ms for visible light. This simple fact provides a very powerful means for achieving high angular-resolution imagery. Since the atmosphere is considered frozen over these timescales, exposures below the coherence time of the atmosphere actually *preserve* diffraction-limited information captured by the telescope in the form of "speckles", or diffraction-limited images of the source (e.g., Fig. 1.2) that arise from interference between the waves passing through each turbulent cell. These speckles can then be used to infer the underlying object and even the atmospheric distortions that produced the final, scrambled image. Below we will introduce the ideas behind Fourier optics and how they can be used to unscramble the target from the atmosphere that it was observed through [4].

Fourier optics describes optical systems using Fourier analysis and fully capitalizes on the wave-like nature of light. In Fourier optics an image I is formed by the convolution of an object O with the system's Point-Spread Function (PSF), as in Equation 1.1 below.

$$I = O \odot PSF , \quad (1.1)$$

where \odot is the convolution. The PSF describes how the light of a point source passing through the optical system is disbursed and spread on a detector. The spatial frequency content of the PSF can be computed by taking its Fourier transform, known as the Optical

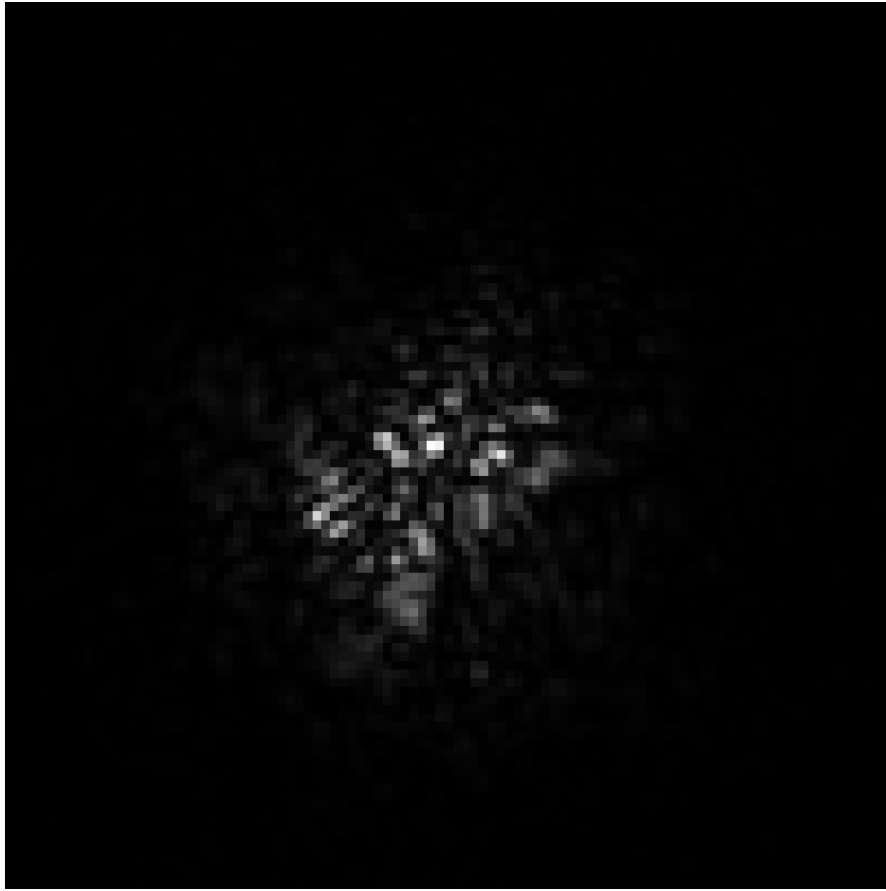


Figure 1.2 Example atmospheric PSF showing speckles. These speckles retain diffraction-limited information.

Transfer Function (OTF), given by

$$OTF = F(PSF) . \quad (1.2)$$

The PSF of a perfect system, i.e., a diffraction-limited system, with a circular aperture and no central obscuration is given by the Airy function. Optical systems are not perfect, however, and typically have aberrations present that distort the PSF. These aberrations are described by a wavefront propagating through the optical system. Since light is composed

of orthogonal, propagating electric and magnetic fields, we describe the incident wavefront using a complex-valued “pupil” function, given by $P = Ae^{i\phi}$, where A and ϕ refer to the complex amplitude and phase, respectively, of the wavefront. Finally, the phase of the pupil function is related to a change in the optical path by $\phi = 2\pi \cdot \frac{W}{\lambda}$, where W is the Optical Path Difference (OPD) in units of length and λ is the wavelength of the wavefront. This pupil function can be linked to the OTF by its autocorrelation, or

$$\begin{aligned} OTF &= P \otimes P \\ &= F(|F^{-1}(P)|^2) \text{ (Wiener-Khinchin Theorem)} , \end{aligned} \tag{1.3}$$

where \otimes is the correlation operator and in the second line we utilize the convolution theorem to express the correlation in terms of Fourier transforms [5]. Combining equations 1.2 and 1.3 allows us to express the PSF as

$$PSF = |F^{-1}(P)|^2 . \tag{1.4}$$

This Fourier description of image formation is useful because any aberrations to the wavefront can be described as a change in the phase and amplitude of the complex wavefront. Computationally, Fourier transforms are also relatively inexpensive compared to the full correlation and convolution computations. We will exploit this throughout the rest of this dissertation. From here, the task becomes “deconvolution” of the object and PSF from a set of intensity measurements. This is usually done in two separate steps where the object and PSF are solved-for separately. When expressing the PSF using the Fourier optics formulation in Eqn. 1.4, the step of recovering the PSF from images is known as phase

retrieval [6] and has been tackled in many disciplines such as astronomy [7], crystallography [8], and medical imaging [9]. In this work, we solve the phase retrieval problem using a gradient-descent approach, where images are modeled using Eqn. 1.1 and the discrepancy between the measured and model images is numerically minimized. Chapter 2 introduces additional measurements from a Wavefront Sensor (WFS) to help constrain the PSFs and Chapter 3 extends the idea of speckle imaging to observations taken over a wide passband.

1.2 Astronomical Instrumentation

Advancements in the field of astronomy are not only dependent on the algorithms used to reduce and analyze the data, but also on the instruments used to collect the data. The way that data are collected needs to match the goals of the observing campaign. Because of this, new instruments are continuously created and developed to meet specific needs. Here, we will describe the basics of astronomical instrumentation as it applies to this work. This should not be taken as an exhaustive guide to optics but rather as a starting point for basic astronomical instrumentation.

1.2.1 Basic Components of an Optical System

An astronomical instrument is typically made up of an arrangement of basic optical components. These components are carefully selected for the conditions they will be operating in. Monochromatic optical systems are typically simpler to understand, and so we will focus on the components of these systems first. The most basic components are plane mirrors and lenses. Plane mirrors reflect an incident beam such that the angle of incidence is equal to

the angle of reflection. This is useful for beam steering, folding very long optical setups, and adding optical path length to a design.

Next, lenses are used to change the convergence properties of a beam by introducing refraction from a glass substrate. The distance at which a lens will form an image is determined by the equation

$$\frac{1}{f} = \frac{1}{d_o} + \frac{1}{d_i}, \quad (1.5)$$

where f is the focal length of the lens, d_o is the distance of the object from the lens, and d_i is the distance that the image is formed from the lens. Depending on the nature of the lens and imaging system, the object or image distance could be negative, resulting in a “virtual” image that cannot be projected onto a detector. The final image will not always be the same size as the original object, leading to some magnification, given by

$$M = -\frac{d_i}{d_o}. \quad (1.6)$$

The sign of Equation 1.6 determines the orientation of the image relative to the optical axis, where a negative sign indicates an inverted image formed below the optical axis. In the context of Fourier optics, lenses also have the powerful ability to perform Fourier transforms between collimated and focused beams. This means that an instrument can be built to inspect and manipulate a beam in the spatial domain (object plane) or the Fourier domain (focal plane), which can be achieved by imparting some phase (or Optical Path Difference (OPD)) on the beam. This will be exploited heavily in the next section. Lenses are typically used in pairs to relay the aforementioned “planes” to different points throughout our optical

system. The simplest relay system is called a 4f relay, where two lenses are separated by the sum of their focal lengths. An object placed before the first lens will form an image after the second lens such that the distance from object to image is $f_1 + f_1 + f_2 + f_2$, hence the name “4f”. A collimated input beam will maintain its collimation and will not have experienced any optical propagation. This is useful for relaying the *pupil* plane of the beam from one location to another. A diverging input beam will converge at the focal length of the second lens, allowing the user to relay the *focal* plane of the beam from one location to another. The 4f relay also allows for tight control over the magnification of the system, where magnification is given by

$$M = \frac{f_2}{f_1} , \quad (1.7)$$

where f_1 and f_2 are the magnifications of the first and second lens, respectively. Notice that this magnification is not dependent on the distance of the object to the first lens or the distance from the second lens to the final image, whereas Equation 1.6 requires precise distance measurements to achieve a specific magnification.

An important component that is made up of simple lenses is the Micro Lens Array (MLA). MLAs come in arrays of round lenses or square lenses and are typically characterized by their lens pitch, or the center-to-center distance between lenslets, and their focal length. They are one of the basic components of a Shack Hartmann (SH) wavefront sensor where the pupil plane of the beam is relayed onto the MLA, each lenslet samples a small portion of the wavefront, and each lenslet forms its own image. These lenslet images can then be analyzed to glean information on the incident wavefront. In a typical Adaptive Optics (AO) system,

the displacement of each lenslet image is used to infer the local slope of the wavefront in real time. We will see in Chapter 2 how these lenslet images can be analyzed in post processing to recover high-fidelity wavefronts and in Chapter 4 how to build an instrument around this concept.

Polarization control is also important to many optical systems. The two components most responsible for polarization control are the linear polarizer and the half-wave plate. Linear polarizers act to filter out non-linear polarization states (i.e. circular, elliptical) while half-wave plates act to rotate the polarization vector of the incident beam by a given angle. Polarization control will be revisited in the next section where certain instruments require a given polarization state to function properly.

When operating over a broad spectral range, careful consideration to the optics used must be given. Lenses operate through the process of refraction, which is itself a wavelength-dependent process. Thus, achromatic lenses aim to reduce the change in focal length with wavelength. A typical achromatic doublet, a pair of lenses cemented together, may present millimeters of focal length shift along the optical axis at wavelengths far from the design wavelength. For applications where tight focus must be maintained over a large spectral range, achromatic doublets may not suffice. For applications where tight focus is needed and obscurations along the optical axis are prohibited, an Off Axis Parabola (OAP) may be preferred. OAPs are formed from a segment of a parent parabola and focus rays off-axis at the focus of the parent parabola. OAPs can either be used to collimate a diverging beam or focus a collimated beam.

Often situations arise when one beam must be shared among several “legs” of an instrument, each manipulating the beam in a different way. For these applications a beam splitter is typically used. Beam splitters split the beam by transmitting a certain percentage of the beam’s power and reflecting the rest (with a small amount of loss in the process). Beam splitters are typically characterized by their ratio of reflected power to transmitted power, with ratios of 50:50, 30:70, 10:90, and the reciprocals of each being common examples. These beam splitters do not discriminate by wavelength. For applications where this behavior is desired, a dichroic beam splitter is used. Dichroic beam splitters transmit light above a chosen wavelength, the “cut-on” wavelength, and reflect light below the cut-on wavelength. This is useful when red and blue light need to be separated and manipulated in different ways, as we will do in Chapter 4.

All of these optical components come with their own choice of reflective coatings (for mirrors) or anti-reflective coatings (for lenses). Each manufacturer’s coating varies slightly (see Fig. 1.3 for an overview of mirror coatings) but in general when it comes to mirrors the standard metallic coatings are aluminum, silver, and gold. Aluminum coatings are great for general-purpose operations in the visible region of the electromagnetic spectrum, degrading in performance at wavelengths longer than ~ 600 nm. Silver coatings have a much broader range of reflectance, typically showing high reflectance from ~ 450 nm well into the far infrared ($\sim 12.5 \mu\text{m}$). Finally, gold coatings are well-equipped for operations in the infrared, picking up around 800 nm and extending well into the far infrared ($\sim 12.5 \mu\text{m}$). Lens coatings are designed to reduce reflection of certain wavelengths and are much less standardized than

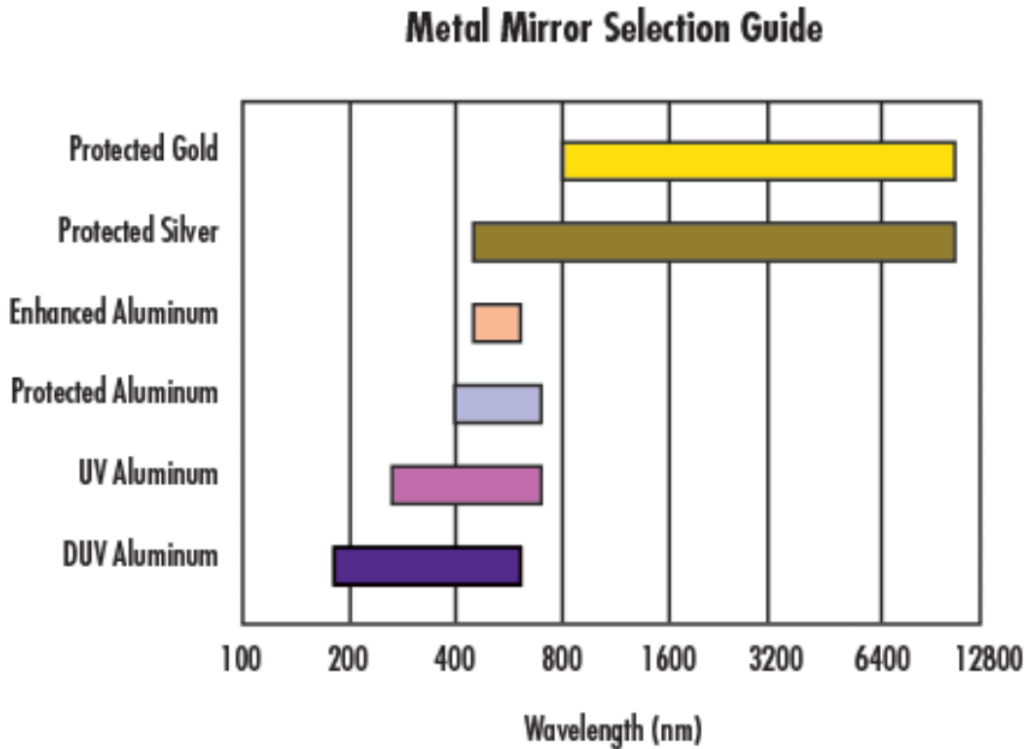


Figure 1.3 Overview of mirror coatings from Edmund Optics.

mirror coatings. Each manufacturer designs their own lens coatings but, in general, these coatings are designed to reduce reflections within a certain wavelength range. Reflectance curves for twelve Thorlabs anti-reflective coatings can be seen in Fig. 1.4. We will see in Chapter 4 that knowing the coatings of your optics is important in both the design and operation of our instruments, as well as the reconstruction of broadband images.

1.2.2 Wavefront Manipulation

Shaping light can be achieved using specialized pieces of equipment that can change the phase of light in one way or another. First, the simplest way to impart a phase change on

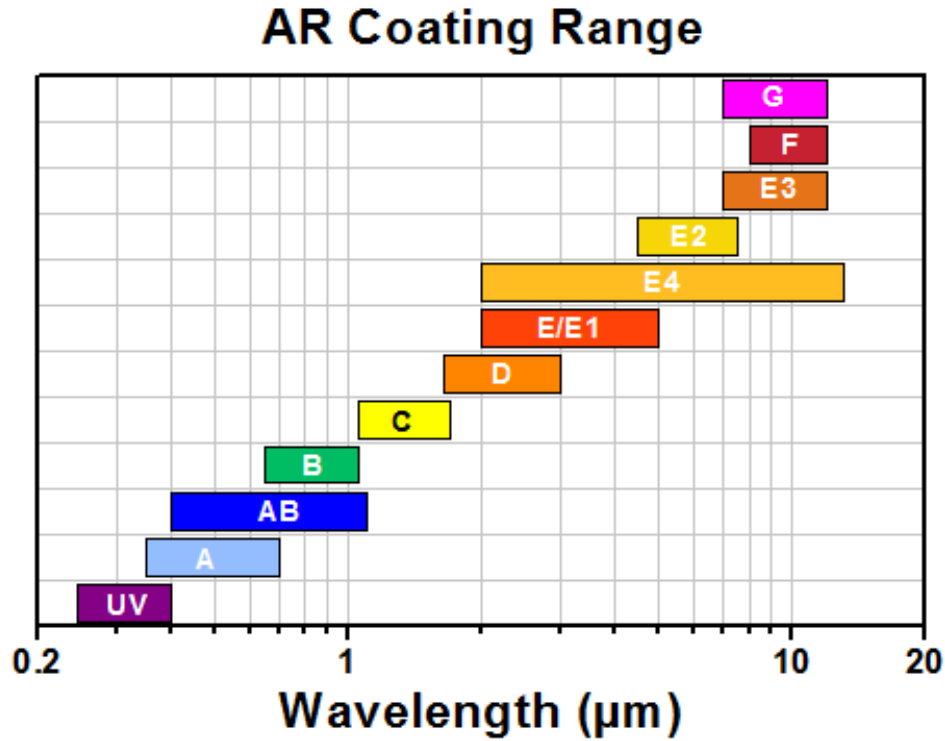


Figure 1.4 Overview of anti-reflective lens coatings from Thorlabs.

the incident wavefront is by change the optical path length across the beam. This is achieved using a Deformable Mirror (DM). DMs are made of a reflective membrane with an array of actuators behind it to impart some piston (or OPD). The performance of a DM is limited by the number of actuators across the pupil and the maximum stroke that an actuator can move, with the number of actuators across the pupil typically being in the single-digits to low double-digits and the typical actuator stroke being tens-of-microns. Larger actuator stroke means that larger spatial frequencies can be manipulated across the beam, whereas more actuators across the beam mean that finer details in the wavefront can be manipulated. There is usually a trade-off between number of actuators and actuator stroke when selecting a DM. Typically, DMs are coupled with a WFS to form an AO system. Typically, the

WFS contains an MLA that partitions the wavefront into small sections. The main idea is that the MLA measures distortions in the wavefront and the DM applies a correction in a feedback loop. More actuators across the pupil mean that *finer* distortions (i.e., high spatial frequencies) in the wavefront can be corrected and larger actuator strokes mean that *stronger* distortions (i.e., large OPDs) can be corrected. The advantage of DMs is that they directly impart an OPD on the wavefront, meaning they behave predictably over a broad spectral range.

For applications where finer control of the wavefront is needed than what a DM supplies, a Spatial Light Modulator (SLM) may be preferred. SLMs are made of liquid crystals on silicon that change orientation with voltage, which changes the index of refraction in a pixel, leading to a change in phase. They typically have much finer resolution than DMs, with micron-sized pixels and a much larger *number* of pixels (compared to actuators for a DM), usually of the order 1920×1152 pixels. They can be changed dynamically and only require a bitmap image to be uploaded to the device containing the “phase screen” that will be imparted on the beam. Since these devices function by imparting phase directly, they are only suitable for monochromatic operations and are calibrated to work at one wavelength. They also require the incoming beam to be linearly polarized such that the polarization vector is aligned with the preferred axis of the SLM. SLMs also have dead space between pixels that reflect incident light. This causes a bright spot in the PSF to appear, called the Zero-Order Diffraction Spot (ZODS). SLMs also have some curvature in their coverglass, meaning that a flat incident wavefront will leave with this curvature imprinted on it that

must be corrected for optimal performance. We will see in Chapter 4 how we mitigate the ZODS and “flatten” our SLMs.

1.3 Summary of Projects

The projects in this dissertation are related to the theme of high resolution imaging, specifically through the technique of speckle imaging. Chapter 2 involves speckle imaging reconstructions over scenes with spatially-varying PSFs. Chapter 3 shows the application of hyperspectral speckle imaging for SDA. Finally, Chapter 4 shows several projects in instrumentation to support the numerical work of the previous chapters.

CHAPTER 2

Speckle Imaging of Scenes with Spatially-Varying PSFs

2.1 Introduction

Imaging is one of the cornerstones of astronomical research, and the quest for images with increased resolution and contrast is ongoing. For example, high-contrast imaging is required for direct imaging of exoplanets [10–13], proto-stellar disk observations [14–16], and the analysis of jets from stellar sources [17, 18]. At the same time, high-resolution imaging is needed for studying close binary systems [19] and microlensing [20]. The former allows us to estimate the mass and orbits of stars accurately [21], which underpins research in stellar evolution, while microlensing observations can provide constraints on dark matter and cosmology [22].

Speckle imaging is a technique developed in the 1970s [23] that allows astronomers to overcome the image blur caused by the Earth’s turbulent atmosphere when viewing celestial objects by effectively freezing the atmosphere during an exposure. The approach fell out of favor in the late 1990s and early 2000s as adaptive optics (AO) became more mainstream and an increasing number of telescopes were equipped with AO systems. However, with the advent of EMCCD cameras, the use of speckle imaging is undergoing a resurgence [24]. This resurgence should also benefit from the recently demonstrated high-quality performance of speckle imaging with AO compensated light on large aperture (8m class) telescopes for detecting closely spaced objects [25].

Although improvements in technology are behind the renewed interest in speckle imaging,

the data analysis techniques used by the astronomy community to process speckle data (known as speckle interferometry, or SI), are, in the main, still very much rooted in the 1970s and 80s with the Knox-Thompson [26] and bi-spectrum techniques [27]. However, research outside of the astronomy community in the past decade or so has shown that processing speckle data using a blind restoration algorithm can provide a notable gain in restoration quality over that achieved using traditional SI techniques [28]. Also, augmenting single-channel speckle data with data from other channels, both imaging, and non-imaging, offers further restoration quality improvement. Sources for the additional data channel(s) include the diversity imaging approaches (phase diversity [29], wavelength diversity [30], multi-aperture diversity [31, 32]) and wavefront sensor data [33].

Most of the research conducted into processing speckle data has focused on the case where the impulse response, or Point-Spread Function (PSF), for an image does not vary with spatial location in the image. That is, the angular extent of the object under investigation (θ_{obj}) is smaller than the isoplanatic angle [34] for the observations,

$$\theta_0 = 0.314 r_0 / \bar{h} \quad (2.1)$$

defined as the angle over which the wavefront phase varies by 1 radian, r_0 is the coherence length of the atmosphere, also known as the Fried parameter,

$$\bar{h} = \sec \zeta \left[\frac{\int C_n^2(h) h^{5/3} dh}{\int C_n^2(h) dh} \right]^{3/5}, \quad (2.2)$$

$C_n^2(h)$ is a measure of the atmospheric turbulence at height h , ζ is the zenith angle of the object, and the number of “isoplanatic patches” covered by the object $N_{patch} = (\theta_{obj}/\theta_0)^2 < 1$.

In this case, for incoherent light, we can model an image (g) as the convolution of the object we seek (f) and the PSF for the observation (h), i.e.,

$$g(\vec{x}) = \int f(\vec{x}_0) h(\vec{x} - \vec{x}_0) d\vec{x}_0 \quad (2.3)$$

where \vec{x} and \vec{x}_0 are 2-D spatial coordinates in the image plane and object plane, respectively [35]. Equation 2.3 represents the isoplanatic imaging model. Based on Eqn. 2.3, it is clear that we can recover the object from the image data through deconvolution for images acquired under isoplanatic conditions. When the PSF is unknown, we retrieve both the object and the PSF using blind deconvolution [36]. When wavefront sensor data are available, we can use them to estimate the PSF for the restoration directly and recover the object through *deconvolution from wavefront sensing* [37]. A limitation of this approach is that information on the PSF encoded in the speckle image is not leveraged in the restoration process. We remedy this by allowing the wavefront phase estimated from the wavefront sensor data to be updated during the restoration: a process known as *myopic* deconvolution [33]. A similar story holds for the processing of speckle diversity imaging data in that the majority of algorithms reported in the literature are designed for data with $N_{patch} < 1$. This predisposition toward using the convolution imaging model for the restoration is because convolution is computationally inexpensive when using the Fourier transform. However, when $N_{patch} \gtrsim 1$ the PSF varies with spatial location in the image, and we need to model an observed image using the anisoplanatic imaging model [35]

$$g(\vec{x}) = \int f(\vec{x}_0) h(\vec{x} : \vec{x}_0) d\vec{x}_0 . \quad (2.4)$$

Unfortunately, this superposition integral is computationally expensive for objects of any significant spatial extent [38, 39]. To minimize the expense, researchers have taken the approach of partitioning an observed image where $N_{patch} \gg 1$ into sections where $N_{patch} \sim 1$. They then use a blind deconvolution algorithm to recover the object and PSF in each image section, which is not necessarily the same size for all sections [40], and then either sew the recovered sections of the object back together or sew (interpolate) the individual PSFs and restore the image globally [41]. Unfortunately, this approach of partitioning the image is limited to cases where there are a sufficient number of resolution elements across a sub-region so that the deconvolution can provide a high-quality estimate of the local object and PSF. This requirement is not always available [39]. This leads us back to modeling the image using Eqn. 2.4. It is clear that if we are to pursue high-resolution, high-contrast imaging, where it is critical to model the speckle morphology with high accuracy, we must pay careful attention to the value of N_{patch} for our observations. On this note, we see that the small FOV options for the NESSI and Alopeke speckle imaging systems [42] are 6.7" and 19", respectively. For seeing conditions of 1" (at 500 nm) and a mean height of turbulence, $\bar{h} = 5.5$ km, these FOVs represent maximum values of $N_{patch} \sim 32$ and ~ 260 , respectively, for observations of targets at zenith in the visible. Using an isoplanatic model for the image (i.e., Eqn. 2.3) will not provide the highest quality restoration under these observing conditions if the angular extent of the object represents a sizable fraction of the FOV. The wide FOV options for NESSI and Alopeke are 56" and 60", respectively. This represents maximum values for N_{patch} of over 2,000. Here we obviously need to use an anisoplanatic image model

for the data to provide any reasonable restoration of the data.

Standard speckle data sets comprise hundreds to thousands of images. When the object remains stationary throughout the data acquisition, processing a series of frames provides a strong constraint on the estimate of the object. This is the basis of multi-frame blind deconvolution (MFBD; [43, 44]). If the speckle data are acquired simultaneously with wavefront sensing data at a cadence faster than the Greenwood frequency [45], the frequency that an Adaptive Optics (AO) needs to be run at to accurately correct the wavefront, for the observing conditions, $f_G = \tau_0^{-1}$, where $\tau_0 = 0.314 r_0/\bar{V}$ is the atmospheric coherence time and \bar{V} is the mean wind velocity given by

$$\bar{V} = \left[\frac{\int C_n^2(h)|V(h)|^{5/3}dh}{\int C_n^2(h)dh} \right]^{3/5}. \quad (2.5)$$

Then we can leverage the frozen flow behavior of the atmosphere [46] to improve our estimation of the wavefront phase for each image [47]. This leverage also applies to the data from any of the diversity imaging methods, which provide a constraint on the wavefront phase estimates during the restoration, and wavefront sensor data, which directly measure the wavefront phases. We note that if data are acquired at a cadence less than f_G , which may be the case when observing dim targets and we need to resort to temporal integration of the image signal, then we lose access to the high-spatial frequency information contained in the temporal correlations in the wavefront. We also note that frozen flow behavior is observed in AO corrected wavefronts when $N_{patch} \leq 1$, and a single deformable mirror is used for the wavefront correction, and when $N_{patch} \gg 1$, and multi-conjugate AO is used for correcting the phases in different atmospheric layers.

Up to this point, we have seen that according to conventional wisdom, we can use isoplanatic modeling, which is computationally inexpensive, for speckle images with $N_{patch} < 1$, and anisoplanatic modeling for speckle images with $N_{patch} \gg 1$, which is computationally expensive (close to prohibitive), as shown by the phase-diversity deblurring algorithm of [38]. However, for extreme scenarios, e.g., high-contrast binary systems, anisoplanatic effects across a narrow field of view ($N_{patches} < 1$) become non-negligible. In this scenario, accurate recovery of the wavefront is paramount to recovering the flux and morphology of the object accurately. According to [48], accurate flux ratios are necessary for determining the mass and spectral types of faint companions where large uncertainties and inaccuracies can vastly change the recovered stellar parameters.

Here, we investigate image deblurring using speckle data augmented with a time series of wavefront sensor data acquired with a simple two-channel speckle imaging system. We demonstrate that Wavefront Sensor (WFS) data provide information on the wavefront phase, the heights of the turbulent layers, and the low spatial frequencies of the object. During the restoration process, this additional information augments similar information that is encoded in the image data acquired through the full telescope pupil. This extra information results in an improved restoration. Moreover, we show that by modeling the temporal correlations in the atmosphere, WFS data can provide information on the phases in the atmosphere's individual layers, even for isoplanatic data. With an approximation of the anisoplanatic PSFs, we can use the full aperture images (either with or without the WFS data) to then place the layers at their heights and produce both an improved object estimate and spatially-varying

PSF models, together bringing accurate photometry of the source. We show here that a full tomographic recovery is necessary for accurate object recoveries even across FOVs that are typically considered isoplanatic.

In Sec. 2.2 we describe our two-channel speckle imaging system and how it can be used to separate the layers of the atmosphere and place the layers at their appropriate heights. In Sec. 2.3 we present our multi-frame blind deconvolution and deblurring recovery processes. In Sec. 2.4 we describe our simulations of wavefront sensor and full aperture speckle data across various degrees of anisoplanatism and in Sec. 2.5 we present the results of these recoveries. Finally, in Sec. 2.6 we discuss the implications of these results and potential applications.

2.2 Two-channel Speckle Imaging System

Here we describe our two-channel speckle imaging system consisting of a full aperture imaging channel and a wavefront sensor channel that provides a multi-frame aperture diverse dataset with low-resolution information on the target and information on the heights of the atmospheric layers. The Shack Hartmann (SH) sensor is probably the most used type of Wavefront Sensor (WFS) due to its simplicity. Thus, we will use a variant, the Imaging Shack-Hartmann (ISH) (or “Scene-based” Shack-Hartmann) WFS to study the effectiveness of our technique. The ISH WFS basically consists of a micro-lens array and a camera. The sensor partitions the wavefront in the entrance pupil into a set of sub-apertures. The wavefronts in the sub-apertures are then focused onto the camera with a magnification such that

the resulting images are each sampled by $N \times N$ pixels. For traditional SH “spot” data, $N = 2$ or 3 . For “scene-based” SH data, N is typically a power of 2 [49] with typical values of $N = 16, 32, 64$. Above these sizes the computational cost to model the subaperture images increases significantly. Commonly, we recover wavefront information from the sub-aperture images through the blurred object’s motions, which are related to the gradients of the wavefront in the sub-apertures [50, 51]. This is true for both spot and scene-based SH data. The object’s motions in the former are typically determined from center-of-gravity calculations [52]. For the latter, they are determined from cross-correlations [49, 53]. However, we can also recover the wavefront by modeling the sub-aperture images [54, 55]. Here the model for each image uses a Fourier Optics description for the Point-Spread Function (PSF). The instantaneous monochromatic PSF at wavelength λ and a given point in the image \vec{x} at time t is modeled using

$$h_\lambda(\vec{x}, t) = F^{-1} [P_\lambda(\vec{u}) \otimes P_\lambda(\vec{u})]_{\vec{x}, t} \quad (2.6)$$

where $P_\lambda(u, v) = |P(u, v)|e^{i\phi(u, v)}$ is the line-of-sight integral of the complex wave front, with amplitude $|P(u, v)|$ and phase $\phi(u, v) = 2\pi \frac{W(u, v)}{\lambda}$, from the given field point to the pupil at point (u, v) , $i = \sqrt{-1}$, $W(u, v)$ is the optical path difference, \otimes denotes cross-correlation¹, and F^{-1} is the inverse 2-D Fourier transform operator. An advantage of this approach is that we are free to choose the number of pixels we use to describe the wavefront in a sub-aperture when generating our model image. By selecting a number of pixels that’s greater than the

¹The cross-correlation of two signals, f and g , is defined as $f \otimes g = \int_{-\infty}^{\infty} \overline{f(t)}g(t + \tau)dt$, where $\{\cdot\}$ is the complex conjugate. Furthermore, the cross-correlation can be expressed in terms of Fourier transforms as $f \otimes g = F^{-1} [\overline{F(f)}F(g)]$.

number of sub-apertures across the pupil, we can estimate the wavefront perturbations at finer spatial scales than we can through using image motion measurements [54]. However, care should be taken to select a number of pixels and subapertures that provides a desirable SNR, which will depend on the target being studied.

2.2.1 Separation of Atmospheric Layers

Wavefront estimation is commonly done on an image-by-image process. As such, this approach ignores temporal correlations in the wavefront due to the atmosphere's frozen flow behavior. These correlations provide additional information about the wavefront that we can harvest from a time series of high-cadence SH data. The maximum observable correlation time, t_{max} , occurs when the turbulent layers are effectively frozen for the time required for the bulk wind to carry the patterns across the telescope pupil. That is, $t_{max} = D/|\bar{V}|$, where D is the telescope diameter, and $|\bar{V}|$ is the bulk wind velocity [56]. This maximum correlation time is significantly longer than the exposure time required to freeze the instantaneous wavefront aberrations, $t_{exp} \leq \tau_0$ [56]. For 1" seeing in visible light ($\lambda = 500$ nm), $r_0 \sim 10$ cm. For $\bar{V} \sim 5$ m/s we have $\tau_0 \sim 6$ ms, and for observations with an 8 m telescope we have $t_{max} \sim 267 \tau_0$. However, practically, evolution in the wavefront as it crosses the telescope pupil results in a smaller value for t_{max} . Observations suggest $t_{max} \leq 100$ ms [57]. The first mining of the temporal information in a time-series of SH data for use in image restoration showed that we could recover spatial information on the wavefront on finer scales than are sampled by the sub-apertures [47, 58].

Fig. 2.1 demonstrates how the wavefronts in the different turbulence layers can be sepa-

rated from measurements of the wavefront obtained using a scene-based SH sensor.

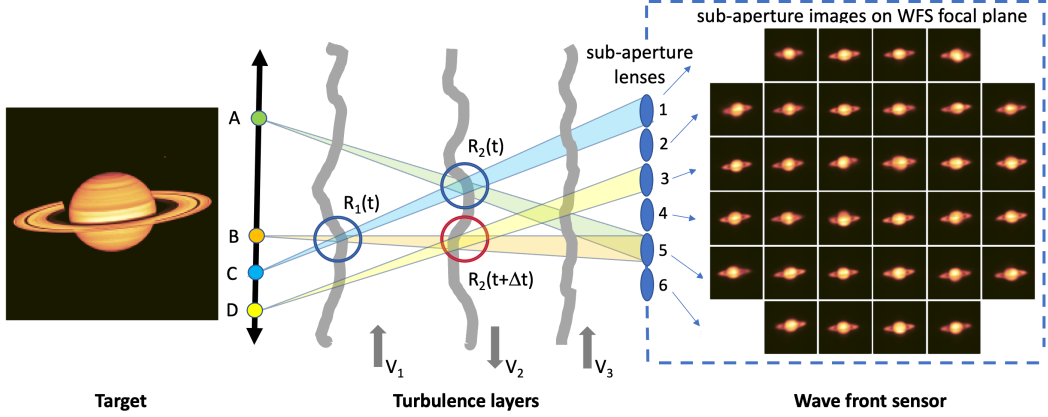


Figure 2.1 Simple diagram displaying how tomography with a resolved source is enabled through the use of a scene-based Shack-Hartmann wave front sensor. See main text for details.

Here we can see that the wavefront in a given layer at a given time and spatial location affects the light at different field points in the source plane, and therefore in the sub-aperture images. For example, at a given instant in time, the region R_2 in the second atmospheric layer is sampled by the field point A in sub-aperture 5 and field point C in sub-aperture 1. Similarly, field points B and C, as measured in sub-apertures 1 and 5, respectively, sample the same region in layer 1 (R_1). This geometry enables tomographic separation of the layers *if their heights are known*, which is not the norm. The heights of the layers usually need to be provided by some other method that can measure the vertical profile of the turbulence, e.g., SCIDAR (SCintillation Detection And Ranging [59, 60]) and SLODAR (SLOpe Detection And Ranging [61]). However, the full aperture images allow the determination of the heights of the layers if the layers have been separated (see Sec. 2.2.2).

Luckily, a second lever is available for separating the layers. We focus on one that does

not need prior knowledge of the layers' heights - the atmosphere's frozen flow behavior. The frozen flow hypothesis results in a given region in any layer being sampled by different field points at different times (i.e., in different images). For example, the layer which contains region R_2 at time t and is sampled by field points A and C in sub-apertures 5 and 1, respectively, will have moved after an additional time Δt such that it will be sampled by field points B and D in sub-apertures 5 and 3, respectively. This avenue should let us use a time series of images to separate the atmospheric layers without knowledge of their heights. The latter is demonstrated in Fig. 2.1. Here we have three atmospheric layers in the telescope's aperture, where, for simplicity sake, we will consider the two layers that are at some altitude from the observer. These layers are propagating in opposite directions with different velocities v_1 and v_2 . At time t , regions R_1 , R_2 , and R_3 in each layer contribute to the images generated by lenses 1, 3, and 5, in the Shack-Hartmann sensor, respectively. At time $t + \Delta t$ regions R_1 and R_3 in layers 1 and 2 have propagated outside the telescope's aperture, and now region R_2 in layer 1 contributes to the image formed by lens 2, R_1 in layer 2 contributes to the images formed by lenses 3 and 4, and R_3 in layer 1 and R_2 in layer 2 contribute to the image formed by lens 5. Thus, a time series of images contains the information needed to separate the layers. In practice, the frozen flow behavior of the atmosphere is observed by taking the 3D autocorrelation of wavefront slope data from a SH-WFS [62].

Based on this model, we expect the layer separation quality to increase as the number and spatial coverage of field points with signal and the number of data frames used for

the separation increases. To investigate our hypothesis that the frozen flow behavior of the atmosphere enables separation of the layers, we performed a series of numerical simulations.

2.2.2 Estimation of Layer Heights

Now that we have shown that the atmosphere's frozen flow behavior facilitates the separation of the layers, all that remains for a tomographic mapping of the volume turbulence is to determine the height of the layers.

Fortunately, the information on the layers' heights is encoded in any short-exposure image data where $N_{patch} > 1$. This is because for $N_{patch} > 1$ there is a spatial variation of the atmospheric point spread function, which is manifest by spatial variation of the PSF shape due to the light from each field point traversing different paths through the turbulence. As the separation between field points increases, the discrepancy between the PSFs of the far field points also increases, as seen in Fig. 2.2. Extracting the height information from the image data requires that we accurately model the image data across the FOV. Accurate modeling of the image data requires that we have good estimates for both the object and the wavefronts in the different atmospheric layers. Fortunately, we have these when we perform a multi-aperture phase retrieval [54] reduction of scene-based SH data. This means we have everything we need to find the heights of our wavefront layer estimates to best model the sub-aperture image data.

We solve for the layers' heights using an iterative approach. As a starting point, we assume that the order of layers is related to the layers' wind velocities, with the smallest velocity corresponding to the lowest layer and the largest velocity to the highest layer. Then,

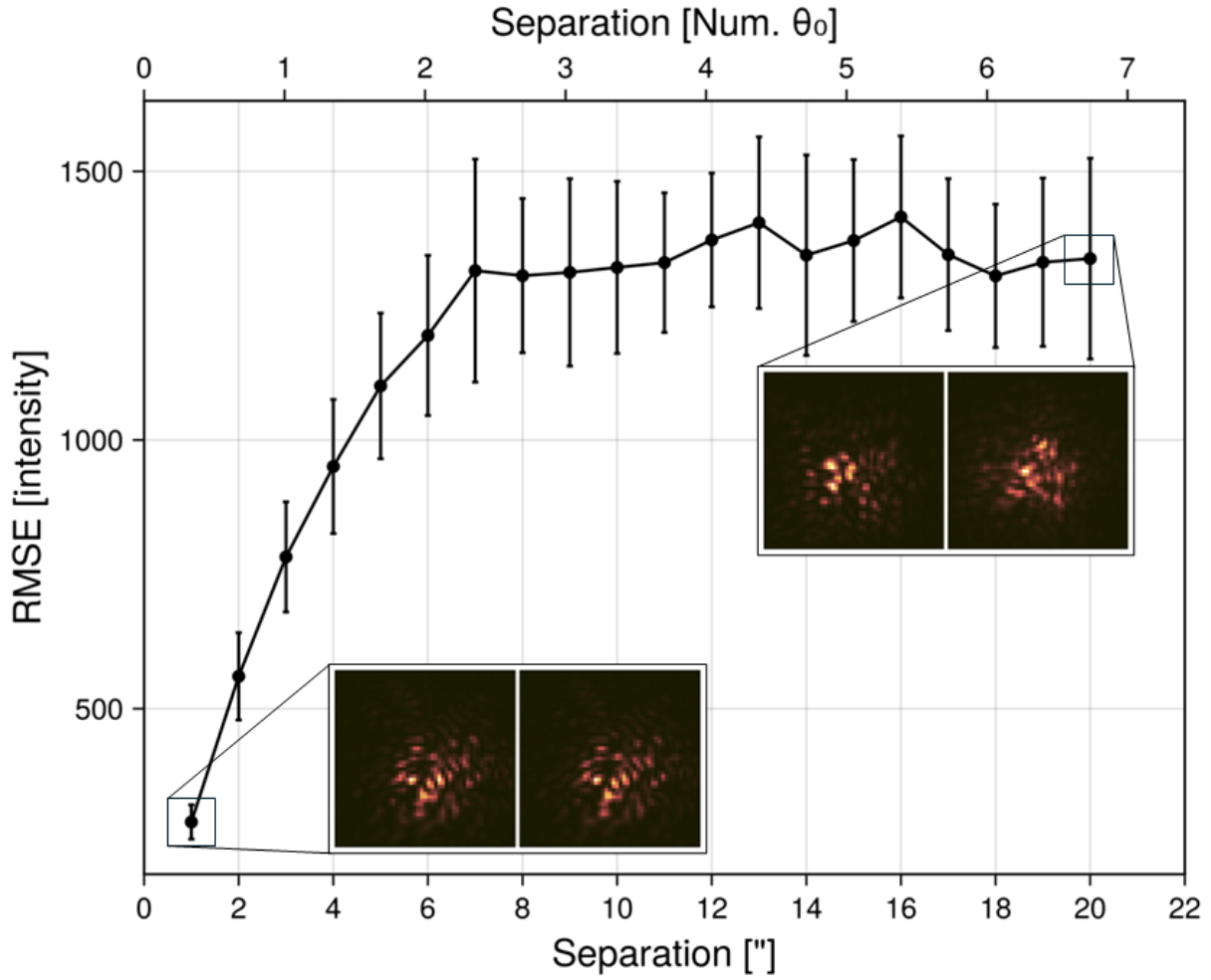


Figure 2.2 Root Mean Square Error (RMSE), in units of intensity, between atmospheric PSFs at two field points as a function of angular separation in units of arcsec ("") and number of isoplanatic angles ($\theta_0 = 2.97''$ for $r_0 = 18$ cm at 500 nm; Eqn. 2.1). The insets show the PSFs at the two extremes of the curve. In the 1" case the PSFs are visually indistinguishable. Differences are clearly seen between PSFs in the 20" case. These RMSE values are the ensemble average of 50 realizations of the atmosphere.

we assume the mid-altitude layer is located between 5 – 10 km and the high-altitude layer is between 10 – 20 km, similar to the approach by [63]. However, we also look at other layer combinations if we cannot produce models that clearly describe the data. At each combination of heights a truncated deblurring step is performed where we first solve for the phase until a stopping condition is reached and then we solve for the updated object under the same stopping condition. For an explanation of how we perform deblurring see Sec. 2.3.2. For the stopping condition for each step in the process we chose to limit the relative change in the gradient norm of the objective function, defined in the next section, $(||\nabla \epsilon_{i-1}||_2 - ||\nabla \epsilon_i||_2) / ||\nabla \epsilon_{i-1}||_2 < 0.01$. This effectively limits the number of iterations needed in each phase and object update for convergence. An example of how the objective function varies during this step is shown in Fig.2.3.

2.3 Reconstruction Method

In this section we outline the method used for recovering the initial phase and object assuming a spatially-invariant PSF and the deblurring process used for recovering a spatially varying PSF. We seek to find the object \tilde{f} and phase $\tilde{\Phi}$ that minimize the weighted likelihood:

$$\epsilon = \sum_t \sum_n \left(\hat{I}_{tn} - I_{tn} \right)^\top \omega_{tn}^{-1} \left(\hat{I}_{tn} - I_{tn} \right) \quad (2.7)$$

where ω_{tn} is the diagonal covariance weight for sub-aperture n at time t , and I_{tn} and \hat{I}_{tn} are the observed and model frames, respectively. The covariance is set as $\omega_{tn} = s_{tn}(\hat{I}_{tn} + \sigma_{RN}^2)$. It accounts for the Gaussian detector read noise σ_{RN} , the shot noise on the model frames

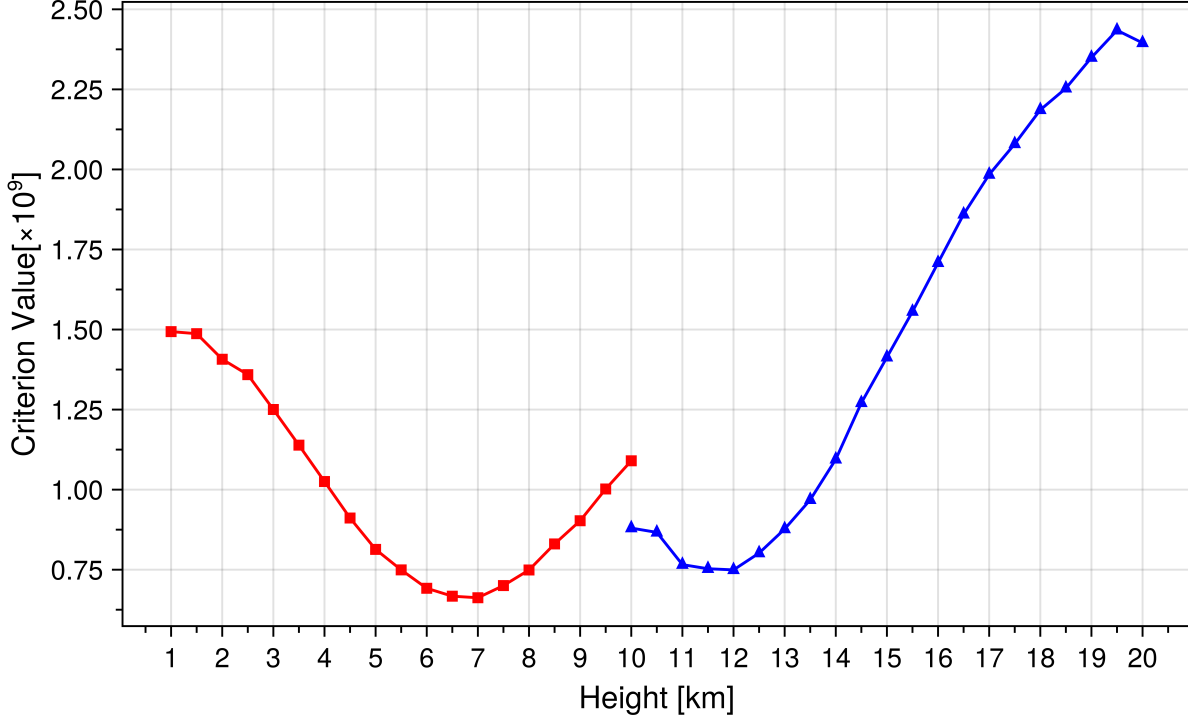


Figure 2.3 An example of how the error metric changes with the heights of the layers during the height solve part of the analysis. Here we use a 3-layer model to simulate observations. The layers are initially set at $h = 0$ km, with the lowest wind velocity layer fixed at ground height throughout the entire analysis. The layer with the highest wind velocity is varied first (blue triangles) and is assumed to be the high-altitude layer between 10 – 20 km. Then, the layer is fixed to the height that provides the lowest criterion value. Next, the mid-altitude layer is allowed to vary in height (red squares) between 5 – 10 km. Finally, with both layers at their respective heights the process is repeated. These results are without tip/tilt estimation on each layer.

\hat{I}_{tn} , and a frame-dependent weight based on the information entropy

$$s_{tn} = -\frac{I_{tn}}{\sum_{x,y} I_{tn}} \log_2 \left(\frac{I_{tn}}{\sum_{x,y} I_{tn}} \right), \quad (2.8)$$

where high-entropy frames are less-heavily weighted to reduce the influence of noise in the reconstruction process. How the model frames are built depends on the nature of the PSFs (i.e., spatially varying vs spatially invariant), and is described in the sections below. The

likelihood was minimized using the Variable Metric Limited-Memory Bounded quasi-Newton method implemented in `OptimPackNextGen.jl`².

2.3.1 Deconvolution

The initial estimate for the isoplanatic phase and object is made using a multi-step recovery process. Phase retrieval is well-known to be susceptible to entrapment in local minima using gradient-based optimizers [64]. To alleviate this it is helpful to “anneal” through spatial frequency by first estimating the low spatial frequencies in the phase and object, and then allowing higher spatial frequencies to vary. Processing the WFS frames first allows only the low spatial frequency information in the object and phase to vary.

The phases are initialized to zero-mean, unit variance random Gaussian numbers and the object is initially estimated as the lucky image of the full aperture frames [65]. Then, in the phase update step, the model images \hat{I}_{tn} for each sub-aperture n (or the full aperture) at time t are given by the multiplication of the PSF h_{tn} by the matrix operator $X = F^{-1} \text{diag}(F\tilde{f})F$ that convolves its input with the object estimate \hat{f}

$$\hat{I}_{tn} = S_{\downarrow} X h_{tn} \quad (2.9)$$

where S_{\downarrow} is a downsampling operator to match the pixel resolution of the observed frames. F and F^{-1} are the discrete fast Fourier transform operator and its inverse, respectively. Similar to Eqn. 2.6, PSFs are built using a Fourier optics formulation of the observed wavefront

$$h_{tn} = \alpha |F^{-1} p_{tn}|^2 \quad (2.10)$$

²<https://github.com/emmt/OptimPackNextGen.jl>

where α is a scalar to account for changes in flux from a beam splitter and $p_{tn} = A_{tn}e^{i\phi_{tn}}$ is the complex pupil function composed of an amplitude A_{tn} and phase ϕ_{tn} . For the initial steps of the analysis the pupil amplitudes are assumed to be unity inside each respective sub-aperture. We are leveraging the frozen flow behavior of the atmosphere by extracting the composite pupil phase for each layer l from a phase sausage Φ_l , that the telescope aperture translates across with time:

$$\phi_{tn} = \sum_l M_n N E_{lt} \tilde{\Phi}_l \quad (2.11)$$

where M_n is a binary mask for sub-aperture n and E_{lt} is the matrix operator that extracts the patch of phase by translating layer l according to the wind velocity, resizing according to layer height, and cropping to the desired image size. N is a matrix operator to convolve the extracted phase with a Gaussian kernel. The FWHM of the kernel follows a schedule that decreases with each iteration of the process until it is smaller than a single pixel. With a decreasing smoothing kernel, the lowest spatial frequencies in the phase are modified first and then higher frequency content is slowly introduced into the recovery. As above, this helps to avoid entrapment in local minima, and additionally, avoids wrapping in the recovered phases.

Once an estimate for the phases in each layer is made, we move on to the object update step. Similar to Eqn. 2.9, the model image for sub-aperture n at time t is given by

$$\hat{I}_{tn} = S_{\downarrow} H_{tn} \tilde{f} \quad (2.12)$$

where $H_{tn} = F^{-1} \text{diag}(F h_{tn}) F$ is the matrix operator that convolves its input with the PSF

for sub-aperture n at time t . Positivity is imposed on the recovered object \tilde{f} by a projection onto the positive set.

After the object is estimated we repeat the process a set number of times (typically 10) using only the WFS data, and then add in the full aperture data and perform the deconvolution process again using the low-resolution object and phases from the initial solve as the initialization.

2.3.2 Height Solver

In order to solve for the heights of each layer we need to estimate a spatially-varying PSF for each image. For this task we use the Efficient Filter Flow (EFF) method from [66] with 50% overlap between patches and a Bartlett-Hann window function defining the patch weights. The advantage of the EFF method is that, with our choice of window function and overlap, it produces smoothly varying PSFs across the image. With this, Eqns. 2.9–2.12 become

$$\hat{I}_{tn} = \begin{cases} \sum_m S_{\downarrow} X_m h_{tnm} , & \text{(Phase Step)} \\ \sum_m S_{\downarrow} H_{tnm}(\rho_m \tilde{f}) , & \text{(Object Step)} \end{cases}$$

$$h_{tnm} = \alpha |F^{-1} p_{tnm}|^2 ,$$

$$\phi_{tnm} = \sum_l M_n N E_{ltnm} \tilde{\Phi}_l ,$$

where m is the index of each patch, ρ_m are the weights for patch m , $X_m = F^{-1} \operatorname{diag}(F \rho_m \tilde{f}) F$, and $H_{tnm} = F^{-1} \operatorname{diag}(F h_{tnm}) F$. Once the heights of the layers are known the wavefront fidelity greatly improves and allows the object morphology to be refined.

2.4 Simulated Observations

We simulated an atmosphere with three layers, chosen because of the prevalence of 3 strong layers in data collected by [62] at Haleakala, HI. These layers are placed at 0 km, 7 km, and 12.5 km [67] with a constant C_n^2 profile, and a wind profile typical of Haleakala, HI, in springtime, as per [68]. In this case, 50% of the photons are sent to a simulated full-aperture, focal plane imaging system and the other 50% are sent to the simulated WFS, which was chosen to be an ISH with 6×6 sub-apertures across the pupil. The full aperture images are sampled by 256×256 pixels and the magnification was chosen such that the diffraction-limited PSF at 500 nm is Nyquist sampled. Similarly, the WFS images are down-sampled to 64×64 pixels to more closely match the Nyquist sampling requirement for the sub-apertures. The parameters for the full aperture and sub-aperture cameras, which are assumed to be identical, can be found in Table 2.1.

We test our method against target separation for two separate target morphologies: a high-contrast binary system, and an extended, resolved source, in this case Saturn.

For the binary star system, the angular separation between sources is determined by the distance (assumed to be infinity) and physical separation of the system. We fix the flux ratio between the primary and secondary stars at $F_{sec}/F_{pri} = 10^{-2}$. We investigate two separations of the stars: 3" separation to evaluate our ability to recover each sources *within* one isoplanatic angle, and 20" separation to show our ability to recover sources well outside of the isoplanatic angle ($\theta_0 = 2.97"$ at 500 nm). The difference between the generated PSFs of the two sources, measured by the RMSE, as a function of separation is shown in Fig. 2.2.

Table 2.1 Simulated Atmospheric and Detector Parameters

Atmospheric Parameters		
r_0	18 cm	
l_0	0.01 m	
L_0	300 m	
λ	500 nm	
N_{layers}	3	
Layer Parameters		
Layer Number	1	2
Height	0 km	7 km
Wind Speed.....	5.0 m/s	6.9 m/s
Wind Direction	45°	125°
		135°
Detector Parameters		
D	3.6 m	
QE	0.8	
σ_{RN}	2.0 e ⁻	
N_{pix} (Full Aperture)	256×256	
N_{frames}	31	
$t_{exposure}$	5 ms	
$N_{apertures}$ (WFS) ...	6×6	
N_{pix} (WFS)	64×64	

We assign the primary star a brightness of $m_V = +4$, making the secondary star $m_V + 9$.

Finally, for the case of Saturn the largest separation between field points is the angular extent of the planet's rings, where the globe of the planet measures $\sim 20''$ and the rings, measured end-to-end, are $\sim 40''$ in extent. Saturn's moons Mimas, Dione, and Enceladus are within the FOV $29''$ ($10\theta_0$), $18''$ ($6\theta_0$), and $32''$ ($11\theta_0$) from the image center, respectively. We assign a brightness of $m_V = +1.17$ to Saturn, representing the faintest expected brightness of the planet. The moons have contrasts of $\Delta m_V \approx +11, +10$, and $+10$, respectively, compared to Saturn itself.

2.5 Results

To measure the success of our method we compute the normalized Root Mean Square Error (RMSE) between truth (f) and recovered object (\tilde{f}) over an $N \times N$ window by Eqn. 2.13.

$$RMSE = \sqrt{\frac{1}{N^2} \sum_{x,y} \left(\frac{f - \tilde{f}}{\sum_{x,y} f} \right)^2}. \quad (2.13)$$

RMSE sometimes does not match well with human perception so we also choose to compute the Structural Similarity Index Measure (SSIM) [69]. Since we are most interested in changes in morphology we chose only to compute the structure term of the SSIM, given below as $SSIM_s$. Typically, SSIM is calculated across small windows of the images by Eqn. 2.14 after being convolved with a small Gaussian kernel, and these SSIM values are averaged together.

$$SSIM_s(f, \tilde{f}) = \frac{\sigma_f \tilde{f} + c_3}{\sigma_f \sigma_{\tilde{f}} + c_3} \quad (2.14)$$

where f and \tilde{f} are first normalized to the same maximum value so that their values lie between 0 and 1, σ_f^2 and $\sigma_{\tilde{f}}^2$ represent the variance of the quantity and covariance between quantities, respectively, and $c_3 = 0.03^2/2$ for floating point numbers [70]. For this work, we choose a window size of 11×11 pixels and a Gaussian of $FWHM = 1.5$ pixels to convolve the inputs of Eqn. 2.14 with. A perfectly recovered object would yield an SSIM of 1, while a value of 0 indicates no structural similarity. This metric is particularly adept at measuring differences in *perceived* structure of images, and can reveal subtle differences even when two distinct images give the same RMSE when compared to the ground truth. Each metric has its strengths and so we report both metrics for all of our results.

The results of each experiment are summarized in Table 2.2.

Target	Isoplanatic		Anisoplanatic	
	RMSE	SSIM _s	RMSE	SSIM _s
3” Binary	4.8×10^{-4}	0.999	9.7×10^{-5}	0.999
Primary	2.5×10^{-1}	0.996	5.3×10^{-2}	0.999
Secondary	3.3×10^{-1}	0.732	1.8×10^{-1}	0.999
20” Binary	2.3×10^{-3}	0.997	3.9×10^{-5}	0.998
Primary	2.0×10^{-1}	0.784	4.5×10^{-4}	1.000
Secondary	3.2×10^{-1}	0.738	2.6×10^{-1}	0.783
Saturn	1.8×10^{-5}	0.945	1.0×10^{-5}	0.962
Mimas	8.4×10^{-2}	0.008	5.4×10^{-2}	0.833
Dione	7.8×10^{-2}	0.000	5.0×10^{-2}	0.671
Enceladus	8.2×10^{-2}	0.007	6.1×10^{-2}	0.577

Table 2.2 RMSE and SSIM_s values for each experiment. “Isoplanatic” and “anisoplanatic” here refer to the way the data are treated.

The morphology of the recovered binary star system at 3” and 20” separation is seen in Fig. 2.4 and 2.5, respectively. Here we see the RMSE between the binary sources increases from the 3” case to the 20” case under an isoplanatic imaging model. However, the RMSE lowers, in both cases, under the anisoplanatic imaging model. The larger separation in the 20” case means that the initial isoplanatic solve will be lower in quality. However, wide separations help to distinguish the PSFs of each source and provide a cleaner recovery once the heights of the layers are found. In the 3” separation case the PSF of the secondary star is embedded in the PSF of the primary, making it harder to disentangle the two sources. However, 3” is approximately equal to the isoplanatic angle for these conditions, meaning that even across a FOV considered isoplanatic, there are non-negligible performance gains that are accessible if the data are modeled using an anisoplanatic model. To further illustrate the point, the flux ratio, measured within an $N \times N$ region, between sources is more accurate

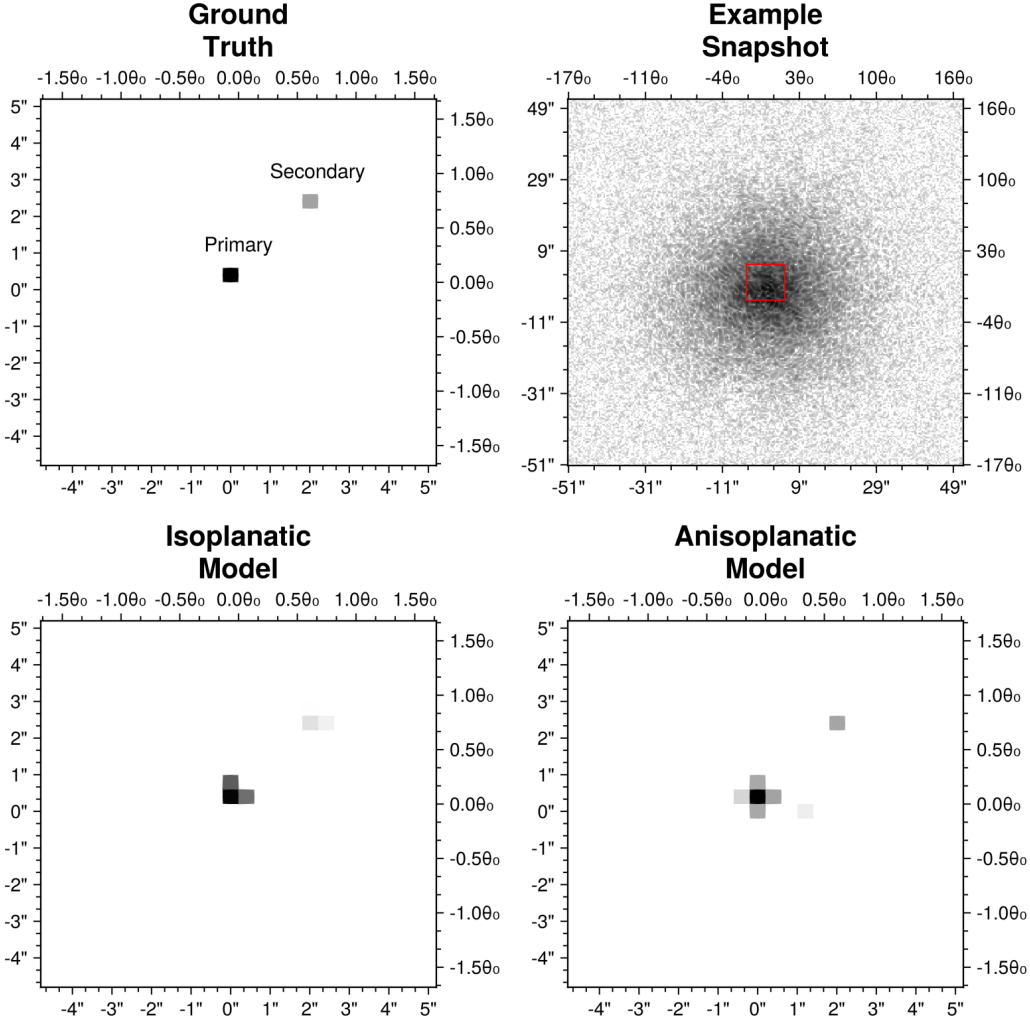


Figure 2.4 Recoveries of a high-contrast binary ($F_{sec}/F_{pri} = 10^{-2}$) at $3''$ separation. The recovery with the isoplanatic model (bottom left) and with the anisoplanatic treatment of the data (bottom right) are shown against the ground truth (top left) and an example data frame (top right). All images are on a logarithmic scale.

under the anisoplanatic model, as seen in Table 2.3. Within a 5×5 pixel region around each star, we are able to recover the true flux ratio in both the $3''$ and $20''$ case.

Finally, the recovered image of Saturn, using both the isoplanatic and anisoplanatic imaging models, can be seen in Fig. 2.6. The reduced RMSE under the anisoplanatic model

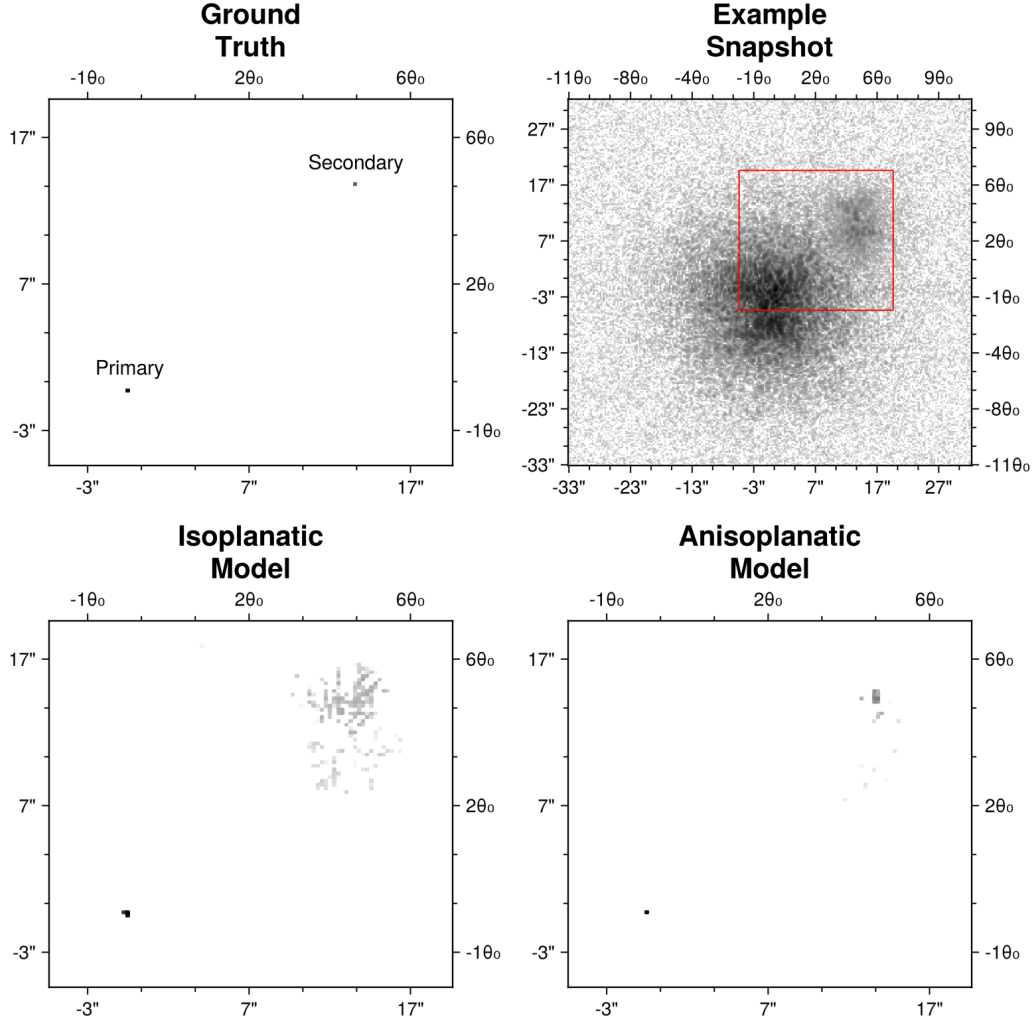


Figure 2.5 Recoveries of a high-contrast binary ($F_{sec}/F_{pri} = 10^{-2}$) at $20''$ separation. The recovery with the isoplanatic model (bottom left) and with the anisoplanatic treatment of the data (bottom right) are shown against the ground truth (top left) and an example data frame (top right). All images are on a logarithmic scale.

allows for details far from the image center, such as the Cassini division and the moons Mimas, Dione, and Enceladus to be recovered more accurately.

Separation	Isoplanatic		
	F_{sec}/F_{pri} (1×1 window)	F_{sec}/F_{pri} (3×3 window)	F_{sec}/F_{pri} (5×5 window)
3"	2.2×10^{-3}	6.1×10^{-3}	6.1×10^{-3}
20"	2.3×10^{-4}	5.2×10^{-4}	1.5×10^{-3}
Separation	Anisoplanatic		
	F_{sec}/F_{pri} (1×1 window)	F_{sec}/F_{pri} (3×3 window)	F_{sec}/F_{pri} (5×5 window)
3"	9.4×10^{-3}	9.1×10^{-3}	1.0×10^{-2}
20"	2.3×10^{-3}	9.1×10^{-3}	1.0×10^{-2}

Table 2.3 Recovered flux ratios using different size windows (in pixels) around each source for the binary system at 3" and 20" separation.

2.6 Conclusions and Discussion

Here we have shown that with a 2-channel imaging scheme one can 1.) separate the atmospheric layers, 2.) place them at their heights, and 3.) recover the morphology of the object accurately. The wavefront sensor channel provides aperture-diverse measurements that are necessary for extracting the wind velocities of each layer that can then be used to separate the atmospheric layers and place them at their heights. These measurements also contain low-resolution information on the underlying object that helps seed the recovery when full-aperture data are introduced. These two channels together have been shown here to provide a powerful lever for extracting the incident wavefronts at their respective heights and high spatial frequency details in the recovered object. Additionally, we show that appreciable anisoplanatic effects are present in FOVs previously considered to be isoplanatic. Accounting for these anisoplanatic effects with the efficient filter flow method allows for the recovery of spatially-varying PSFs. This improves the morphology of the recovered object across the entire image for both the extended, resolved source case, such as Saturn, and the

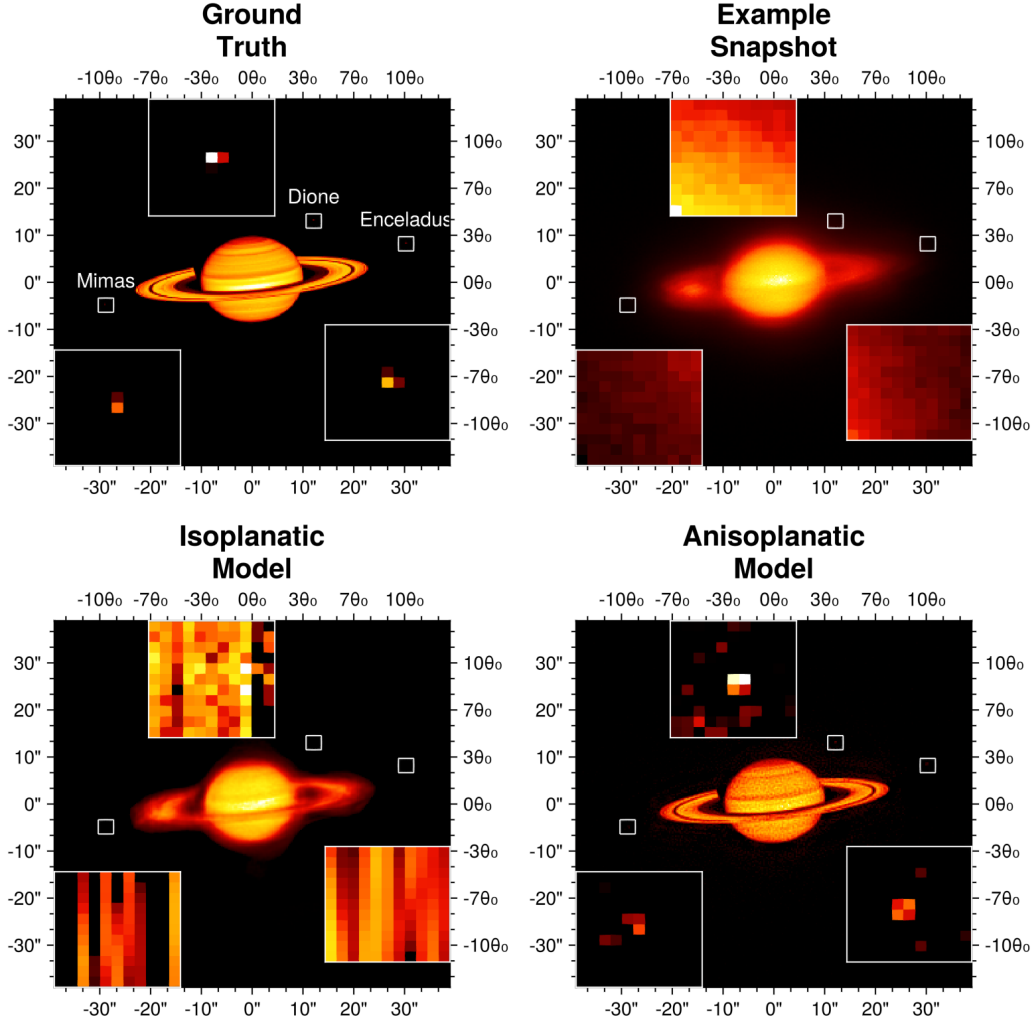


Figure 2.6 Recoveries of Saturn. The recovery with the isoplanatic model (bottom left) and with the anisoplanatic treatment of the data (bottom right) are shown against the ground truth (top left) and an example data frame (top right). Each image is shown on a linear scale. Saturn’s moons Mimas, Dione, and Enceladus, from left to right, are shown in the insets of each subplot on a square-root scale to enhance background details.

spatially-extended, unresolved source case, such as the binary system. We show that in order to recover the true flux ratio of a tight binary system we must recover a full tomographic solution for the atmosphere, which leads to greatly improved object flux and morphology.

In a real-world scenario, several higher-order effects are present that may affect perfor-

mance. Scintillation changes the flux of the source with time. The assumption of unit-volume PSFs can be relaxed to accommodate this. In the recovery process, this means that after a full recovery of the wavefront phase is made the wavefront amplitudes are also allowed to vary. [71] showed that including wavefront amplitudes in the recovery process brings up to a 40% improvement in the recovered wavefront and object when observations are taken at large zenith angles.

Next, these results have assumed a strictly-frozen flow. However, it is known that the atmosphere exhibits some degree of turbulent “boiling” as well [72]. This boiling acts to reduce the coherence time of the atmosphere. A more sophisticated model than the translating layer model used in this work is needed to account for boiling wavefronts.

Finally, these results impart only the knowledge that the recovered object must be positive. Additional regularization could provide a powerful tool to constrain both the morphology of the object and the power spectrum of the recovered wavefront. The former can be constrained by imposing a total-variation regularization. However, the ℓ_1 norm is problematic with gradient-based optimizers, such as the quasi-Newton method used in this work. A full refactoring to a scheme that can handle such a regularizer, such as the proximal-splitting method of ADMM [73] or its recent evolution, bSDMM [74]. Constraints on the wavefront can be more-cleverly placed to constrain the power spectrum of the recovered wavefront rather than its morphology. Such a regularizer would need to come from a machine-learning algorithm and would require careful training so as to not introduce biased realizations of the atmosphere into the solution.

2.7 Table of Variables

Below is a table containing each variable used in this chapter and a short description of that variable.

$\overline{(\dots)}$	Complex conjugate
$\ \cdot\ _2$	L2 norm
\otimes	Cross-correlation operator
$(\cdot)^T$	Matrix transpose
A_{tn}	Complex wavefront amplitude for subap n at time t
α	Flux-scaling parameter for beam splitters
$C_n^2(h)$	Refractive index structure parameter at height h
D	Diameter of the telescope
Δt	Time interval
E_{lt}	Extraction operator for layer l at time t
E_{ltm}	Extraction operator for layer l at time t and patch m
$f(\vec{x}_0)$	Object at object coordinate \vec{x}_0
\tilde{f}	Estimated object
f_G	Greenwood frequency
F	2D Fourier Transform operator
F^{-1}	Inverse 2D Fourier Transform operator
F_1	Flux of the primary star
F_2	Flux of the secondary star
$g(\vec{x})$	Model image at spatial coordinate \vec{x}
$h(\vec{x} - \vec{x}_0)$	PSF at coordinate offset $\vec{x} - \vec{x}_0$
$h(\vec{x} : \vec{x}_0)$	PSF at coordinate \vec{x} for field point \vec{x}_0
$h_\lambda(\vec{x}, t)$	PSF at wavelength λ , image point \vec{x} , and time t
h_{tn}	PSF variable for subap n at time t
h_{tnm}	PSF variable for subap n at time t for patch m
\bar{h}	Average height of atmospheric layers
H_{tn}	Matrix operator that convolves its input with the PSF for subap n at time t
H_{tnm}	Matrix operator that convolves its input with the PSF for subap n at time t and patch m
i	Imaginary unit
I_{tn}	Observed image for subap n at time t
\hat{I}_{tn}	Model image for subap n at time t

$\text{Im}\{\dots\}$ Imaginary part of input

λ Wavelength

M_n Mask for subap n

N Number of pixels across one side of the image

N Matrix operator that convolves its input with a Gaussian kernel

N_{patch} Number of turbulent patches across the pupil

$\nabla \epsilon_i$ Gradient of the objective function at iteration i

$P_\lambda(\vec{u})$ Pupil function at wavelength λ and frequency \vec{u}

p_{tn} Pupil function for subap n at time t

p_{tnm} Pupil function for subap n at time t and patch m

$\tilde{\Phi}_l$ Estimated phase sausage for layer l

$\phi(u, v)$ Phase at frequency coordinate (u, v)

ϕ_{tn} Complex wavefront phase for subap n at time t

ϕ_{tnm} Complex wavefront phase for subap n at time t and patch m

ω_{tn} Statistical weight of subap n at time t

r_0 Fried parameter

$\text{Re}\{\dots\}$ Real part of input

ρ_m Weight of patch m

S_\downarrow Downsampling operator

s_{tn} Information entropy of observed image of subap n at time t

σ_{RN} Read noise

τ_{atm} Coherence time of the atmosphere

t_{exp} Exposure time

t_{max} Maximum observable atmospheric correlation time

θ Separation between field points/sources

θ_0 Isoplanatic angle

\hat{u} Frequency coordinate in x direction

\hat{v} Frequency coordinate in y direction

$V(h)$ Wind velocity at height h

\bar{V} Mean wind velocity

$W(u, v)$ Optical Path Difference (OPD) at frequency coordinate (u, v)

X Matrix operator that convolves its input with the object

X_m Matrix operator that convolves its input with the object within patch m

\vec{x} Spatial coordinate in the image plane

\vec{x}_0 Spatial coordinate in the object plane

Y General observed quantity

\tilde{Y} General estimated quantity

ζ Zenith angle

CHAPTER 3

Hyperspectral Speckle Imaging of Resolved Targets

3.1 Introduction

Materials in space are greeted with a harsh bombardment of particles, most notably atomic oxygen, that eat away at a material and change its chemical structure. Important instruments and components on a satellite can be compromised if a material cannot withstand the space environment for a prolonged period. Thus, understanding the process of the aging of materials in space is paramount. Material aging is currently studied in a vacuum chamber to simulate the types of particles and radiation encountered in space [75]. However, space weather can vary wildly with different orbits and solar conditions, challenging the accuracy of ground-based experiments that provide constant radiation doses and particle fluences [76]. The Materials International Space Station Experiment (MISSE; Degroh et al. 77) remedied this by flying several common spacecraft materials on board different faces of the International Space Station. However, once returned to Earth, the materials react with air and their properties can change, through a scarring process, from when they were onboard the International Space Station [78]. Thus, we need to study the material reflectivity while the material is in space to accurately characterize space weather aging, and we require spatially resolved images to identify individual materials on the satellite.

Characterizing satellites and orbital debris requires spectral information. As pointed out by [79], even if we have an ultra-broadband image of a satellite and could attain infinite levels of spatial resolution, we are still not guaranteed to be able to identify its features and

characteristics. We also need to be able to decode the spectral data for each pixel in the image. That is, spectral and spatial data are complementary, and accurate characterization of a target needs both. Spectral information has been a mainstay for the characterization of unresolved targets for many years. Multi-color photometry has provided a means for discriminating between debris and intact space objects such as rocket bodies and satellites [80], characterizing the type and performance of ion thrusters, and studying the effects of on-orbit aging of satellite materials. The current state-of-the-art for integrated (i.e., unresolved) multi-color photometry, is 3 – 5 spectral bands of width around 100 – 150 nm, depending on the wavelength range and cadence of observation [81]. That is, the spectral information available on a target is still relatively crude. Our ability to characterize the target is thus still limited. There are many imaging techniques available for acquiring spectral information on resolved targets [82]. The technique that is probably best-suited for Space Domain Awareness (SDA) is snapshot hyperspectral imaging. Here several approaches are available, although, to the best of our knowledge, none of them are in operational use for SDA. The two approaches which appear most promising for SDA are integral field spectroscopy using lenslet arrays and computed tomography imaging spectrometry. However, these techniques require large-format detector arrays, which inherently means frame rates that are slow compared to the atmospheric coherence time. Ultra-broadband speckle imaging [83], however, can use smaller format detector arrays and does not suffer this limitation. It also provides information for at least twice as many spectral channels than are currently used for unresolved measurements.

Monochromatic speckle imaging with a ground-based telescope can recover spatial information on a space-based target with diffraction-limited resolution; however, work by [83] and [84] demonstrated that additional wavelength information on the target can be extracted from *broadband* speckle images ($400 - 1000$ nm), when accurate Point-Spread Function (PSF) are available, at a spectral resolving power of up to $\bar{\lambda}/\Delta\lambda \sim 12$ and ~ 91 , respectively, where $\bar{\lambda}$ is the mean wavelength and $\Delta\lambda$ is the width of the passband. The reconstructed hyperspectral images contain the signatures of the underlying materials that are reflecting incident sunlight. If the satellite is spatially resolved, then the signatures of its materials can be recovered per pixel. This recovery is possible because dispersion in the Earth's atmosphere, perturbations in the wavefront introduced by the atmosphere, and diffraction in our imaging instrument all spread the light out differently at each wavelength, allowing wavelength information in the target to be extracted. We aim to use this approach to perform ground-based hyperspectral speckle imaging of resolved targets in the near-Earth space environment.

In Sec. 3.2, we detail the numerical simulations performed as a proof-of-concept for hyperspectral speckle imaging, and in Sec. 3.3, we highlight our analysis approach. Then, in Sec. 3.4 we discuss our results. Finally, in Sec. 3.5, we discuss the implications of this work to the SDA community, summarize our findings, and discuss improvements to our method.

3.2 Numerical Simulations

For this study, we simulate ground-based observations of a satellite acquired using a 3.6 m aperture telescope viewing through atmospheric turbulence conditions typical for nighttime

observations from Mount Haleakala, Maui. Specifically, we use a coherence length (also known as the Fried parameter r_0) of 17 cm, measured at wavelength of 500 nm and a zenith angle (η) of 0 degrees [85]. The resulting ratio of the diameter of the telescope aperture (D) to the atmospheric coherence length, a quantity typically used to characterize the strength of the atmospheric turbulence affecting the observations, is $D/r_0 = 21$.

Realizations of the wavefront perturbations incurred due to the propagation of the wavefront through the Earth's turbulent atmosphere, are generated using Kolmogorov statistics and a common Optical Path Difference (OPD) across the entire bandpass, employing the Fourier transform method [86]. A modified von Kármán power spectral density is utilized

$$PSD_{mvK}(\nu) = 0.023r_0^{-5/3} \frac{\exp(-\nu^2/\nu_m^2)}{(\nu^2 + \nu_0^2)^{11/6}}$$

where ν is spatial frequency in cycles/m, the inner and outer scale sizes are $l_0 = 1$ cm and $L_0 = 100$ m, respectively, $\nu_m = 0.942/L_0$, and $\nu_0 = 1/l_0$. We implement a 3-layer model for atmospheric turbulence, with layers at heights of 0 km, 7 km, and 12.5 km. The wind profiles for these layers are based on data from Mount Haleakala in May, as reported in [87]. We simulate observations at zenith angles of 0° and 30° . Since r_0 varies with the secant of the zenith angle [3], the level of turbulence for the observations at $\eta = 30^\circ$ is higher than for those at $\eta = 0^\circ$ by a factor of 1.15. For $\eta = 30^\circ$ the angular dispersion of an object is $+0.30''$ at 400 nm and $-0.38''$ at 1000 nm. This angular dispersion causes a wavelength-dependent spreading of the signal on the detector. Since some telescopes are equipped with dispersion correction optics to mitigate this effect, we investigate two scenarios: images acquired with and without dispersion correction optics.

For observations acquired with a telescope equipped with dispersion correction optics, we model the broadband data using

$$g(t) = \sum_{w=0}^{w=N_\lambda-1} \left\{ f \left[\lambda_{min} + \left(w + \frac{1}{2} \right) \Delta\lambda \right] \odot \sum_{m=0}^{m=N_{int}-1} h(\lambda_{min} + w\Delta\lambda + m\Delta\lambda_0, t) \right\}, \quad (3.1)$$

where $N_{int} = N_\lambda^0/N_\lambda$, $f(\lambda)$ is the object at wavelength λ , $h(\lambda)$ is the Point-Spread Function (PSF) at wavelength λ , and \odot denotes convolution. We define $\Delta\lambda_0$ and $\Delta\lambda$ using

$$\lambda_{max} - \lambda_{min} = N_\lambda^0 \cdot \Delta\lambda_0 = N_\lambda \cdot \Delta\lambda, \quad (3.2)$$

where N_λ^0 is the user defined number of spectral slices used to build the data, N_λ is the user defined number of spectral bands to be used in the recovery and λ_{min} and λ_{max} are the minimum and maximum wavelengths in the broadband observation, respectively. This is a variation of the spectral slicing approach of [88].

For observations without dispersion correction optics, the second term in Eqn. 3.1 becomes

$$\sum_{m=0}^{m=N_{int}-1} D(\lambda_{min} + w\Delta\lambda + m\Delta\lambda_0, \eta) h(\lambda_{min} + w\Delta\lambda + m\Delta\lambda_0, t), \quad (3.3)$$

where $D(\lambda, \eta)$ is a matrix operator that translates the monochromatic PSF depending on wavelength and zenith angle.

The extreme cases for Eqn. 3.1 are when $N_\lambda = N_\lambda^0$, and $N_\lambda = 1$. The former represents

$$g(t) = \int_{\lambda} f_{\lambda}(t) \odot h_{\lambda}(\eta) d\lambda,$$

and is the value used to build the data, while the latter represents

$$g(t) \simeq f_{BB} \odot h_{BB}(t), \quad (3.4)$$

where

$$f_{BB} = \int_{\lambda} f_{\lambda} d\lambda ,$$

and

$$h_{BB}(t) = \int_{\lambda} h_{\lambda}(t) d\lambda .$$

Fig. 3.1 shows that the approximation in Eqn. 3.4 is not unreasonable as a starting point for our recoveries.

$$g(t) = \int_{\lambda} f_{\lambda} \odot h_{\lambda}(t) d\lambda \quad g(t) \simeq f_{BB} \odot h_{BB}(t)$$

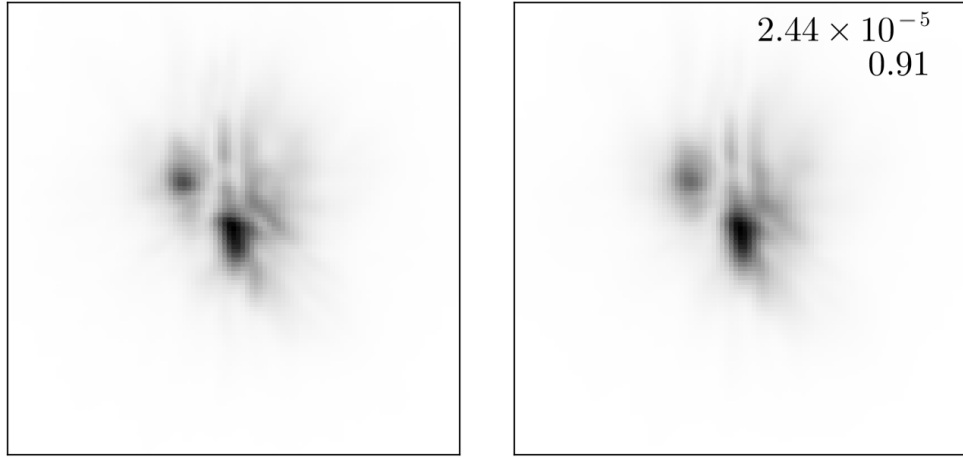


Figure 3.1 Left: A broadband image modeled using Eqn. 3.3 with $N_{\lambda} = 101$ for $\eta = 30^\circ$ and $r_0(500 \text{ nm}) = 17 \text{ cm}$ for data built with $N_{\lambda}^0 = 101$. Right: The broadband image modeled using $N_{\lambda} = 1$ with $N_{\lambda}^0 = 101$. The Root Mean Square Error (RMSE) (top) and Structural Similarity Index Measure (SSIM)_s (bottom) between the two images, defined in Eqn. 3.8 and 3.9, respectively, are shown in the upper right corner of the approximation in the right plot.

Additionally, the PSFs can be further expressed using a Fourier optics formulation

$$h(\lambda, t) = F [p(\lambda, t) \otimes p(\lambda, t)] ,$$

where F is the Fourier transform, \otimes denotes cross-correlation, and $p(\lambda, t)$ is the complex pupil function given by $p(\lambda, t) = A(\lambda, t) \exp[i \cdot \phi(\lambda, t)]$. In this work we assume effects from scintillation are negligible, i.e. $A(\lambda, t) \approx 1$. The phase $\phi(\lambda, t)$ can be expressed as

$$\phi(\lambda, t) \simeq \sum_{l=1}^{N_{layers}} E(\lambda, t, l) \frac{2\pi W(l)}{\lambda}, \quad (3.5)$$

where N_{layers} is the number of atmospheric layers, $W(l)$ is the OPD of layer l , and $E(\lambda, t, l)$ is the matrix operator that extracts the appropriate region of layer l at wavelength λ and time t . Once these OPDs are generated they are degraded to match the performance one would obtain from an Imaging Shack-Hartmann wavefront sensor for the atmospheric conditions, as per [89].

The assumption of an OPD that is invariant to wavelength is, of course, a simplification. The index of refraction of the atmosphere is a weak function of wavelength. As OPD is calculated as the integrated index of refraction along the optical path, OPD also has a weak dependence on wavelength. However, if our wavefront sensor measures the wavefront phase at a wavelength near the mid-point of our spectral bandpass of 400 nm to 1000 nm, we expect the error induced by using the approximation of a constant OPD to be small and significantly less severe than the effects of atmospheric turbulence [90].

For this work we simulate a generic model satellite, which we only loosely base on a typical satellite in Low Earth Orbit (LEO), simulated at a range of 515 km with dimensions 60 cm \times 12 cm ($0.25'' \times 0.05''$)¹ and is composed of three materials: anti-reflection coated

¹We note that a typical satellite in LEO is much larger than this, constituting fields of view tens of arcseconds in size. For this study, however, we choose to simulate the lowest limit of what would be observed in LEO as a proof of concept.

solar panel [91], Kapton, and Aluminized Mylar [92]. The latter two materials also include their aged counterpart, corresponding to the particle fluence and UV irradiation encountered in LEO over an 11 year period [93]. A LEO satellite in orbit for 11 years represents the most extreme weathering a LEO satellite might experience, and thus the largest changes in its materials' reflectance spectra. This satellite is assumed to reflect a solar spectrum modulated by each material's reflectance. We artificially brighten our toy satellite to a magnitude of mag+4 in our passband². The signal is then detected by a typical sCMOS detector with an $8'' \times 8''$ Field of View (FOV). The final observed spectrum for each material, Solar spectrum, Quantum Efficiency (QE) curve, and location of each material on the satellite can be seen in Fig. 3.2.

To simulate broadband observations, we generate $N_t = 102$ speckle imaging frames (5 ms exposure time) using Eqn. 3.1 and 3.2 at $N_\lambda^0 = 101$ equally-spaced wavelengths ($\Delta\lambda = 6$ nm) between 400 – 1000 nm, where the data are Nyquist sampled at 400 nm. This wavelength range was chosen because it encompasses the typical sensitivity range of a silicon detector (see upper right panel of Fig. 3.2). We incorporate dispersion effects using the model described in [94] and [95] to calculate the shift in position of the images on the detector with wavelength ($D(\lambda, \eta)$ in Eqn. 3.3) and to calculate the ray trace with wavelength through the atmospheric layers ($E(\lambda, t, l)$ in Eqn. 3.5). For reference, Eqn. 4 from [95] gives the atmospheric differential refraction $\Delta\theta$ in arcsec ('') as

$$\Delta\theta(\lambda) \approx 206265 [n(\lambda) - n(500 \text{ nm})] \tan(\eta) ,$$

²We define our magnitude zero-point using the integrated flux of Vega at the top of the atmosphere across our passband.

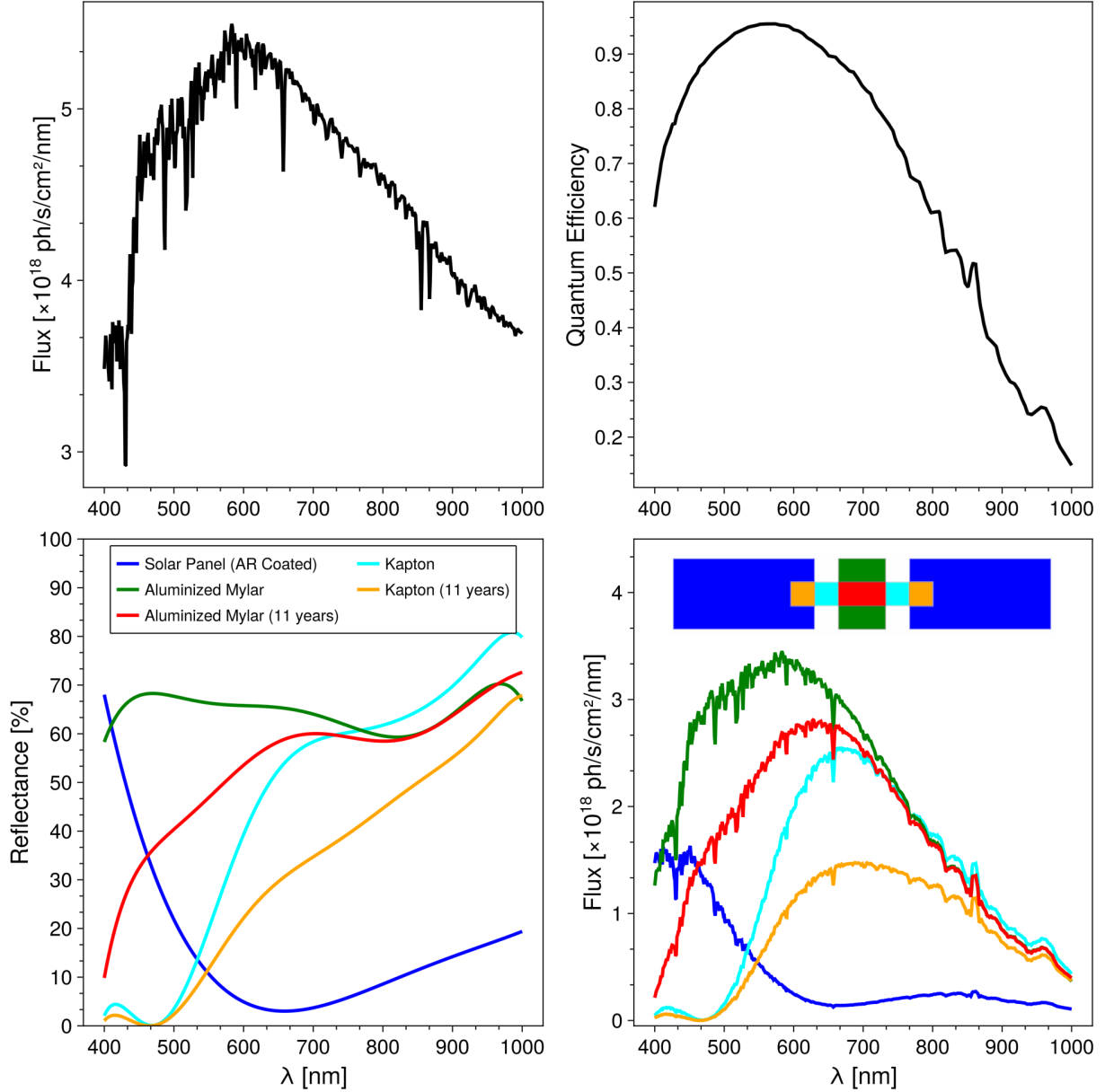


Figure 3.2 (top left) Solar spectrum as observed by the Hubble Space Telescope [2]. (top right) QE curve for our simulated detector, based on the Photometrics Teledyne Prime-95b sCMOS camera. (bottom left) Reflectance spectra for three different materials and two of their aged counterparts. (bottom right) After considering the factors mentioned above, the final, optimally observed spectrum for each material, and, at the top of the panel, a color-coded schematic showing the location of each material on the satellite.

where $n(\lambda)$ is the refractive index at wavelength λ and η is the zenith angle. The refractive index is calculated from Eqn. 2 and 3 of [95] assuming an air temperature of 15° C, air pressure of 760 mm Hg, and water vapor pressure of 8 mm Hg. Temporal correlations are enforced by assuming a frozen flow for each atmospheric layer [96]. A subset of five of the 101 monochromatic frames used to build a single broadband image is shown in Fig. 3.3.

Finally, to provide a baseline for comparison, we simulate a multi-spectral observation (five wavebands) of the satellite from a hypothetical space-based telescope of the same diameter. These data represent diffraction-limited resolution observations, i.e., observations free from the effects of atmospheric turbulence.

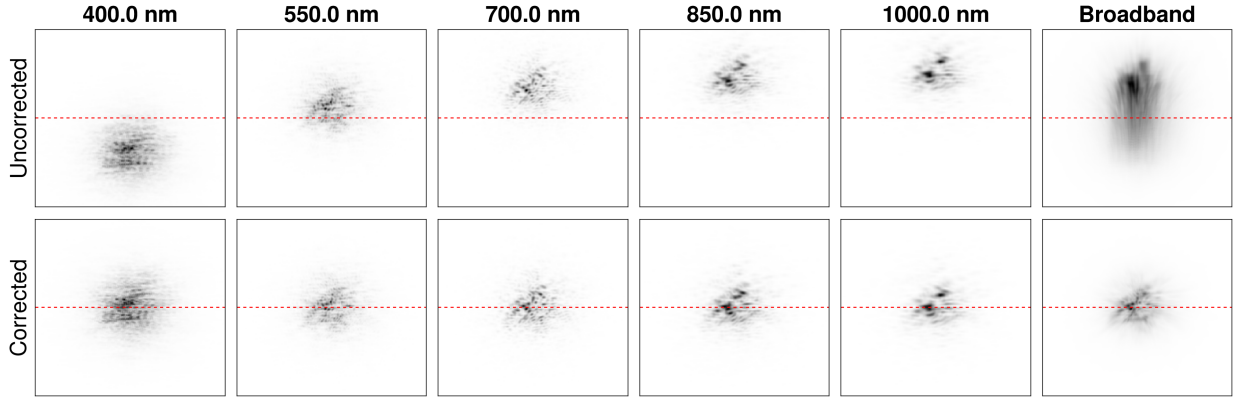


Figure 3.3 Five monochromatic images from the 101 images generated between 400 nm and 1000 nm that, when integrated, produce a single broadband frame (right-most image). Observations are simulated with a 60° zenith angle to demonstrate dispersion from the atmosphere (top row), where the shortest wavelength (400 nm) sees the largest effect. Dispersion is calculated relative to 500 nm, shown as a dashed red line. The direction of dispersion is taken to be the vertical axis in the images and the attitude of the satellite is shown in the bottom right panel of Fig. 3.2. The bottom row shows the same frames but when a dispersion corrector is used. In both cases, the monochromatic images at each wavelength are identical, but the broadband images are vastly different.

Numerically, the object and OPDs are reconstructed and updated by minimizing the

criterion

$$\epsilon = \sum_t \sum_{x,y} \omega(t) [g(t) - d(t)]^2 ,$$

where $d(t)$ is the measured broadband image for time t ; the inner summation is the pixel sum of the weighted residuals, and $\omega(t) = \{s(t) [g(t) + \sigma_{RN}^2]\}^{-1}$ is the weight of each frame, containing a Gaussian read-noise term σ_{RN}^2 , a Poisson noise term $g(t)$ (the model image of frame t), and the information entropy $s(t) = -\frac{d(t)}{\sum d(t)} \log_2 \left(\frac{d(t)}{\sum d(t)} \right)$ of the data frame. By incorporating entropy into the weighting, we ensure that frames containing the most information content (i.e., least blurred) are more heavily weighted. Minimization is performed using the quasi-Newton Variable Metric Limited Memory Bound (VMLMB) method from `OptimPackNextGen.jl`³.

3.3 Analysis Method

The number of variables needed to describe the object at N_λ wavelengths, using a pixel basis set is

$$N_{var}^{obj} = N^2 N_\lambda ,$$

where N is the number of pixels along one side of a square array. The number of variables needed to describe the PSFs, assuming we are modeling PSFs from a set of OPDs for each layer of turbulence, and a pixel basis set, is given by

$$N_{var}^{PSFs} = \sum_{l=1}^{N_{layers}} \pi \left(\frac{N}{4} \right)^2 + \pi \left(\frac{N}{2} \right) v_l N_t ,$$

³<https://github.com/emmt/OptimPackNextGen.jl>

where the summation is over N_{layers} atmospheric layers, v_l is the velocity of the l^{th} layer in pixels/frame, and N_t is the number of broadband images in the data set. The number of measurements is given by

$$N_{meas} = N^2 N_t .$$

The ratio of the number of variables to the number of measurements $R_{v:m}$ is given by

$$R_{v:m} = \frac{N^2 N_\lambda + N_{layers} \pi \frac{N^2}{16} + \pi \frac{N_t N}{2} \sum_{l=1}^{N_{layers}} v_l}{N^2 N_t} . \quad (3.6)$$

To provide an over-determined system with more measurements than unknowns, we need

$$\frac{N_\lambda + \frac{N_{layers} \pi}{16}}{N_t} + \frac{\pi}{2N} \sum_{l=1}^{N_{layers}} v_l < 1 . \quad (3.7)$$

For our numerical experiment, $N = 512$, $N_\lambda = 20$, $N_t = 102$, $N_{layers} = 3$, $v_1 = 1.78$ pixels/frame, $v_2 = 2.45$ pixels/frame, $v_3 = 12.16$ pixels/frame, $D = 3.6$ m, and $t_{exp} = 5$ ms.

For the spectra of the materials represented in this study (see lower right plot in Fig. 3.2), a recovery at $N_\lambda = 20$ wavelengths is sufficient to capture the morphology of the spectra and satisfies the condition in Eqn. 3.7 with $R_{v:m} = 1/4$, meaning there are 4 measurements for each unknown and ensuring our system is not underdetermined. N_λ can be increased to capture finer details in the spectrum, however, this increases the value of $R_{v:m}$, which we want to minimize, and provides little in the way of additional information for the smoothly-varying material spectra used in this study.

We use the technique of Multi-Frame Myopic Deconvolution (MFMD) [97, 98] to recover the grey object f_{BB} from Eqn. 3.4, using the degraded wavefront estimates from the wavefront sensor to generate estimates of the spectrally-integrated PSFs. Using this approximation at

the beginning of the recovery allows us to gain traction on the morphology of the object before attempting to recover detailed spectral information. When we start recovering spectral information on the object we slowly increase the value of N_λ from 1 to its final value as the recovery progresses. This process ensures that the large-scale structures in the spectrum are captured before high-frequency content is allowed into the recovery process. The final N_λ desired is determined both by the Signal-to-Noise Ratio (SNR) in the data and the complexity in the material spectra. [99] note that in low-SNR environments the act of smearing signal across the detector with wavelength further reduces the SNR, which can be detrimental to the problem if the smearing is severe.

It is important to avoid overfitting of the object since there are imperfections in the wavefront. However, information on the wavefront is still encoded in the broadband speckle images. In Multi-Frame Blind Deconvolution (MFBD) the data frames are assumed to be temporally linked by the frozen-flow nature of the atmosphere [96], allowing us to update the atmospheric layers on “sausages” that the pupil scrolls across. Using the recovered grey object, we perform short, alternating recoveries of the wavefront OPD and object, slowly increasing N_λ , until the solution converges and we reach the target N_λ .

In all cases, we measure the success of our method by calculating the normalized Root Mean Square Error (RMSE) between the truth object f_λ and recovered object \tilde{f}_λ at each wavelength. We calculate the RMSE as

$$RMSE = \sqrt{\frac{1}{N^2} \sum_{x,y} \left(\frac{\tilde{f}_\lambda - f_\lambda}{\sum_{x,y} f_\lambda} \right)^2}, \quad (3.8)$$

where N is the number of pixels along one side of the object array and $\sum_{x,y} f_\lambda$ is the flux of the truth object at wavelength λ . RMSE sometimes does not match well with human perception so we also choose to compute the mean Structural Similarity Index Measure (SSIM) [69] across all wavelengths between the truth (f) and recovered (\tilde{f}) objects. Since we are most interested in changes in morphology we chose only to compute the structure term of the SSIM, given below as $SSIM_s$. Typically, SSIM is calculated across small windows of the images by Eqn. 3.9 after being convolved with a small Gaussian kernel, and these SSIM values are averaged together.

$$SSIM_s(f, \tilde{f}) = \frac{\sigma_f \tilde{f} + c_3}{\sigma_f \sigma_{\tilde{f}} + c_3} \quad (3.9)$$

where f and \tilde{f} are first normalized to the same maximum value so that their values lie between 0 and 1, σ^2 represents the variance of the quantity, and $c_3 = 0.03^2/2$ for floating point numbers [70]. For this work, we choose a window size of 11×11 pixels and a Gaussian of $FWHM = 1.5$ pixels to convolve the inputs of Eqn. 3.9 with. A perfectly recovered object would yield an SSIM of 1, while a value of 0 indicates no structural similarity. This metric is particularly adept at measuring differences in *perceived* structure of images, and can reveal subtle differences even when two distinct images give the same RMSE when compared to the ground truth. Each metric has its strengths and so we report both metrics for all of our results.

In this work we report the recovered object morphology at 5 selected passbands around 400 nm, 550 nm, 700 nm, 850 nm, and 1000 nm. We also examine the spectrum of each pixel at all $N_\lambda = 20$ wavelengths, as compared to the spectra for the truth object and the

diffraction-limited case. Finally, we remove the solar spectrum and QE curve and combine the pixel spectrum of each respective material to assess our recovery of each material’s reflectance. For these experiments we incorporate read noise ($\sigma_{RN} = 2 e^-$) and photon (“shot”) noise (the target brightness is mag +4) into the simulation. Furthermore, the wavefronts used in the reconstructions are assumed to have come from a scene-based (“imaging”) Shack-Hartmann wavefront sensor with 6×6 sub-apertures across the entrance pupil, and have an RMSE of ~ 0.35 rad at 500 nm when compared to the truth wavefronts. This provides a realistic estimate of the recovered wavefronts from a focal plane wavefront sensor, as per [89].

3.4 Results

The diffraction-limited data, which are free from the deleterious effects of atmospheric turbulence, provide a benchmark against which we can evaluate our hyper-spectral imaging results. These benchmark data, which are shown in the middle row of Fig. 3.4, show a decreasing fidelity of the object’s morphology as the wavelength increases due to the effects of diffraction. Quite simply, information on the high-spatial frequencies of the object becomes increasingly depleted as the observing wavelength increases (see images in the right-hand column of Fig. 3.5).

The recoveries for the noisy, degraded wavefronts experiment, shown in the bottom row of Fig. 3.4, also demonstrate a degradation in the morphology of the recovered object with increasing wavelength. However, the recovered morphology here is superior to that measured

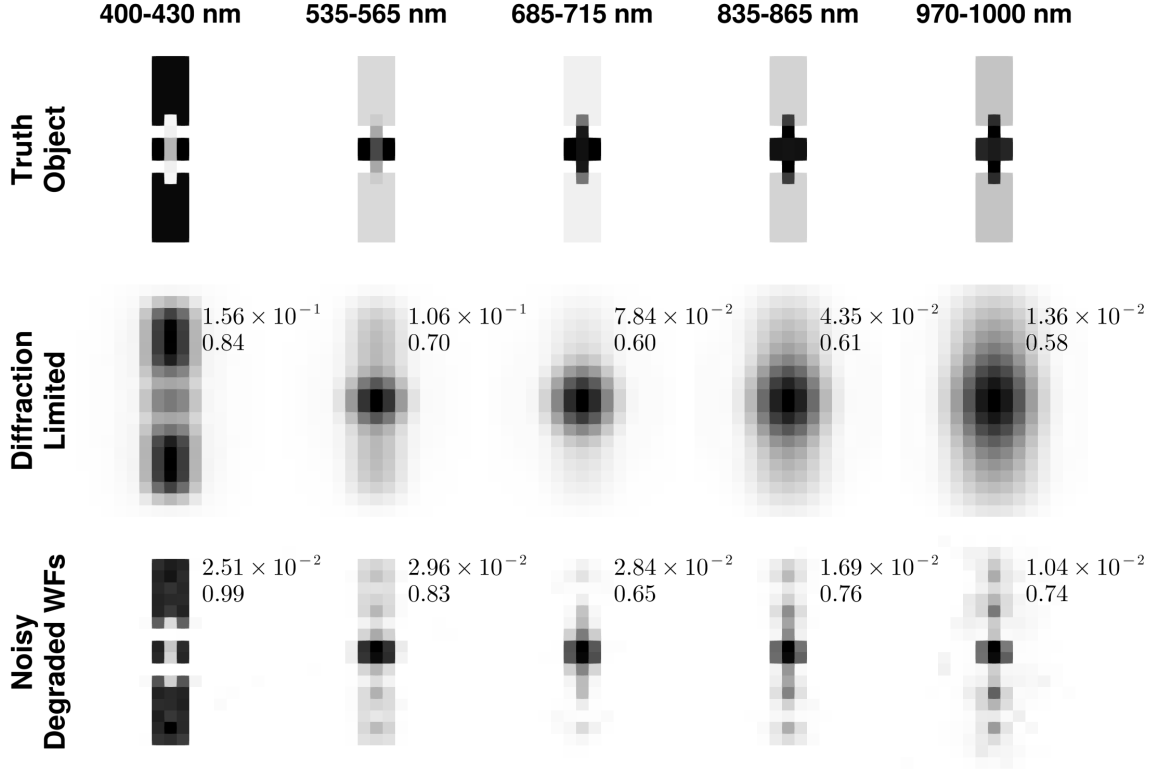


Figure 3.4 The top row shows the truth object for five selected wavebands from the 20 wavebands that were used to build the broadband images. The middle row presents the corresponding theoretical diffraction-limited resolution images. The bottom row depicts the recovered objects from simulated ground-based observations taken at zenith, through a combined atmospheric turbulence of $D/r_0 = 21$. The ground-based observations incorporate Gaussian read noise ($\sigma_{RN} = 2 e^-$), shot noise for a magnitude +4 target brightness, and the restoration used estimated wavefronts from a Shack-Hartmann wavefront sensor. The recovery process reduces this wavefront error from 0.33 rad in the composite wavefront to 0.22 rad at 500 nm. The RMSE and SSIM, computed using Eqn. 3.8 and 3.9, respectively, are shown to the upper right of the recovered object at each wavelength.

in the diffraction-limited resolution images. The improvement in fidelity is directly related to the improved amplitudes of the spatial frequencies below the cutoff frequency and some partial super-resolution (see the middle column of images in Fig. 3.5). It is well-known that non-linear image restoration algorithms demonstrate the ability to recover spatial fre-

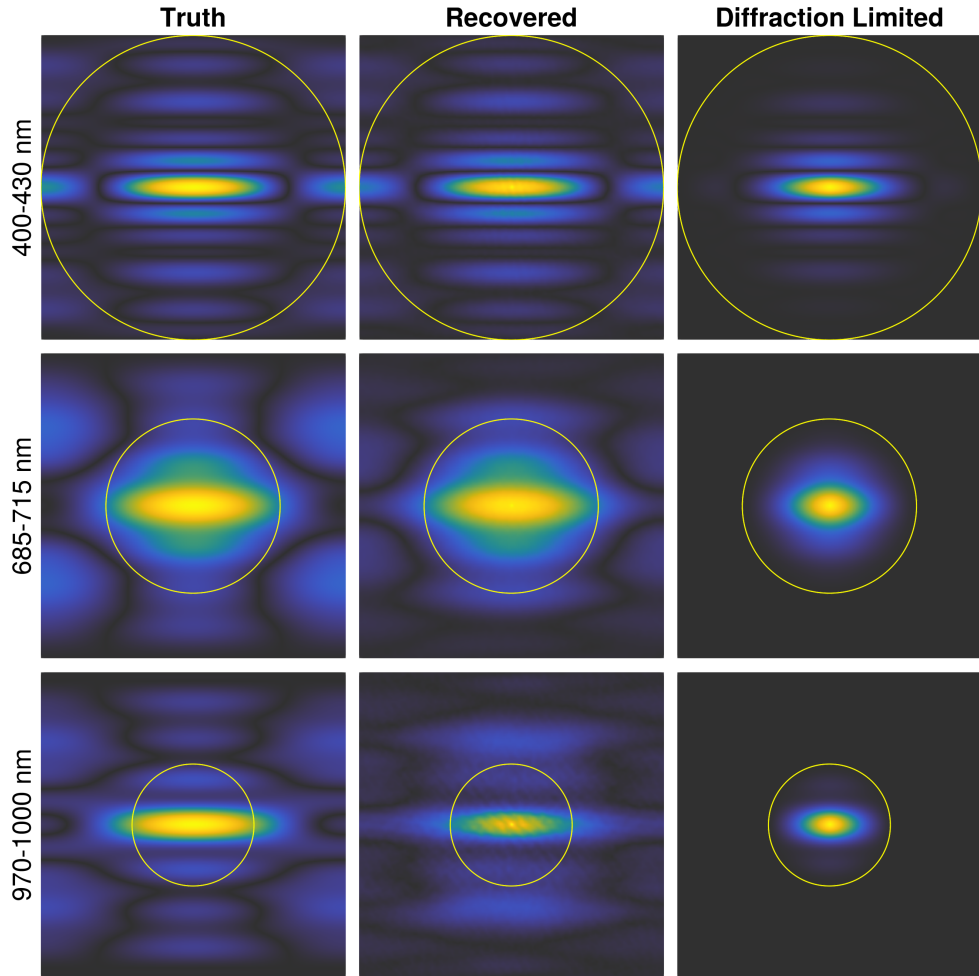


Figure 3.5 Power spectrum of the truth object (left), recovered object (center), and diffraction-limited object (right) at wavebands $400 - 430$ nm (top row), $685 - 715$ nm (center row), and $970 - 1000$ nm (bottom row) for observations taken at zenith with Gaussian read noise, shot noise, and with degraded wavefronts. The cutoff frequency at each wavelength is plotted in all three plots as a yellow circle. Within the cutoff frequency, we are recovering spatial frequencies in the object to their true amplitudes. Additionally, we see some meaningful recovery of spatial frequencies outside of the cutoff frequency. However, the discrepancies between the true and recovered spatial amplitudes increase with wavelength, particularly near and beyond the cutoff frequency. This is due to the reduction in spatial information available in the data as the wavelength increases. These discrepancies lead to artifacts in the recovered morphology, which in turn result in errors in the recovered spectra.

quency information beyond the Rayleigh diffraction limit for objects of finite extent, through bandwidth extrapolation (or “analytic continuation”; Lucy 100) . The amount of additional information recovered is contingent upon the SNR of the data and the accuracy of the PSF estimates. Even in cases where the SNR is insufficient to produce super-resolution effects in the recovered image, these algorithms can still enhance spatial frequencies within the diffraction cut-off frequency. This enhancement is clearly evident in Fig. 3.5.

As the morphological accuracy of the recovered object improves, spectral mixing in the recovered hyperspectral signal, caused by residual image blur and reconstruction artifacts, decreases. The spectrum of each pixel in the satellite is shown in Fig. 3.6. The effects of this mixing are most damaging in regions of the target where its materials are changing quickly with spatial location, i.e., the bus of the satellite. This effect can be clearly seen in the recovered spectra from our diffraction-limited resolution images (see dotted lines with star markers in Fig. 3.7). Here the recovered spectra for Kapton and Mylar are almost indistinguishable from each other, show almost no variation with aging, and bear little resemblance to the truth spectra. Whereas the spectrum for the solar panel material, where the target has a relatively large number of contiguous pixels of the same material in two areas, shows a striking similarity to the true spectrum for the material. Contrasted with the recovered pixel spectra in Fig. 3.6 and the recovered material spectra in Fig. 3.7, it is clear to see that reducing spatial smearing is crucial for recovering accurate spectra.

As dispersion acts like a prism in spreading the signal across the detector we were expecting to see an improvement in the recovery for data acquired at non-zero zenith angles

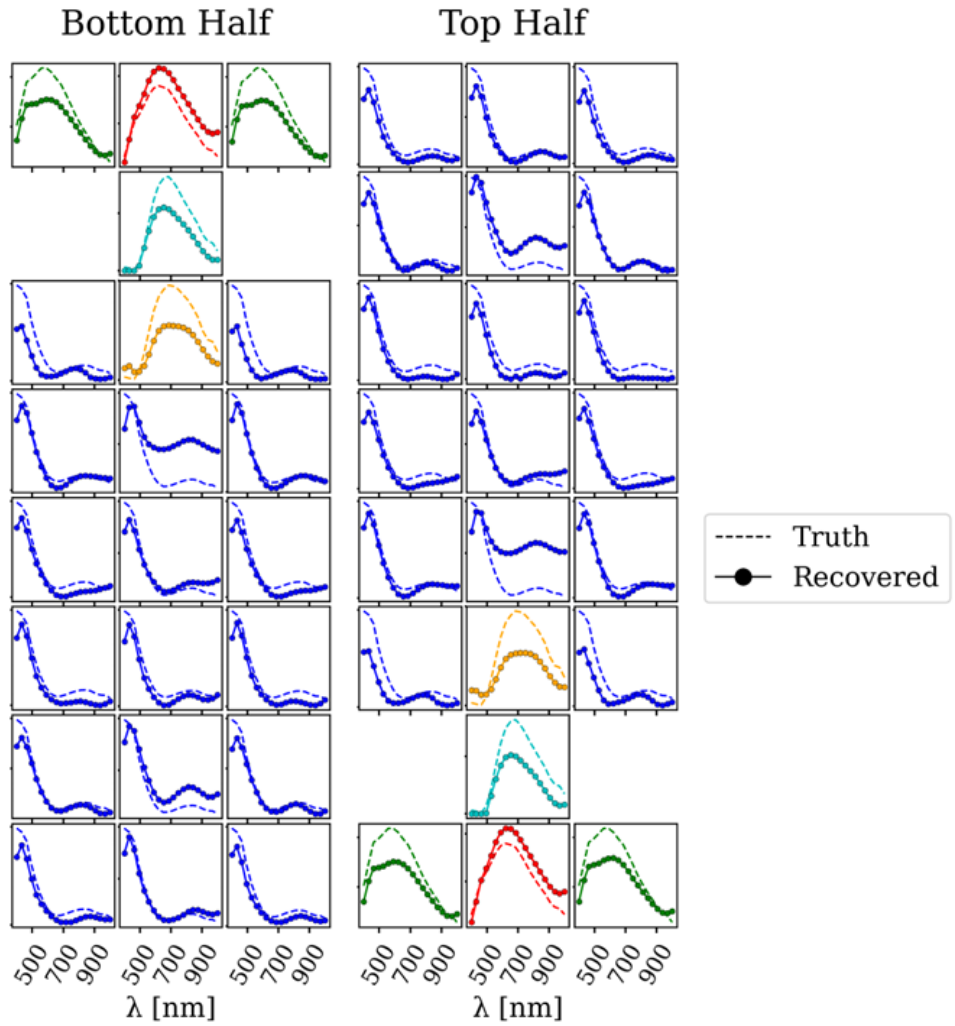


Figure 3.6 Recovered spectrum of each pixel in the object at 20 wavelengths (solid line) for noisy frames, degraded wavefronts, and observations at zenith ($\eta = 0^\circ$). The bottom half of the satellite is shown on the left and the top half on the right. Truth spectra are shown as dashed lines (and in the right panel of Fig. 3.2). Colors correspond to the materials in Fig. 3.2. Discrepancies in the recovered spectra around the bus of the satellite (center of figure) are the result of spatial mixing of adjacent pixels. Mixing increases towards larger wavelengths due to the loss in resolution.

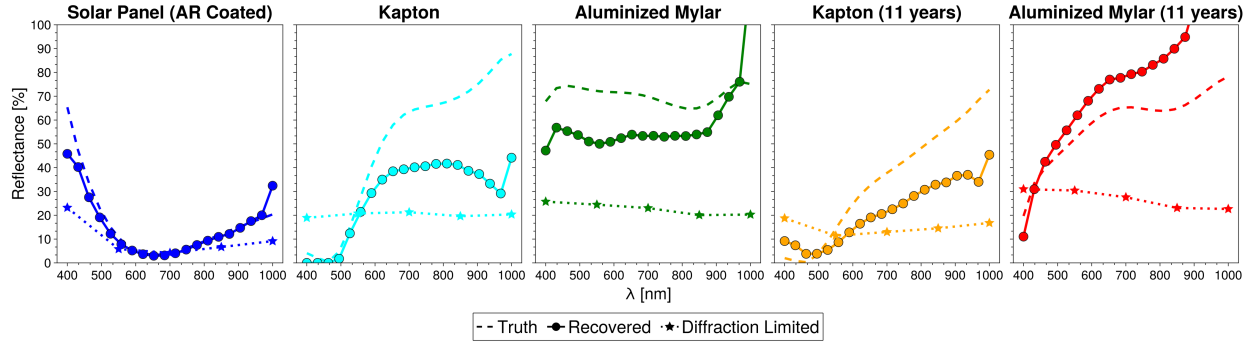


Figure 3.7 Mean, recovered material reflectance for observations taken at zenith angle $\eta = 0^\circ$ where the frames are corrupted by read noise and shot noise, and the initial wavefronts estimates possess 0.332 ± 0.004 rad of wavefront error at 500 nm when compared to the truth. The initial wavefront estimates are updated in the recovery process and contain 0.217 ± 0.009 rad wavefront error at 500 nm at the end of the recovery process. The recovery was performed for $N_\lambda = 20$. These spectra are obtained by averaging all of the pixel spectra for each material and removing the solar spectrum and QE curve. The shaded region represents the standard-deviation of the mean RMSE for recoveries made with four different time series of data, each performed with $N_t = 102$. The truth spectra are shown by the dashed lines and the theoretical diffraction limited results for a 5-channel multi-spectral imager are shown as dotted lines with star markers.

without dispersion correction optics, despite the reduced SNR with smearing. We therefore studied the performance of our restoration algorithm for observations taken at a zenith angle of $\eta = 30^\circ$ without dispersion-corrective optics and with dispersion correction. What we found (see Fig. 3.8) was counter to our expectations: the fidelity of the recovery made with the corrected data was better than that obtained with the uncorrected data. The likely reason for this difference is the lower SNR value of the latter due to the spreading of the signal [99].

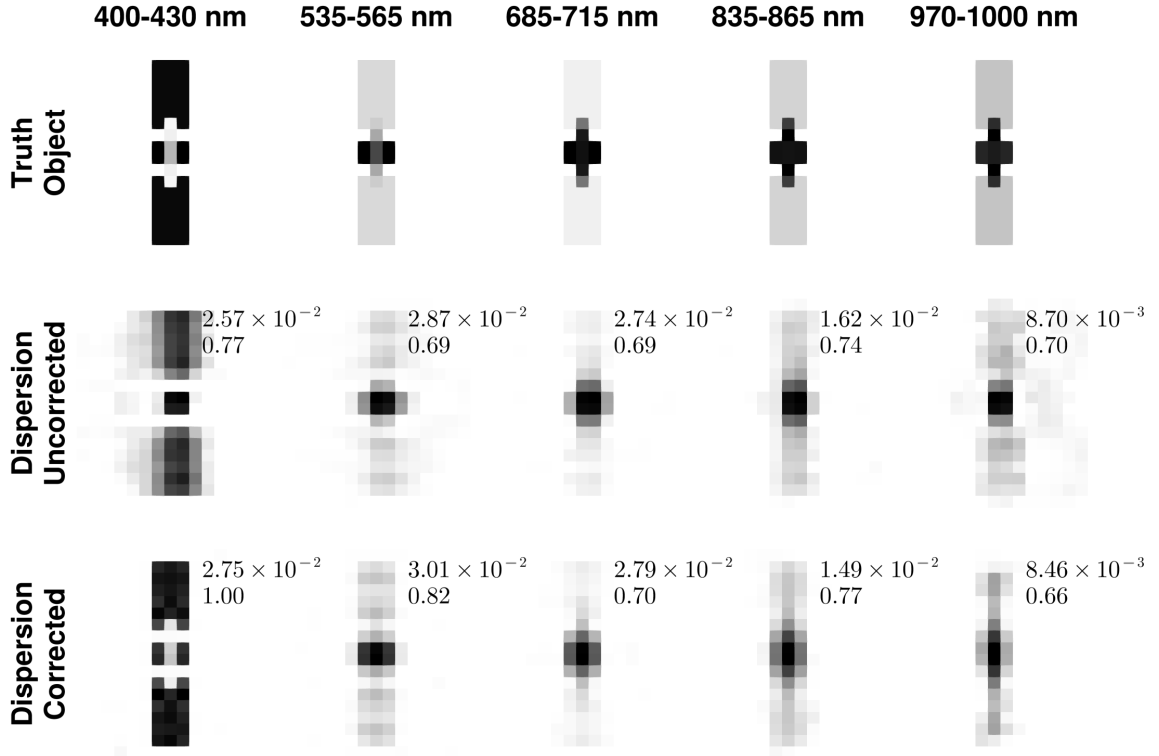


Figure 3.8 Recovered object at 5 wavebands for observations taken at $\eta = 30^\circ$ with both Gaussian read noise and shot noise present, and with degraded wavefronts. The top row shows the truth object, the middle row shows the recovered object when dispersion is not corrected-for at the detector, and the bottom row shows the recovered object when a dispersion corrector is used. The RMSE and SSIM, computed using Eqn. 3.8 and 3.9, respectively, are shown to the upper right of each recovered object slice.

3.5 Discussion & Conclusion

We have used numerical simulations to show that hyperspectral speckle imaging has the potential to be a viable tool for extracting wavelength information from resolved targets and recovering the reflectance spectrum of each pixel in the recovered object. This capability

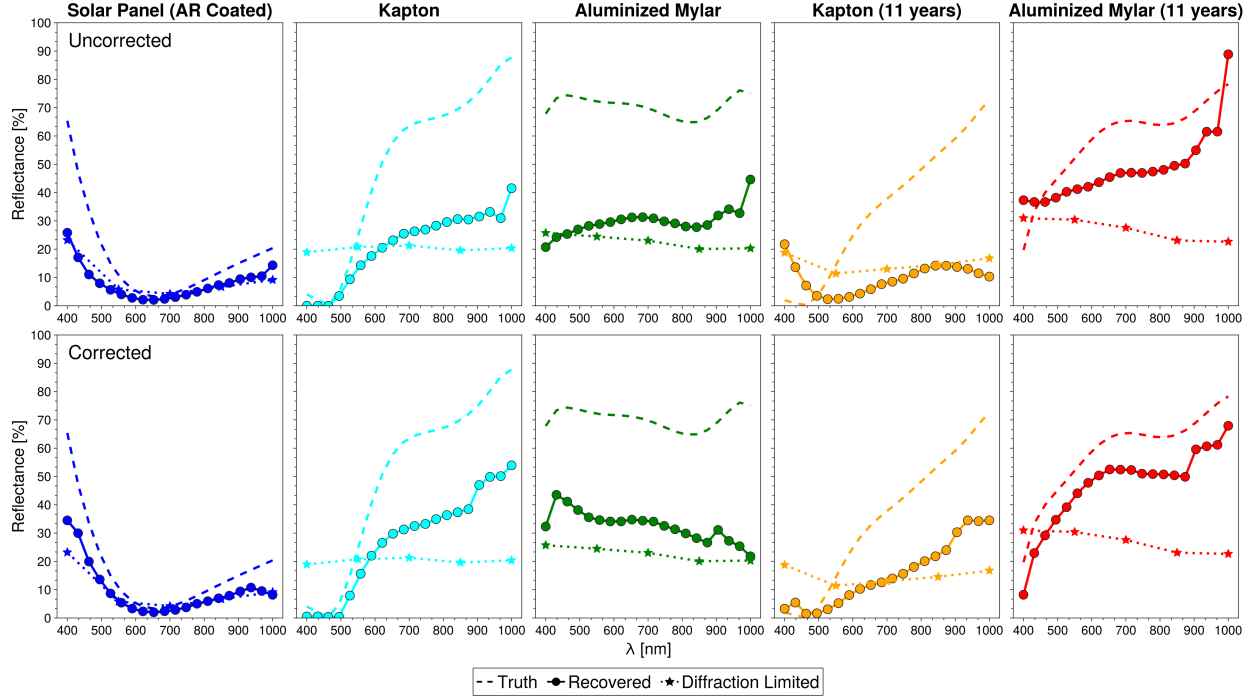


Figure 3.9 Mean, recovered material reflectance for observations taken at zenith angle $\eta = 30^\circ$ where the frames are corrupted by read noise and shot noise, and the initial wavefronts estimates possess 0.33 rad of wavefront error at 500 nm when compared to the truth. The initial wavefront estimates are updated in the recovery process and contain 0.21 rad wavefront error at 500 nm at the end of the recovery process. The recovery was performed for $N_\lambda = 20$. These spectra are obtained by averaging all of the pixel spectra for each material and removing the solar spectrum and QE curve. The truth spectra are shown by the dashed lines and the theoretical diffraction limited results for a 5-channel multi-spectral imager are shown as dotted lines with star markers.

could pave the way for ground-based materials identification and improved characterization of satellites in the near-Earth environment, and could lead to advances in aging studies. These results, however, serve as a proof-of-concept and will be followed-up with on-sky measurements of resolved targets in LEO, such as the numerous Starlink satellites since they have simple compositions (mainly solar panel).

To recover spectra that closely demonstrate the wavelength behavior associated with the

underlying material, we need to minimize spectral mixing caused by spatial blurring and reconstruction noise in the recovered image. Even measurements acquired with diffraction-limited resolution suffer from significant distortion due to the spatial blur in the image from diffraction. With accurate estimates for the PSFs we can recover an estimate of the target object with high-spatial frequencies (inside the cut-off frequency) that have amplitudes closer to the true amplitudes than are available in diffraction-limited resolution observations. We have shown that allowing the wavefronts to update in our recovery process improved the wavefront error by 37%. This improvement in the wavefront error directly translates into improved morphology in the recovered target object. The results from [89] are for the case of monochromatic wavefront sensing, but we suspect that higher-fidelity wavefronts can be obtained using *broadband* wavefront sensing. This is due to dispersion in the atmosphere causing the light at different wavelengths to sample the upper atmospheric layers differently. This slightly different sampling of the upper layers with changing wavelength should allow for improved sampling of these layers, analogous to the sub-sampling of the wavefront achieved by incorporating frozen flow behavior into the modeling of the wavefront [101].

The results presented here are constrained only by imposing positivity on the recovered object. However, additional regularization on both the object morphology, using total-variation regularization, and the pixel spectrum, through a cross-spectral regularizer, would provide a means for improved performance. Proper implementation of a total variation regularizer, however, requires the shift to a proximal splitting framework, such as ADMM [73], or its more recent extension, bSDMM [74]. These proximal splitting frameworks are conve-

niently adept at parallelizing large problems of this sort, potentially allowing for networks of computers to process these data on more-feasible timescales.

Our results are simulated for moderate turbulence, however, r_0 scales with the zenith angle η as $r_0 \propto \sec \eta$, where at 60° the effects of turbulence are effectively double that at $\eta = 0$. Realistically, the ability to perform recoveries through strong turbulence means that a larger portion of the sky is accessible to our technique. To recover material spectra through these turbulence levels, thought must be given to the way data are acquired. One proposed paradigm is that of [102], where the telescope’s aperture is partitioned into a set of annuli. Each annulus probes a region of the target’s power spectrum and allows for “bootstrapping” through spatial frequencies by individually introducing apertures into the reconstruction one by one. In their analysis they found noticeable improvements in a recovered monochromatic object with a multi-annulus scheme over a single aperture through strong turbulence. Further improvements to this technique have been proposed by [103] where the particular size of each aperture is carefully selected to maximize the speckle transfer function of the observing conditions.

Finally, the wavelength range over which we probed corresponds to the range of sensitivity for silicon-based detectors. However, the wavelength range of our observations can be extended to 400 nm – 1700 nm by using a new high sensitivity SWIR image sensor, such as the Sony IMX991⁴, that uses a combination of InGaAS photodiodes and silicon readout circuits to achieve a broader spectral range.

⁴<https://www.sony-semicon.com/en/products/is/industry/swir/imx990-991.html>

3.6 Table of Variables

Below is a table containing each variable used in this chapter and a short description of that variable.

$\overline{(\dots)}$	Complex conjugate
\odot	Convolution operator
\otimes	Correlation operator
$(\cdot)^T$	Matrix transpose
c_3	Constant used in the SSIM calculation
$d(t)$	Observed image for time t
D	Diameter of telescope
$D(\lambda, \eta)$	Dispersion operator at wavelength λ and zenith angle η
$\Delta\lambda$	Wavelength bandpass
$\Delta\theta(\lambda)$	Change in position in arcsec (") due to atmospheric diffraction at wavelength λ
$E(\lambda, t, l)$	Operator that selects the region of layer l at wavelength λ and time t
ϵ	Cost function
η	Zenith angle
f_{BB}	Broadband approximation of the object
f_λ	Object at wavelength λ
\tilde{f}_λ	Object estimate at wavelength λ
F	Fourier transform operator
$g(t)$	Model image a time t
h_{BB}	Broadband approximation of the PSF
$h_\lambda(t)$	PSF at wavelength λ for time t
$\text{Im}\{\dots\}$	Imaginary part of input
λ	Wavelength
$\bar{\lambda}$	Mean wavelength
m	Index of number of wavelengths to integrate over per passband
$n(\lambda)$	Index of refraction at wavelength λ
N	Number of pixels along one side of the image
N_{int}	The number of wavelengths to integrate per passband
N_λ	Number of wavebands used in the recovery process
N_λ^0	Number of wavebands used in data generation
N_{layers}	Number of atmospheric layers

- N_{meas} Number of measurements
 N_{var}^{obj} Number of variables needed to express the object in the recovery process
 N_t Number of observations
 ν Spatial frequency
 ν_m Outer scale spatial frequency
 ν_0 Inner scale spatial frequency
 $\omega(t)$ Statistical weight of observation at time t
 PSD_{mvk} modified von Kármán power spectral density
 $p(\lambda, t)$ Complex pupil function at wavelength λ and time t
 $\phi(\lambda, t)$ Complex wavefront phase at wavelength λ and time t
 r_0 Fried parameter
 $R_{v:m}$ Ratio of the number of variables to the number of measurements
 $\text{Re}\{\dots\}$ Real part of input
 $RMSE$ Root Mean Square Error
 $s(t)$ Information entropy for observation at time t
 $SSIM_s$ Structure term of the SSIM calculation
 σ_f Variance of the truth object
 $\sigma_{\tilde{f}}$ Variance of the recovered object
 $\sigma_{f\tilde{f}}$ Covariance between the truth and recovered objects
 σ_{RN} Read noise
 t Time
 v_l Wind velocity of layer l in pix/frame
 w Wavelength index
 $W(l)$ OPD of layer l

CHAPTER 4

Optics Experiments for Speckle Imaging

This chapter marks the step from the realm of digitally-simulated photons (and their associated noise) to real, physical photons and real detectors. It is broken into two main sections 1.) the building of an atmospheric turbulence simulator, named Advanced Reconnaissance of Earth-orbiting Satellites (ARES), and the experiments that it is feeding and 2.) the building and commissioning of a 2-channel broadband speckle imaging instrument.

4.1 ARES Turbulence Simulator

The algorithms and methods presented in Chapters 2 and 3 are benchmarked by their ability to recover a *known* object under *known* turbulence. On sky it is difficult to truly test the performance of an instrument without knowing what the true conditions were at the time of observation. Furthermore, we lose the luxury of knowing the true morphology of the target, in the case of satellites in Low Earth Orbit (LEO). Benchtop turbulence simulators provide exactly the right controlled environment to test new instruments and algorithms. Historically, turbulence has been generated in the laboratory by either 1.) altering the temperature and wind in the beam path with heating elements and fans [104] or 2.) introducing a transparent material to the beam [105, 106]. The first method produces accurate turbulent conditions at the expense of repeatability. The exact turbulence cannot be replicated exactly. The second method uses glass plates that are either coated in hair spray [105] or inscribed with phase screens that match Kolmogorov statistics [107]. The downside to these plates is that they require expensive, precise fabrication and only provide a single instance

of the atmosphere. They can be spun to simulate an evolving atmosphere. [108] showed that an optical system with phase plates can be tuned to provide the required atmospheric characteristics. State-of-the-art turbulence simulators, however, opt to use Spatial Light Modulators (SLMs) because of their dynamic nature and adaptability [109]. Phase screens can be updated on the fly to resemble translating and boiling phase screens. For this reason, we have chosen to create an atmospheric turbulence simulator based around a set of SLMs. As a refresher, SLMs operate by applying a voltage to a lattice of liquid crystals, causing the crystals to change orientation, which then changes the index of refraction in that region. This imparts a phase change to the incident wavefront. Specifically, we use Meadowlark Optics 1920×1152 pixel High-Speed SLMs, which have $9.2 \mu\text{m}$ pixels and can switch phase screens at frequencies up to 555 Hz. They operate by simply uploading a bitmap image to the device with the phase to be imparted on the beam.

4.1.1 Optical Design

Prior to ARES there is a dual-source laser module, seen in Fig. 4.1. This laser module is composed of a fixed, on-axis source and an off-axis source on a translation stage. Each source is paired with a linear polarizer and half-wave plate for polarization and brightness control. The two sources are then combined using a beam splitter and collimated with a collimating lens. Finally, the beam is ~ 40 mm in diameter and placed on an aluminum plate with a pair of circular, 10 mm apertures that produce two independent 10 mm beams for ARES to utilize. These beams are used to build two identical “legs” of ARES that each function as an independent turbulence generator in the experiments.

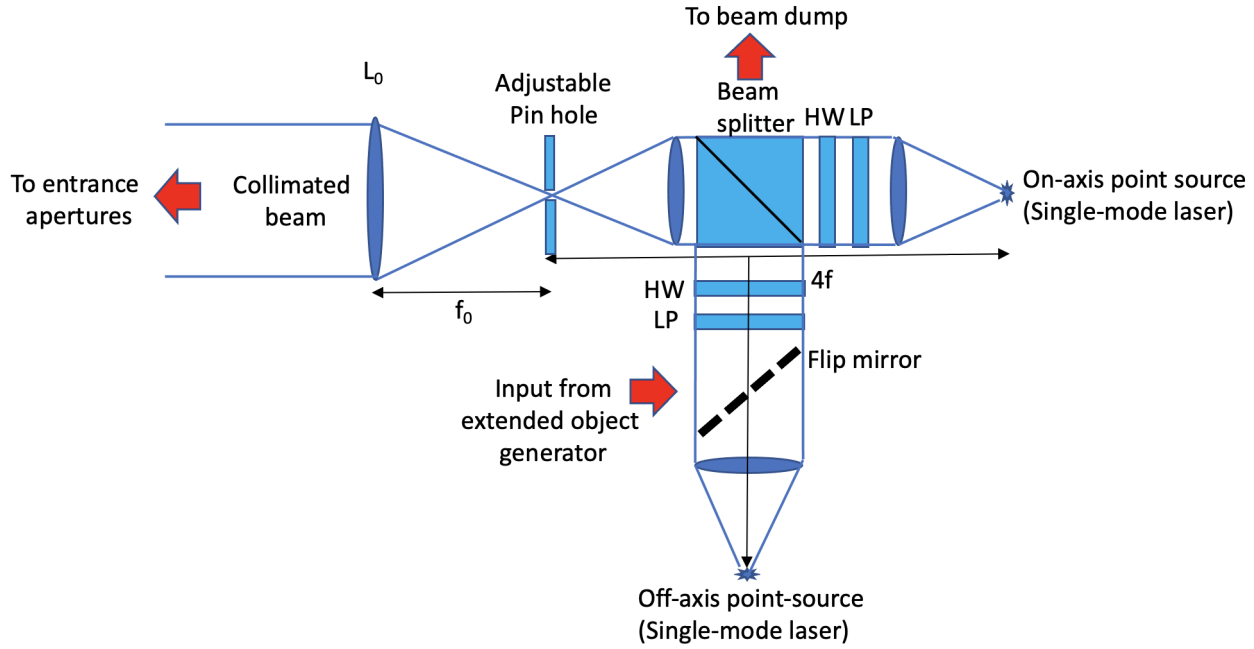


Figure 4.1 Laser module that feeds ARES, composed of two lasers, one of which is on a translation stage to change the separation between sources.

The optical schematic for ARES can be seen in Fig. 4.2, where the optical schematic for each leg is identical. First, the 10 mm beam encounters a set of relay optics (L1–L2) that fold the beam (M1) and relay the face of the aluminum aperture to SLM1. This SLM will act as the high-altitude layer of the atmosphere. An optical trombone (M2–M5) is placed directly after SLM1 to add simulated height to the high-altitude phase screen. From there, a half wave plate (HWP1) is placed to rotate the polarization vector to match the preferred polarization of SLM2. When the optical trombone is set such that there is no distance between SLM1 and SLM2 (i.e. SLM1 is in the ground layer), SLM1 is relayed to SLM2, in the ground layer, by a set of relay optics (L3–L4) and a fold mirror (M6). The beam is then expanded (L5–L6) and folded (M7) a final time to a diameter of 13.3 mm to fill the face of an

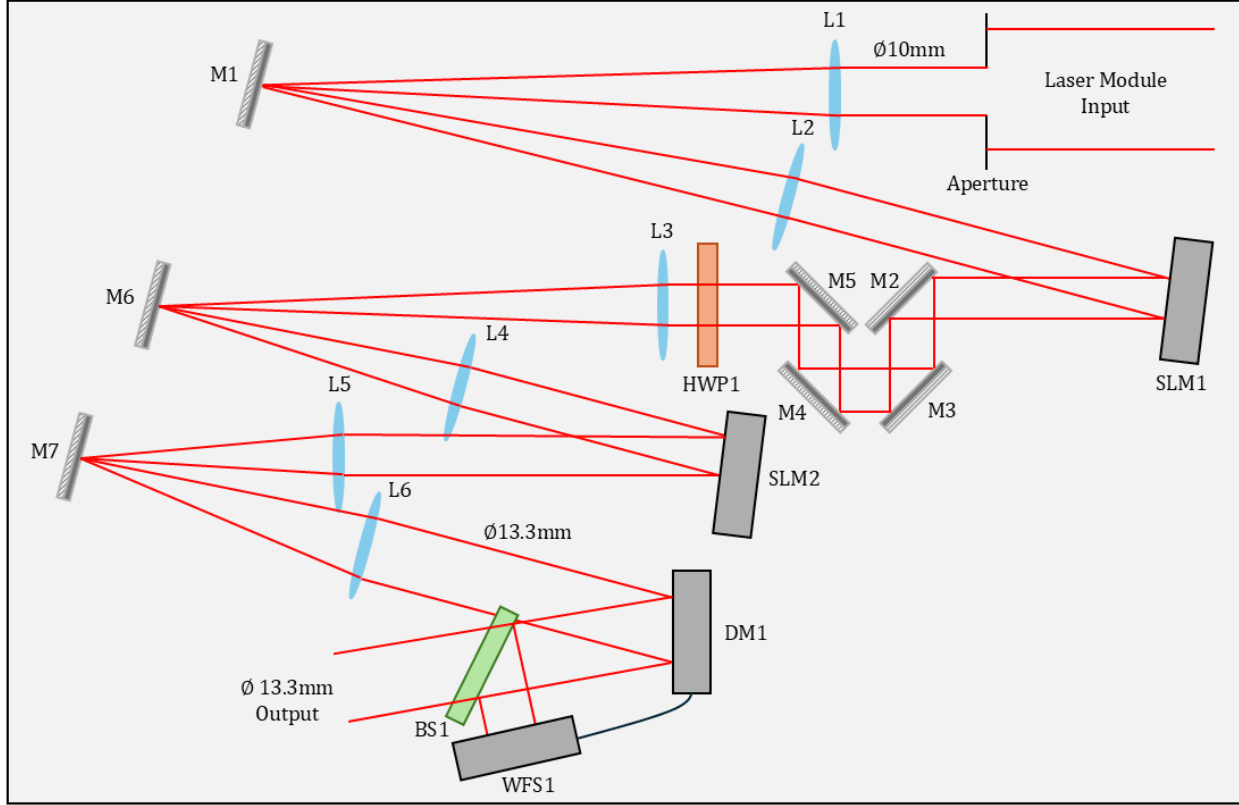


Figure 4.2 Schematic of the ARES turbulence generator. The key components of ARES are SLM1 and SLM2, acting as the high altitude layer and ground layer of turbulence, respectively. The optical trombone, M2–M5, set the height of the upper layer.

Alpao Deformable Mirror (DM)-97 (DM1). The Alpao DM-97 features 11 actuators across the pupil each with a maximum actuator stroke of $60 \mu\text{m}$ for tip/tilt correction or $40 \mu\text{m}$ for astigmatism and defocus correction, and operates at a maximum speed of 700 Hz. A 50:50 beam splitter (BS1) feeds a Shack-hartmann wavefront sensor (WFS1) with 32 lenslets across the pupil, each sampled by 2×2 pixels, that is in a closed loop with DM1. The DM is flattened by sending a plane wave through the system where it is sensed by Wavefront Sensor (WFS)1 and corrected by DM1. We are able to achieve the minimum wavefront distortion quoted by the manufacturer of $7 \mu\text{m}$ RMSE for an incident plane wave. ARES,

as it appear on the bench, is seen in Fig. 4.3.

4.1.2 Phase Wraps

The 13.3 mm output beam is collimated and contains the phase imparted by each atmospheric layer and any amplitude variations due to Fresnel propagation. Additionally, the SLMs are limited to phases between $0 - 2\pi$, meaning that larger values are wrapped to fit in this range. These wraps cause diffractive effects that manifest as amplitude variations along the site of the wrap. The effects of these variations on the Point-Spread Function (PSF) can be quite severe, so we must therefore include them in our modeling. We approximate the locations of the phase wraps by applying the Sobel operator¹ [110] to the wrapped phase screen and then scaling and thresholding the result such that the amplitude map contains values between $0 - 1$. Fig. 4.4 shows the effect on the PSF of these amplitude variations for 8 waves of defocus. The result is a bright spot that outshines the rest of the PSF.

4.1.3 Zero-Order Diffraction Spot (ZODS) Removal and SLM Flattening

SLMs are not perfect devices. As stated in Sec. 1.2, they contain pixels that can be programmed to impart phase changes on a beam. However, there is space between pixels, approximately 3.5% of the area inhabited by the beam, that reflects light without adding phase. This produces a bright spot in the PSF, known as the Zero-Order Diffraction Spot (ZODS). Rather than modeling this spot in post production, we chose to remove it optically. This was done by simply adding defocus to the final phase screen. This does not technically “remove”

¹The Sobel operator calculates the vertical and horizontal gradients of an image and is usually used as an edge-finding operator.

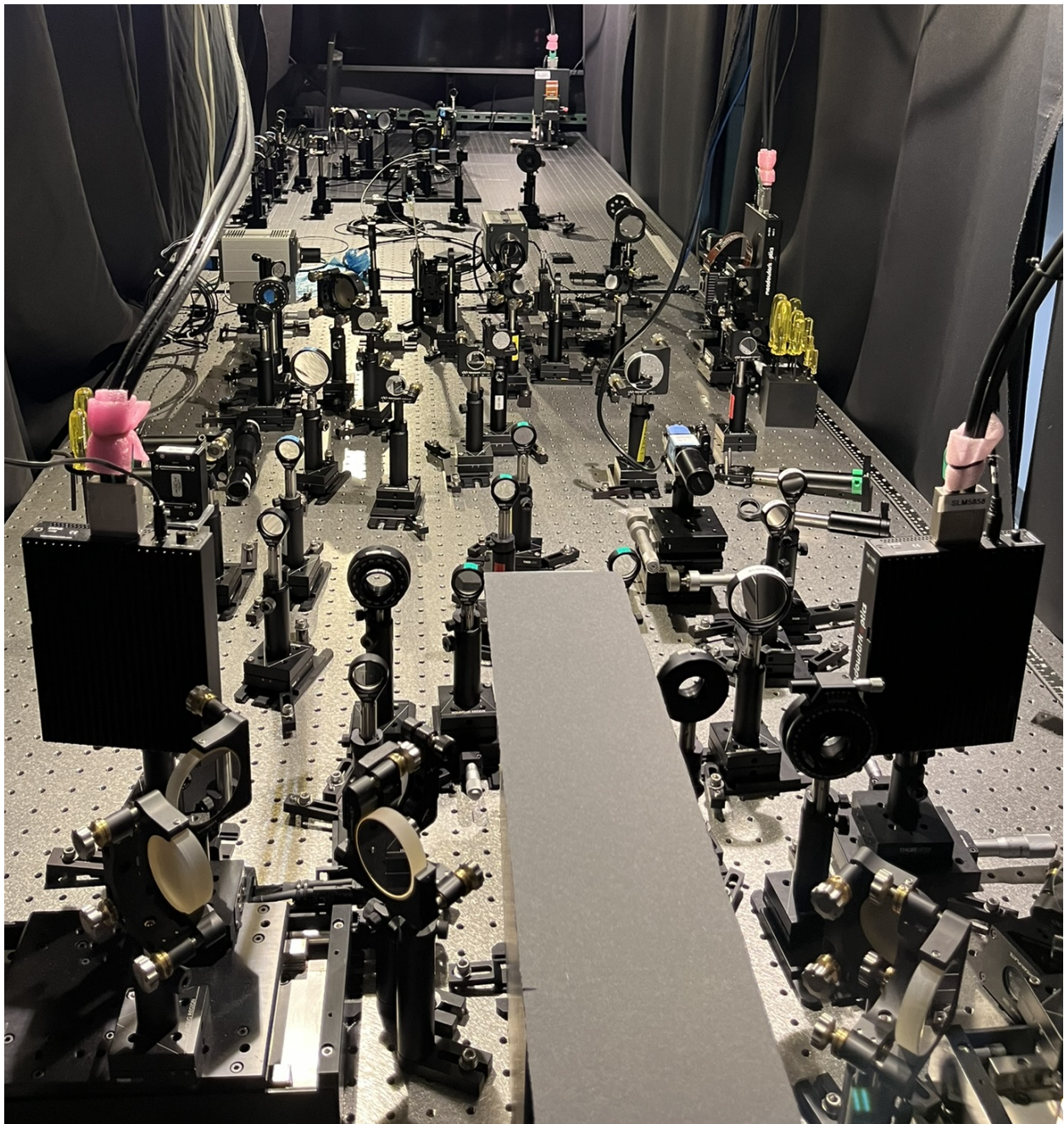


Figure 4.3 ARES on the optical bench.

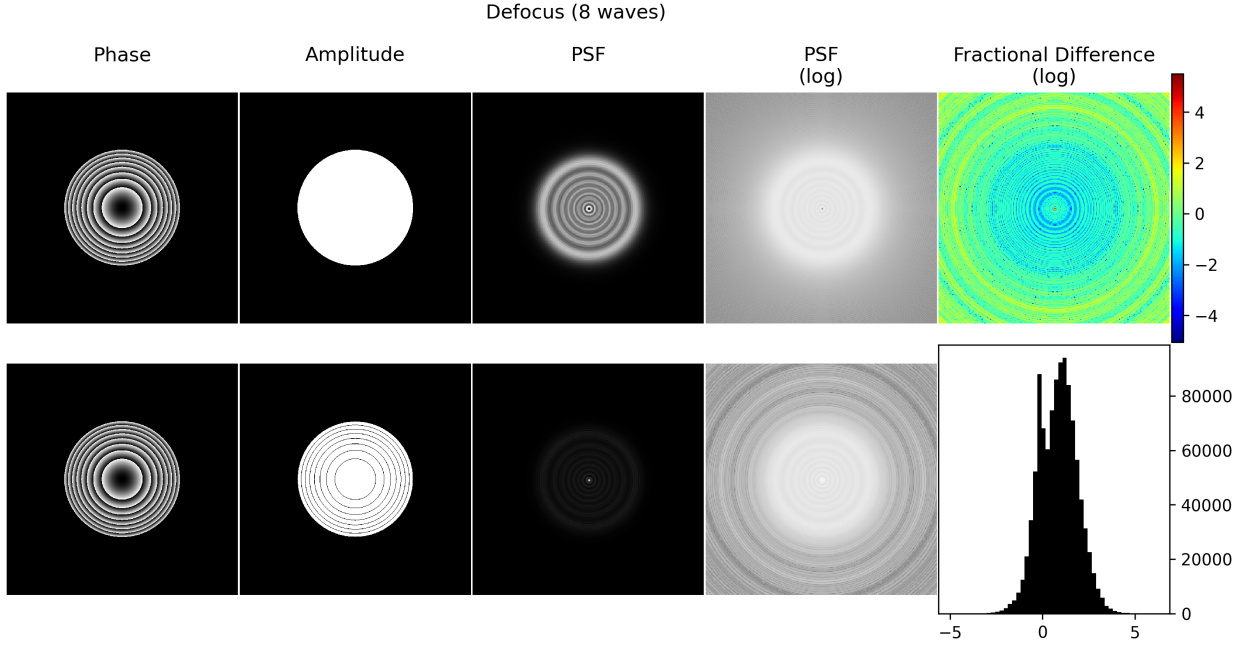


Figure 4.4 Comparison of the expected results without (top row) and with (bottom row) amplitude variations from phase wraps for 8 waves of defocus. The phase screens can be seen in the first column and the amplitudes are seen in the second column. The third column shows the simulated PSF formed by these phases and amplitudes and column four shows the common logarithm of the PSF. Finally, the last column shows the common logarithm of the fractional difference between the two PSFs (top) and a histogram of the logarithmic fractional differences (bottom).

the ZODS completely, but rather pushes it out of focus with respect to the atmospheric PSF.

The effect of this method can be seen in Fig. 4.5. As can be seen, the ZODS is pushed into the far field without losing much fidelity in the generated PSF.

Next, the SLMs have some curvature in their coverglass which adds some unwanted phase variation. The optics in the system are also not perfectly aligned and add some degree of unwanted astigmatism and defocus, mainly. By measuring this added phase (ϕ), we can apply the conjugate ($2\pi - \phi$) to the SLM to cancel out the aberrations. This will enhance the fidelity of generated PSFs with ARES. We will accomplish this task using the technique

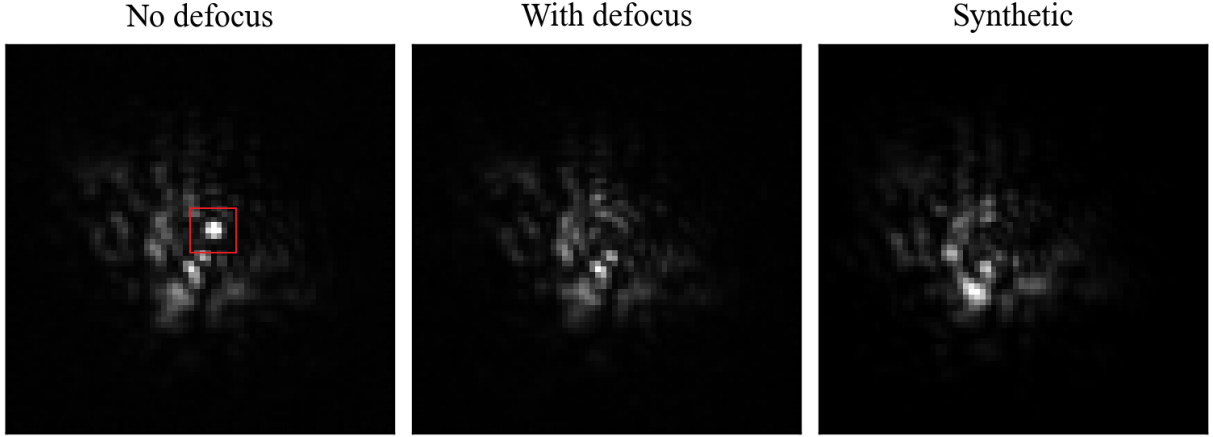


Figure 4.5 Removal of the ZODS with defocus. Left shows the PSF from ARES with the ZODS present (within the red box). The center image shows the result of adding defocus to the phase screens. The right image shows the computer-generated PSF for comparison to evaluate any degradation in fidelity as a result of adding defocus.

of phase diversity [29]. Phase diversity works by adding a known phase, i.e. the diversity phase ϕ_D , and observing the change in the PSF. With enough PSF measurements, we can solve for the static phase ϕ_0 . In practice, we choose to add a number of low-order Zernike polynomials as the diversity phase. Specifically, we add ± 1 wave of defocus, ± 1 wave of oblique astigmatism, ± 1 wave of vertical astigmatism, ± 1 wave of vertical coma, ± 1 wave of horizontal coma, and ± 1 wave of primary spherical aberration². More than one wave of each aberration can be used instead but this increases the density of phase wraps in the phase screen. The use of bi-symmetric pairs was shown by [111] to produce better retrievals than the traditional one-sided (i.e., +1 wave of aberration) phase diversity method. Mathematically, we want to find the optimal static phase ($\tilde{\phi}_0$) that minimizes the discrepancy between our

²In the Noll indexing scheme, where the matrix index of the Zernike polynomial is represented with one number rather than two, these correspond to indices 4, 5, 6, 7, 8, 10, and, 11, respectively.

observed (h) and simulated PSFs (\hat{h}). To do this we minimize the following equation:

$$\epsilon = \sum_{n=1}^{N_{zern}} \|\hat{h}_n - h_n\|_2^2 , \quad (4.1)$$

, where N_{zern} is the number of PSFs collected for the analysis, n is the index for each measured PSF, and $\|\cdot\|_2$ is the ℓ_2 norm. For our case, $N_{zern} = 12$. Since the laser source is a point source, the collected images, scaled to have unit volume, are images of the PSF, or rather $I = \delta \odot h = h$. The simulated PSFs are given by

$$\hat{h}_n = |F^{-1}p_n|^2 , \quad (4.2)$$

where $p_n = A_n \exp(i\theta_n)$, $\theta_n = \tilde{\phi}_0 + \phi_{D,n}$, and $\phi_{D,n}$ is the known diversity phase from aberration n . We use the Variable Metric Limited Memory Bound (VMLMB) minimization engine in OptimPackNextGen.jl³ to solve for $\tilde{\phi}_0$. Analytic gradients for the minimization can be found in Appendix A. The recovered static phase at each SLM can be seen in Fig. 4.6. Fig. 4.7 shows the diffraction-limited PSF before and after flattening. In both cases, we see a noticeable visual improvement in the diffraction-limited PSF after flattening as well as a lower RMSE value between the observed and ideal PSFs.

4.1.4 Performance

Now that the static aberrations in the system are corrected we can evaluate ARE's ability to generate accurate turbulence. For a single layer of turbulence, the simulated and observed PSFs can be seen in Fig. 4.8. Visually, these PSFs show strong agreement with their computer-generated counterparts. A quantitative comparison is seen in Fig. 4.9 where we

³<https://github.com/emmt/OptimPackNextGen.jl>

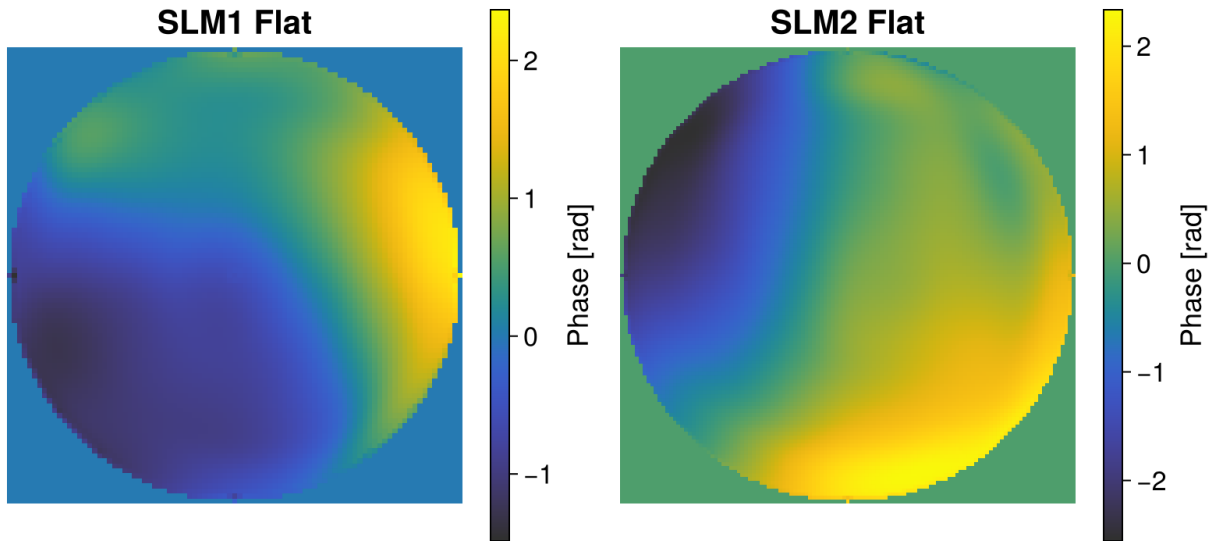


Figure 4.6 The static phase in units of radians recovered at SLM1 and SLM2 using a phase diversity process.

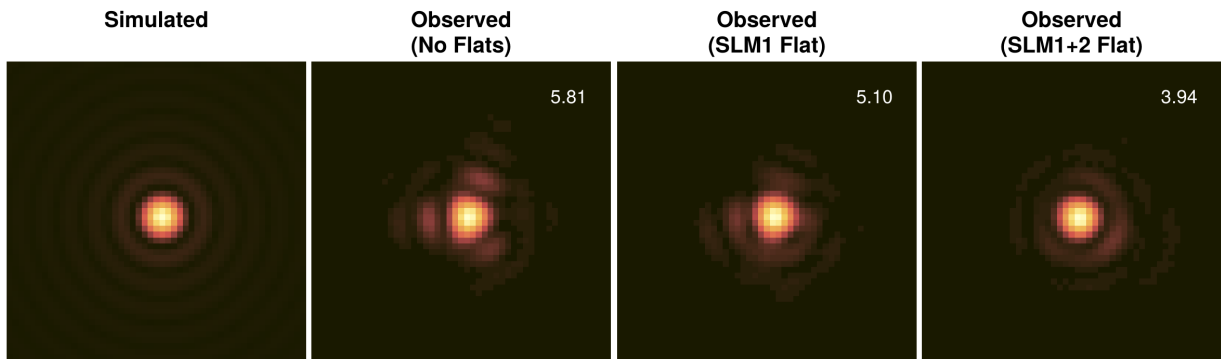


Figure 4.7 Comparison of the observed PSF at each stage of flattening, starting with the simulated diffraction-limited PSF for an ideal system, then moving to the observed PSF before flattening, the PSF after flattening SLM1, and finally after flattening both SLMs 1 and 2. Each image is shown on a square-root scale. The Root Mean Square Error (RMSE) between the simulated PSF and each observed PSF is shown in the upper right corner of each plot, in units of 10^{-4} intensity units.

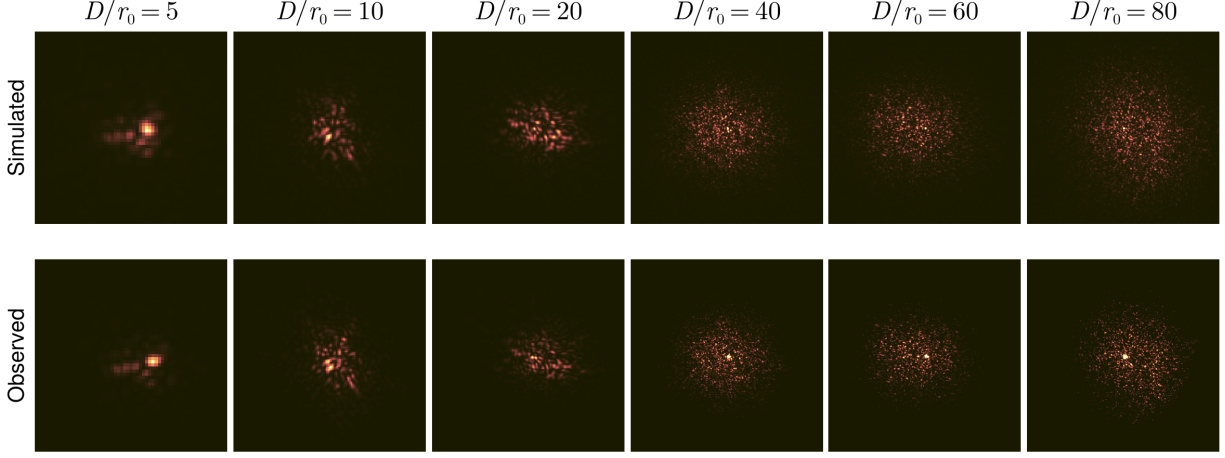


Figure 4.8 Simulated (top row) vs observed (bottom row) PSFs generated with ARES for 1 atmospheric layer. PSFs are generated at D/r_0 values from 5 – 80, going from left to right. Images are thresholded so that the bright spot from phase wraps does not drown out the structure of the atmospheric PSF.

have computed the Structural Similarity Index Measure (SSIM) [112] between the two sets of images. Identical images will yield an SSIM of 1 while images with no structural similarity will yield an SSIM of 0. Here, we are seeing a strong level of agreement all the way up to $D/r_0 = 60$ and a decrease in performance at stronger turbulence values. The decrease in performance is likely a result of the bright spot from phase wrapping dominating the PSF and from the faint background light of the ZODS being brighter, relative to the brightest speckles.

4.2 SLM as an Imaging Shack-Hartmann (ISH)-WFS

Using ARES, we also investigated the use of an SLM as an ISH-WFS. In this experiment, we partition the beam into an array of Fresnel lenses on the SLM where we can dynamically

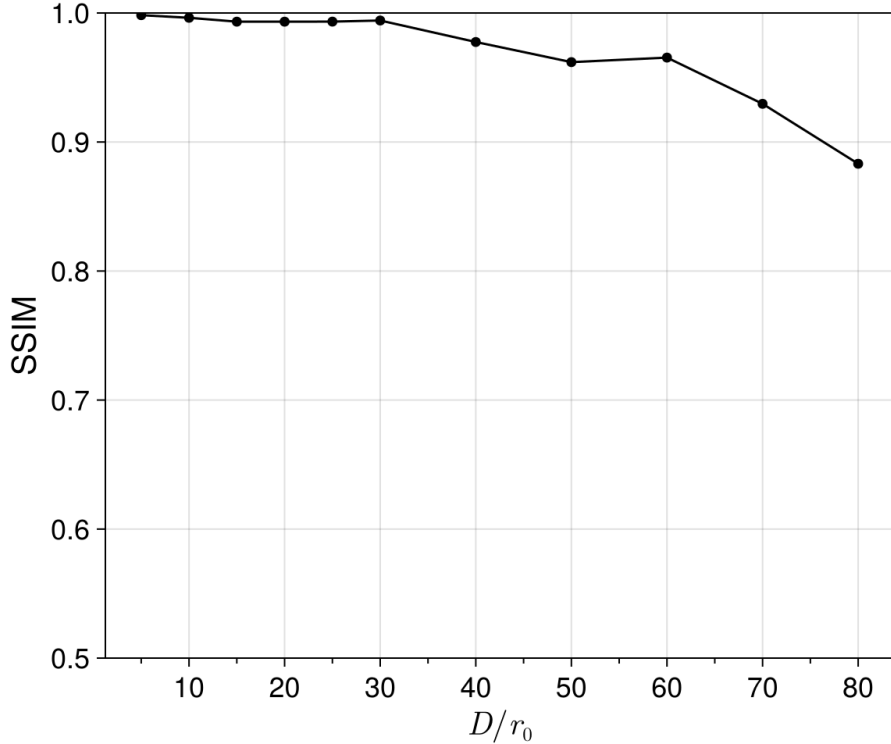


Figure 4.9 SSIM vs D/r_0 for the set of simulated and observed PSFs generated with ARES.

change the focal length, size, and number of lenslets across the pupil. An example phase screen for a 6×6 lenslet array that is put on the SLM can be seen in Fig. 4.10. This idea of an adaptive microlens array was proposed by [113], implemented by [114], and tested on simulated atmospheric wavefronts by [115] in an Adaptive Optics (AO) loop. They did a traditional spot-centroid routine to measure the local slope of the wavefront rather than a detailed modeling of the lenslet images (as in Chapter 2). In addition to collecting the lenslet images we also image the intensity at the pupil plane. This allows us to approximate the amplitude variations in the complex wavefront due to phase wraps. An example of the two sets of images collected is seen in Fig. 4.11. Using an SLM as an ISH WFS, we can test

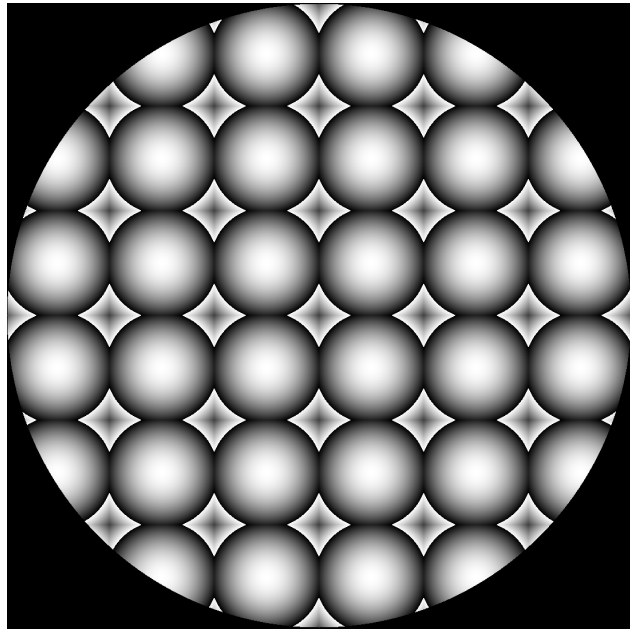


Figure 4.10 6×6 Fresnel lenslet array placed on the SLM to simulate a microlens array.

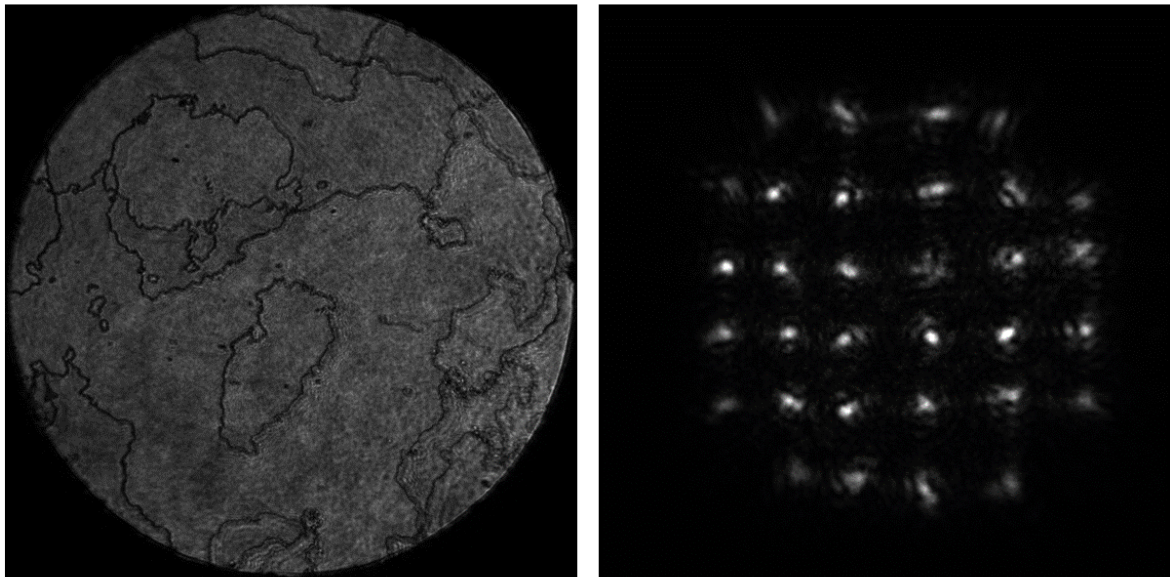


Figure 4.11 (left) Shows an example of a pupil-plane intensity image showing the amplitude variations from phase wrapping in the turbulent phase screens. (right) Shows a set of example lenslet images generated from the turbulent phase screens.

a wide variety of configurations of lenslets and their performance through different levels of turbulence without needing to swap any optics. Furthermore, since ARES is equipped with an AO system, we can also test our methods using *AO-compensated* speckle images.

4.3 ARGOS 2-Channel Broadband Speckle Imager

The ARGOS 2-channel imager is meant to collect the data that were simulated in Chapter 3. As a review, the results in Chapter 3 hinge on the ability to collect full aperture focal plane images and high-fidelity estimates of the wavefront. From Chapter 2, we know that high-fidelity wavefronts can be recovered by post-processing ISH-WFS data. Thus, the ARGOS 2-channel imager is composed of a full-aperture imaging channel and an ISH channel. The specifics of the design are outlined in the following section.

4.3.1 Optical Design

The optical schematic for the ARGOS 2-channel imager is found in Fig. 4.12. First, the beam from the telescope exits the Nasmyth port as a converging beam with focal ratio $f/\# = 6.5$. We place an adjustable field stop at the prime focus of the telescope to limit the Field of View (FOV). Then, the light is collimated by Off Axis Parabola (OAP) 1 and folded by mirror M1. A dichroic beamsplitter with cut-on wavelength 805 nm splits the beam into a “red” channel (transmitted $\lambda > 805$ nm) and “blue” channel (reflected $\lambda < 805$ nm). The blue channel is the full aperture channel and terminates with OAP2 to focus the beam on camera C1 to collect the images. The red channel is the WFS channel and consists of a beam reducer (L1–L2) that shrinks the beam such that it samples the 10×10 lenslets of

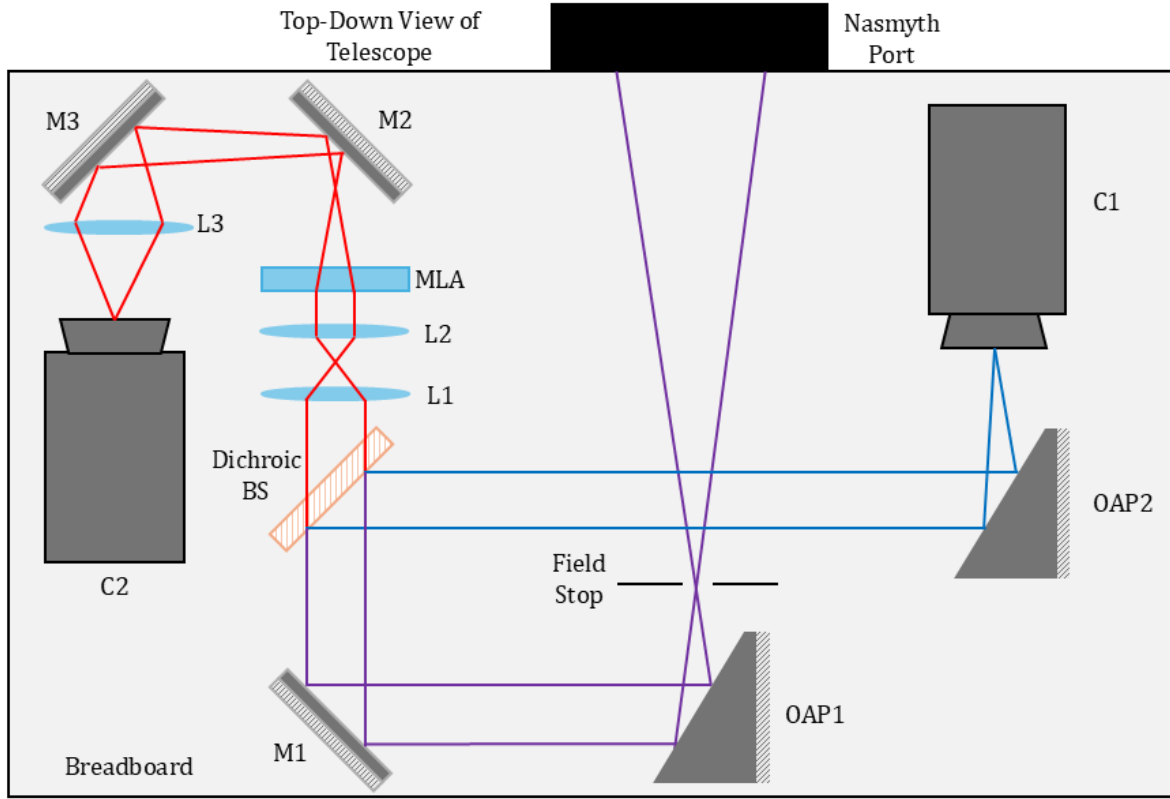


Figure 4.12 ARGOS 2-channel broadband speckle imager optical schematic.

the Micro Lens Array (MLA). Then, the beam is folded by mirrors M2 and M3, and then lens L3 focuses the beam and sets the magnification of the lenslet images where they are finally collected by camera C2. All of the plane mirrors are coated with protected silver to maximize reflectance across the entire visible range. Lenses L1, L2, and L3 are achromats with Thorlabs' AB coating, which has the broadest anti-reflectance properties in the visible range (see Fig. 1.4 for wavelength range). Since the cut-on wavelength of the dichroic is 805 nm and the longest wavelength we can detect is ~ 1000 nm, the effect of focal length shift with wavelength is not expected to be significant over this range, justifying the use of

refractive optics for the red channel. Both cameras are Andor Zyla v5.5 sCMOS cameras and are rigged to a function generator for high-precision triggering. The Andor Zyla v5.5 sCMOS cameras have a 2560×2160 pixel sensor with $6.5 \mu\text{m}$ pixels, $6.5 e^-$ read noise, a maximum frame rate of 201 frames/s (5 ms exposure with overlapping readout) for 512×512 pixel frames, and a maximum Quantum Efficiency (QE) of 0.6 at ~ 600 nm.

The instrument, fully operational, is seen in Fig. 4.13 attached to the side of the Hard Labor Creek Observatory (HLCO) Planewave CDK700 telescope. The optics in the instrument are all placed on kinematic mounts, meaning that components can be swapped easily without the need for realignment. This is handy when users want to observe over different wavelength regimes. We have available a 650 nm cut-on dichroic for increased Signal-to-Noise Ratio (SNR) in the WFS channel but it comes at the cost of the furthest wavelengths from the center being defocused a slight amount. For those wishing to observe across a narrow passband, we have a 50:50 beamsplitter mounted on a kinematic mount outside of the beam path that can be hot swapped for the dichroic with no realignment necessary. Additionally, a set of Chroma 2" Sloan *ugriz* filters are mounted and can be screwed into a 2" lens holder for narrowband operations. Built onto the board is also an alignment laser (right side of Fig. 4.13) with a set of mirrors and a lens carefully selected to match the $f/\#$ of the telescope. This alignment source is not necessarily perfectly aligned but allows the user to align the instrument close enough so that a more-thorough alignment can be done with a bright star.

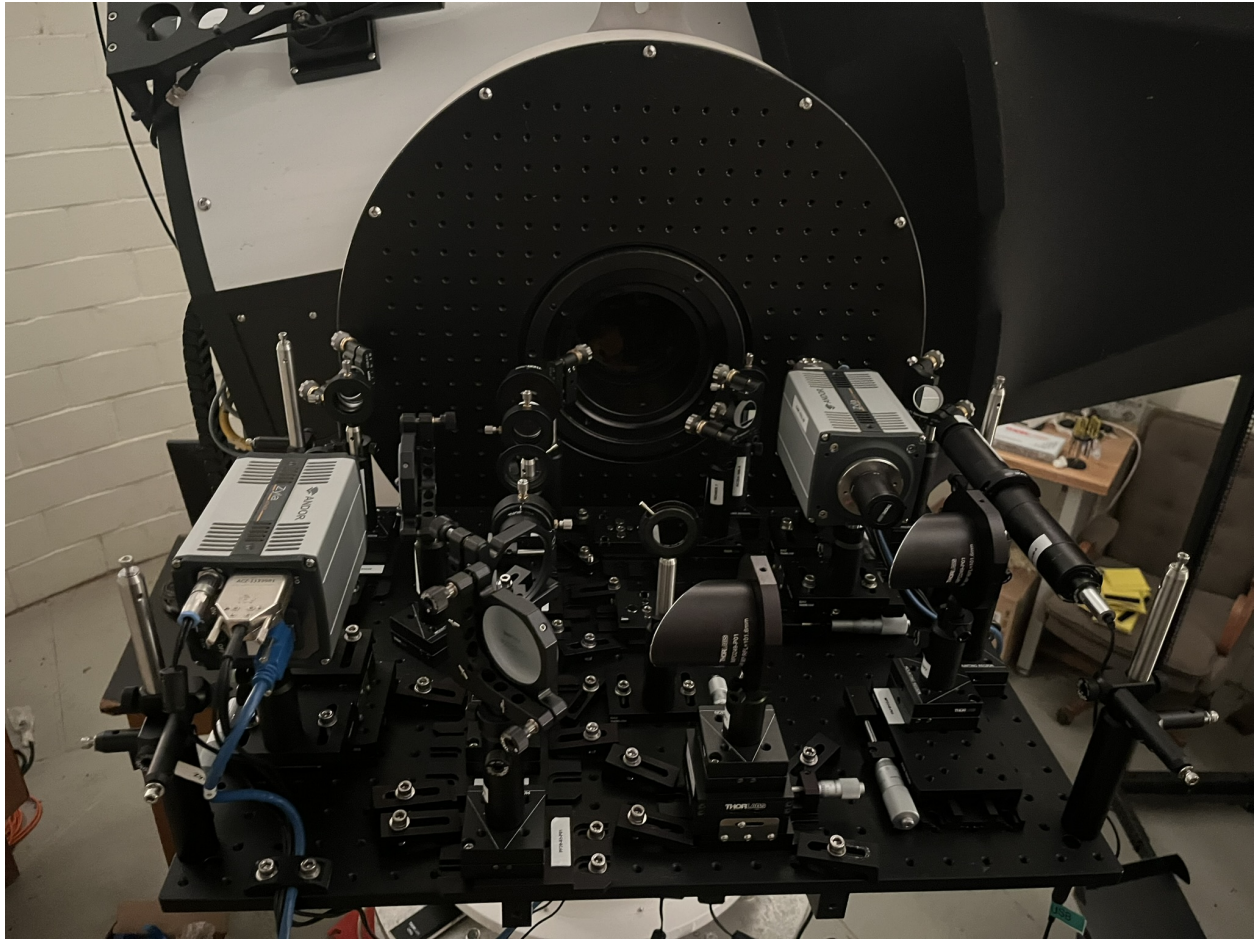


Figure 4.13 ARGOS 2-channel imager attached to the Nasmyth port of the HLCO Planewave CK700 telescope.

4.3.2 Preliminary Results & Current Limitations

The instrument, although mounted on the telescope, has not been used to produce any notable results. However, we took preliminary measurements of Vega on 24 August 2024 and Saturn on 22 September 2024. These data can be seen in Fig. 4.14 and 4.15, respectively. Both datasets were acquired within astronomical twilight and contain 100×5 ms full aperture frames of size 512×512 pixels and a contemporaneous set of WFS images of the same

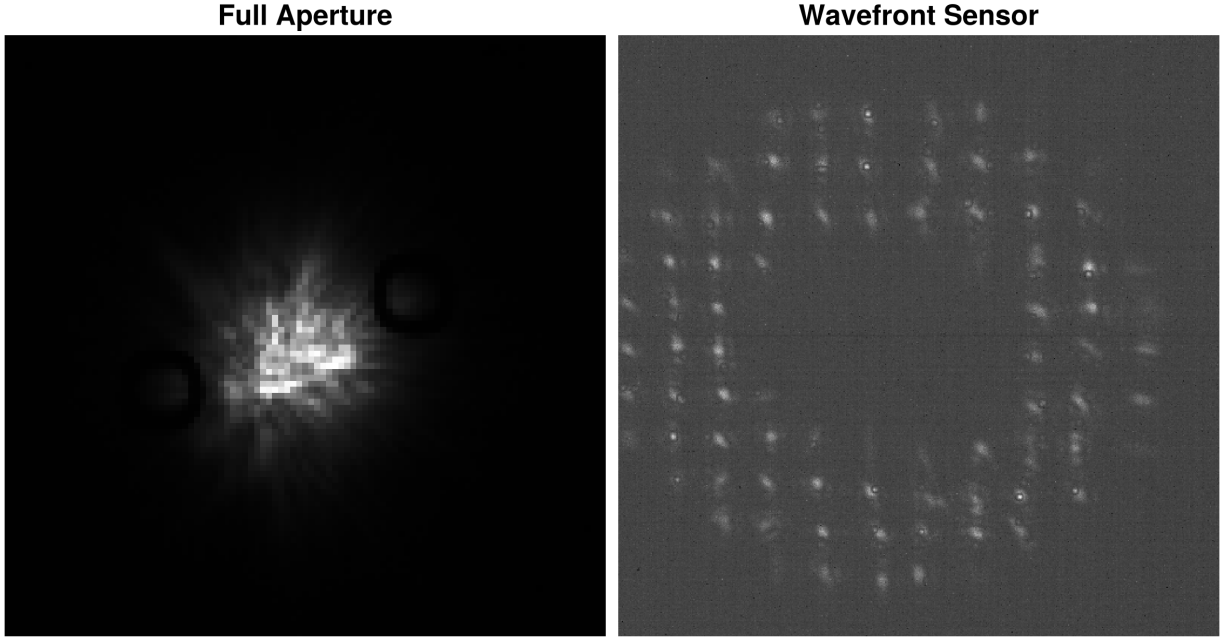


Figure 4.14 Full-aperture data frame (left) and ISH data frame (right) of Vega acquired with the 2-channel broadband speckle imager on 24 August 2024.

exposure time and size. Given the historically-poor atmospheric conditions at HLCO, the coherence time of the atmosphere on a given night is potentially lower than our exposure time of 5 ms. However, to maintain a suitable SNR we chose not to reduce our exposure time. Observations of Vega were taken within 5° of zenith while observations of Saturn were taken at approximately $\eta = 55^\circ$.

Several important things can be learned from these images. Looking at Fig. 4.14, we can see that the WFS channel of the instrument has one additional subaperture image across the pupil than intended (11 observed vs 10 planned). This means that the magnification of the beam onto the MLA provided by the 4f system ($M = 0.2$) is not exact ($M = 0.192$

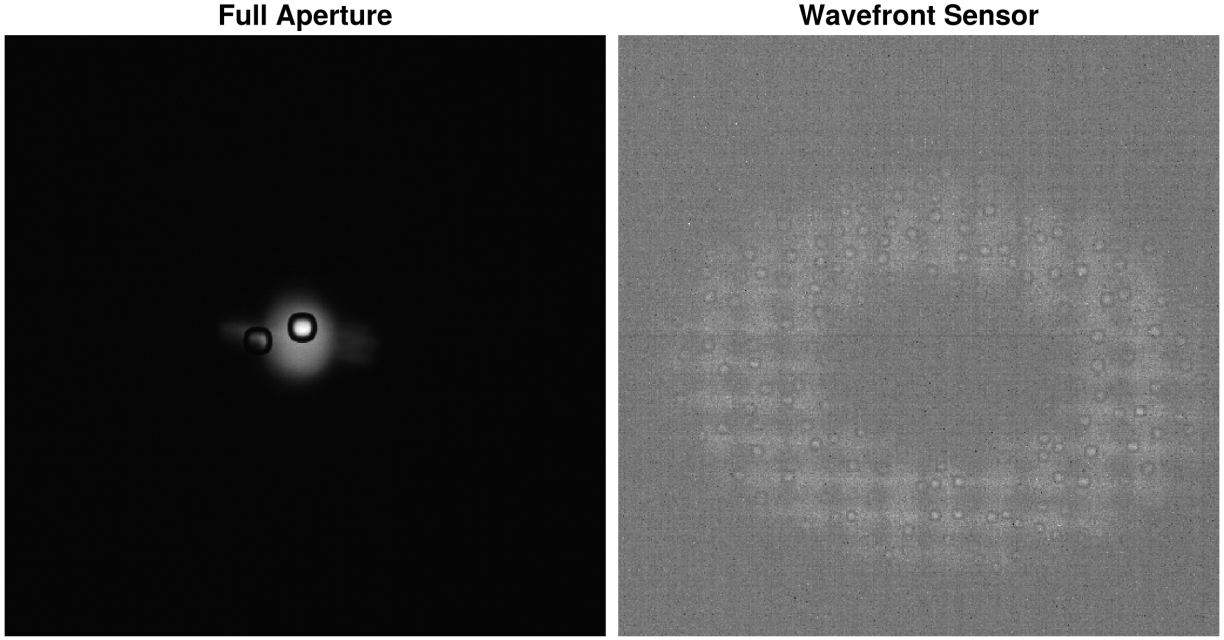


Figure 4.15 Full-aperture data frame (left) and ISH data frame (right) of Saturn acquired with the 2-channel broadband speckle imager on 22 September 2024.

needed for perfect lenslet sampling) and provides a slight over-filling of the MLA. This is not necessarily a problem and is a consequence of using a simple 4f system for magnification control. Exact magnification could be achieved with the addition of several meniscus lenses before and after the lenses of the 4f. This comes at the expense of reduced throughput. As for the magnification of the MLA images, which is set by the final lens of the WFS channel (L3 in Fig. 4.12), we see in Fig. 4.15 that the subaperture images are somewhat overlapping. This can be remedied by changing the magnification of the subaperture images by altering the distance of the final imaging lens in the WFS channel from the MLA. It may be the case that, in order to achieve Nyquist sampling, the subaperture images will overlap. In that

case the MLA would be replaced for one with a larger lenslet pitch (i.e. the spacing between lenslet centers).

We can also see that the subaperture images have a low SNR, which, at first glance, might be surprising for a $\text{mag}_V = 0$ mag target like Vega. This could be due to the spectrum of Vega peaking at ~ 290 nm, where the WFS channel of the instrument is sensitive to light between $805 - 1000$ nm. It would be more advantageous to utilize the 50:50 beamsplitter for this case or a dichroic with a cut-on wavelength closer to the peak wavelength of the target. If using a beamsplitter, the focal length shift with wavelength is something that needs to be considered and accounted for in the modeling of the images.

Next, the FOV of the instrument was not entirely known prior to these on-sky images. Looking at Fig. 4.15, if we consider the globe of Saturn to be $20''$ in diameter, that makes the FOV across the full image $\sim 159''$. Unfortunately, the instrument uses OAPs to collimate and focus the beam from the telescope and these optics are known only be well-behaved across narrow FOVs, much narrower than the entire FOV of our images. We observed significant coma outside of $\sim 20''$ from the image center. This presents a problem for targets that exceed this extent and means that the pointing model of the telescope needs to have sub-arcsecond precision. Over the course of several nights we built a point model consisting of 70 points evenly distributed in azimuth and between altitudes of $45 - 85^\circ$. From this we were able to achieve $\sim 3''$ precision, which is insufficient for operating this instrument effectively. Additionally, for targets in LEO, tracking errors are more pronounced than objects that track at a sidereal rate. Compounded with pointing errors, we see $> 10''$

pointing error when tracking objects in LEO. In all, the next iteration of this instrument would see both OAPs replaced with achromatic doublet lenses, both for ease of alignment and for greatly-reduced aberrations far from the image center, meaning larger FOVs can be imaged accurately. Again, this does increase the complexity of the modeling that would need to be done to reproduce the images.

Unfortunately, there are obtrusive “donuts” in every single frame (most apparent in the full-aperture image in Fig. 4.15) that come from condensation on the camera sensor due to the camera’s desiccant being saturated. For both of the Andor Zyla v5.5 sCMOS cameras, the only way to fix this is by sending them to the company for servicing. This processes is both costly and lengthy, meaning that the instrument is out-of-commission until spring 2025, at the earliest. These donuts render every image unusable for analysis. However, as is seen above, they still provide a useful diagnostic for learning some basic properties of the instrument.

Finally, an overlooked component that would be extremely useful in this setup is an atmospheric dispersion corrector. As is seen in Chapter 3, dispersion-corrected images are easier for our code to reconstruct and reduce the complexity of the modeling slightly. Something that is not considered in Chapter 3 is the slight decrease in signal from the imperfections in the optics of the dispersion corrector. This should not, however, have a detrimental effect on the SNR of the images.

4.4 Table of Variables

Below is a table containing each variable used in this chapter and a short description of that variable.

$\overline{(\dots)}$	Complex conjugate
$\ \cdot\ _2$	ℓ_2 norm
\odot	Convolution operator
$(\cdot)^T$	Matrix transpose
A_n	Complex wavefront amplitude for observed PSF n
D	Telescope diameter
δ	Delta function
ϵ	Cost function
F^{-1}	Inverse 2D Fourier transform operator
h_n	Observed PSF for Zernike n
\hat{h}_n	Model PSF for Zernike n
i	Imaginary unit
I	generic image
$\text{Im}\{\dots\}$	Imaginary part of input
λ	Wavelength
N_{zern}	Number of Zernikes used in phase diversity
p_n	Pupil function for observed PSF n
$\phi_{D,n}$	Diversity phase for Zernike n
$\tilde{\phi}_0$	Estimated static phase
r_0	Fried parameter
$\text{Re}\{\dots\}$	Real part of input
θ_n	Composite wavefront phase for observed PSF n

CHAPTER 5

Discussion, Conclusion, and Future Work

As with all projects, there is a treasure trove of projects to build upon or improve these results. In this chapter we discuss ways to move forward and implications of this work for the broader community.

5.1 Closely Spaced Objects (CSOs)

The work in Chapter 2 and 3 can be combined to perform *wide-field* hyperspectral speckle imaging. Assuming we see the comparable performance gains across narrow Field of Views (FOVs) as in Chapter 2, we would expect this to boost our ability to detect Closely Spaced Objects (CSOs). Generally speaking, CSOs consist of small, faint bodies placed close to large, bright bodies. In astronomy this is equivalent to a high-contrast binary system, such as a binary stellar system or an exoplanet system. In the Space Domain Awareness (SDA) community, this typically refers to a “snuggler” satellite, or CubeSat, parked next to a large satellite. The intentions of these smugglers can be nefarious, so it is paramount to national security that we be able to sniff out bad actors at all times. As an initial test, we placed an unresolved, purely solar panel CSO 8 pixels ($0.125''$) from the main satellite in Chapter 3 and gave it a contrast of 10^{-2} . With noise-free observations and perfect knowledge of the wavefronts we were able to recover the morphology and the spectrum of the CSO, as seen in Fig. 5.1. Under the presence of noise and degraded wavefronts we expect these results to suffer. However, with enough iterations we still expect to *detect* the CSO, even if the spectrum is not recovered with the exact morphology. Additionally, these data were synthesized

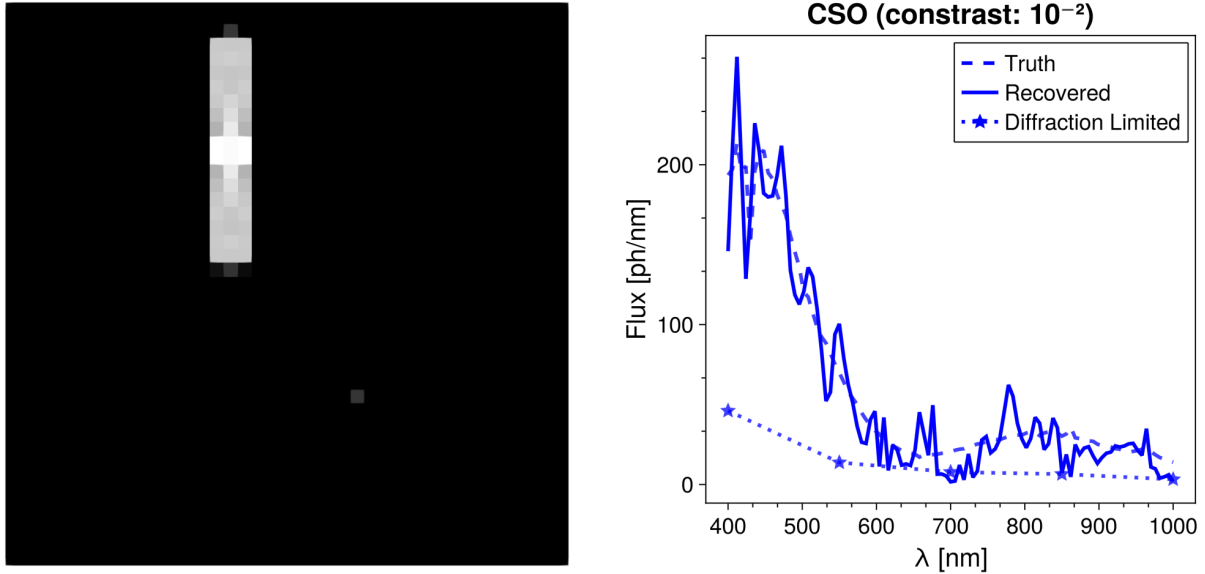


Figure 5.1 (left) The recovered morphology of the main satellite and the CSO to the lower right on a logarithmic scale. (right) The recovered spectrum of the CSO at 101 wavelengths.

with an isoplanatic imaging model. When synthesized with an anisoplanatic imaging model, the recovered spectrum of the CSO would likely show a larger difference than what we see in Fig. 5.1, similar to the results found in Chapter 2. This again highlights the need for a full anisoplanatic solution. Knowing the *true* contrast of the CSO sheds light on its projected area, which has implications to the technological infrastructure onboard and the capability of the spacecraft. As we will see in Section 5.4, the task of anisoplanatic modeling of polychromatic data is extremely computationally expensive and requires considerable effort to provide results in a meaningful time frame. CSOs present a threat to national security and potentially require immediate action. Computations that take months to complete serve as a major weakness in our ability to characterize CSOs.

5.2 Extension to 30 m Class Telescopes

This work has shown that atmospheric turbulence provides diversity in speckle images that can be leveraged to glean information on the underlying target that we may have otherwise missed out on, such as high spatial frequency information (see Chapter 2) or spectral information (see Chapter 3). [89] showed that the 2-channel imaging scheme works for strong turbulence, up to at least $D/r_0 = 80$, seen by a $D = 3.6\text{ m}$ telescope, and [102, 103] showed that an annular partitioning scheme can provide further performance gains through particularly strong turbulence by probing different regions of the turbulence and target power spectrum individually. However, the strengths of turbulence that will be seen by the upcoming 30 m class of telescopes is unprecedented. For example, for good seeing on Haleakala of $r_0 = 18\text{ cm}$ at 500 nm a 3.6 m telescope sees $D/r_0 = 20$, considered moderate turbulence, while a 30 m telescope sees turbulence of strength $D/r_0 = 167$, considered extreme turbulence. To correct for this level of turbulence will require extreme Adaptive Optics (AO) systems with large numbers of actuators and large actuator stroke. However, residual wavefront error from residual turbulence errors can be corrected using a variation of the deconvolution process in Chapter 2. Additionally, our method of Multi-Frame Blind Deconvolution (MFBD) may be capable of directly unscrambling images through this extreme level of turbulence without AO compensation.

5.3 Hybrid Optical Telescope Concept

Given the task of high resolution imaging of satellites from Low Earth Orbit (LEO) out to Cislunar space, we have also been experimenting with the Hybrid Optical Telescope (HOT) architecture. In the HOT concept, a set of ring-distributed, smaller-aperture telescopes are deployed within a tensegrity structure to gain both improved angular resolution and mechanical stability. This, of course, comes at the expense of reduced light gathering power, compared to a similar-diameter segmented telescope. However, HOTs are much more cost-effective than traditional monolithic and segmented telescopes, coming in at approximately 1/10th of the cost for an equivalent-sized segmented telescope and 1/5th the cost of an equivalent-sized interferometric array. Additionally, the HOT does not require the complex optics of an interferometer, such as delay lines and beam combiners, since the segments of the telescope are slewed as one entire structure. For the task of high-resolution imaging, the HOT presents a unique opportunity to perform Point-Spread Function (PSF) engineering. Since each segment is controlled by its own set of motors and drives they can each be manipulated to produce features in the PSF such as a dark hole that can be used to scan for faint companions. Using the equipment in the Remote Sensing for Space Sciences (RSSS) lab at Georgia State University (GSU), [116] was able to generate a dark hole using a small-scale aluminum aperture to simulate a ring of HOT apertures and an Spatial Light Modulator (SLM) to impart phase perturbations (see Fig. 5.2). These results are without corruption by the atmosphere, meaning that further gains could be realized with a wavefront sensor and post-processing scheme. Wavefront sensing on this configuration of mirrors is not

40 Zernikes

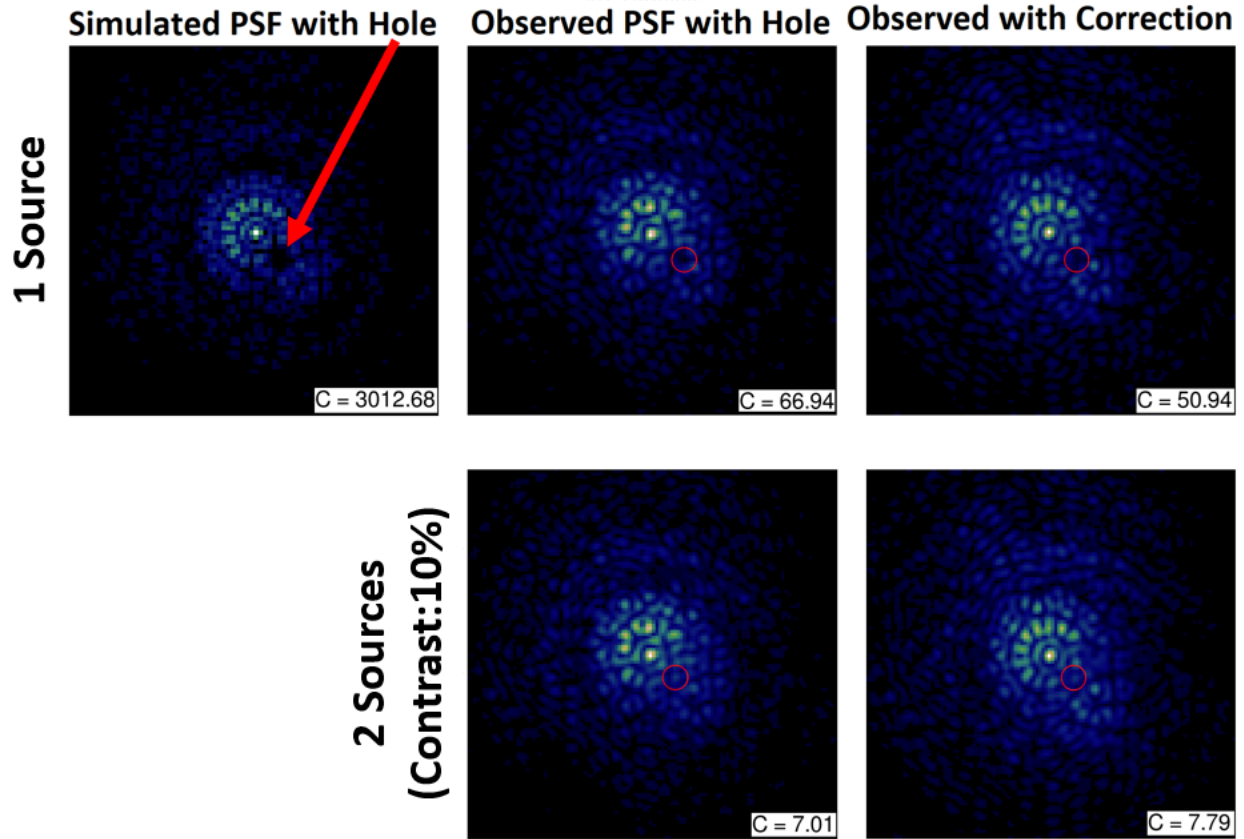


Figure 5.2 Dark hole generated with a HOT aperture and SLM. The first column shows the computer generated diffraction-limited PSF with a dark hole indicated by the red arrow. This PSF is generated by performing a Zernike decomposition of the PSF with the hole and selecting the first 40 Zernike modes to reconstruct the phase. The middle column shows the observed PSF on the optical bench using this reconstructed phase. The final column shows the same PSF but with correction for static phase on the SLM, using the procedure given in Sec. 4.1.3. The first row shows the case of a single point source and the second row shows the case of a fainter secondary source within the dark hole. Finally, the numbers in the lower right corner of each plot are the contrast between the flux in the central spike of the PSF and the flux within the dark hole.

exactly intuitive and work is currently being done to find the most-optimal way to implement a wavefront sensor on an HOT.

5.4 Improvements to MFBD.jl

The work presented here uses the open-source MFBD.jl code¹. This code has many avenues for improvement and extension. First, the analysis code needs to be rewritten to include several factors. We are in the process of including the reflectivity of each lens and mirror in our modeling, however, this has not been tested fully. Next, our 2-channel broadband speckle imager is not a perfect instrument, meaning that the static phase of the system would need to be solved for in the code. Also, any background flux (significant for daytime observations and low Signal-to-Noise Ratio (SNR) environments) needs to be accounted for in the code as well. In terms of the minimization engine, we are simply finding the set of parameters (θ) that minimize the ℓ_2 distance between the observed (d) and modeled (g) data frames, $r(\theta) = d - g(\theta)$, or

$$\operatorname{argmin}_{\theta} \|r(\theta)\|_2^2 ,$$

i.e., maximum likelihood estimation, which sometimes shows “ringing” in the recovered object due to correlated noise in the residuals. Instead, [117] proposed minimizing a selected portion of the *autocorrelation* of the residuals

$$\operatorname{argmin}_{\theta} \sum_{x,y} M_{ACF}[r(\theta) \otimes r(\theta)]^2 ,$$

¹<https://github.com/djohn134/MFBD.jl>

i.e. maximum residual likelihood, where M_{ACF} is a mask that selects the lag terms to minimize, that are typically set by the size of the PSF. This avoids correlated noise in the residuals and does not produce ringing artifacts in the recovered object. Since autocorrelations can be expressed in terms of fast Fourier transforms, we do not expect the increased computational cost of implementing this method in our code to be significant. Thus, to improve the fitting of noise in our data we will implement a maximum residual likelihood scheme in the future.

Since the same code was used for the work in Chapters 2 and 3, a full tomographic solution for the atmosphere could theoretically be obtained from broadband wavefront sensor data. In fact, this approach would need to be taken to analyze data from the 2-channel imaging instrument. The code is currently capable of synthesizing and analyzing broadband wavefront sensor data over wide FOVs, however, this takes an enormous amount of computer RAM and computation time. For example, to create 100 frames for 32 subapertures of size 64×64 pixels at 100 wavelengths with 81 Efficient Filter Flow (EFF) patches we need ~ 396 GB of RAM. A complimentary set of 256×256 pixel full aperture frames adds another ~ 396 GB of RAM, meaning we need in excess of 800 GB to create the data set, not including the buffer arrays used in the process. A memory-conscious approach can be taken in the data synthesis step, but this requires a full rewrite of the code. More importantly, the computation time for the monochromatic, isoplanatic solution in Chapter 2 using 8 CPU threads takes around 30 minutes, which extrapolates to 50 hours at 100 wavelengths. The height solve step takes around 6 hours, which extrapolates to 600 hours, or a little under

a month of computation time. The final anisoplanatic solve step takes another 6 hours, so another month of computation time. In total, a full tomographic solution would require about two months of computation time, assuming that broadband data require the same number of iterations to converge to a solution as monochromatic data, which is unlikely to be the case. The only viable ways forward are to refactor entirely the code to a distributed framework such as ADMM [73] or migrate the code to a supercomputer such as GSU’s ARCTIC cluster, which provides 75 million CPU hours each year to researchers. *GPU* computing, rather than purely CPU multithreading, could also be useful for speeding up smaller calculations but the problem is then limited to the amount of VRAM on the GPU and the transfer speed to move the data from the CPU to the GPU. It also requires a considerable effort to write efficient GPU kernels that fully exploit the architecture of the available equipment.

5.5 On-Sky Speckle Imaging Validation

There are a wealth of instrumentation projects to pursue based upon of this work. First and foremost, the results of Chapters 2 and 3 should be validated with on-sky measurements. This could be done with our 2-channel imaging instrument after the changes in Section 4.3.2 are made. The results of Chapter 2 could be validated using the Sloan *ugriz* filter set that is present at Hard Labor Creek Observatory (HLCO) to obtain monochromatic speckle images. Ideally, we would observe bright binary stars at a range of separations. ζ Aqr is a well-studied binary system with a combined brightness of $\text{mag}_V = +3.44$ and separation $\sim 2.2''$, used in the past by [118] to study the effectiveness of their speckle-imaging based

technique. Conveniently, it also serves as a close comparison to the hypothetical 3" binary simulated in Chapter 2 and serves as a prime candidate for validation with our technique.

Next, the results in Chapter 3 would ideally be validated by both a calibration source with a known spectrum, such as a star, and a satellite in LEO. A range of calibration sources should be observed spanning different spectral types to study the effect of SNR on the different legs of the imaging instrument. A star like Vega, an A-type main sequence star, has a well-known spectrum that peaks around 290 nm while a star like Betelgeuse, a red supergiant, has a spectrum that peaks around 763 nm. Since the instrument is built on kinematic bases, the dichroic and beamsplitter can be easily swapped to produce optimal SNR in each imaging leg. Additionally, each type of target presents their own level of complexity with the cooler stars showing many more spectral lines and absorption bands and the satellites showing a solar spectrum modulated by each materials' reflectance spectrum. With the 2-channel imaging instrument we expect to recover the blackbody shape of the spectrum and other large-scale features. As for satellites, Starlink satellites are perfect for this work because they are abundant in the night sky and have simple construction, being composed mostly of solar panel. We expect then to recover spectra that closely resemble the solar panel material on board the spacecraft.

5.6 Polychromatic Turbulence Generation

Ideally, the aforementioned broadband imaging instrument would be tested on lab-generated turbulence before being tested on-sky. The Advanced Reconnaissance of Earth-orbiting

Satellites (ARES) turbulence simulator is only currently capable of producing *monochromatic* turbulence, meaning that a new turbulence generator should be built to produce *polychromatic* turbulence. This can be achieved using a combination of Deformable Mirrors (DMs). Here, each layer would be simulated using two DMs in a Woofer-Tweeter configuration [119]. This configuration comes about from the limitations of modern DMs where large actuator strokes come at the cost of less actuators and large numbers of actuators come at the cost of reduced actuator stroke. In the woofer-tweeter system a DM with high dynamic range and lower number of actuators is used to produce low spatial frequency deformations in the wavefront and a second DM with a larger number of actuators is used to impart high frequency information on the wavefront. Since DMs impart Optical Path Difference (OPD) directly on the wavefront, rather than altering the phase at a particular wavelength like SLMs, they are capable of simulating polychromatic turbulence. Polychromatic turbulence simulation also requires polychromatic sources. In the lab, we are currently in possession of broadband diodes that produce blackbody spectra for a range of temperatures. This is useful for simulating binary systems in the lab with variable contrasts, separations, and now spectral types.

APPENDIX A

Analytic Gradients

Much of the recovery processes in this work rely on knowledge of the gradient of the minimization criterion function. Below, we list the analytic gradients for each step of our recovery process. Please refer to the appropriate chapter for a table of variables.

Object Update

First, we will derive the gradients of the cost function under the assumption of purely Gaussian noise, i.e., $\omega_{tn} = s_{tn}^{-1} \sigma_{RN}^{-2}$. In the monochromatic case (e.g., Chapter 2), the gradient of the cost function (Equation 2.7) with respect to the recovered object \tilde{f} is

$$\frac{\partial \epsilon}{\partial \tilde{f}} = \sum_{t=1}^{N_{epochs}} \sum_{n=1}^{N_{frames}} \frac{\partial \hat{I}_{tn}}{\partial \tilde{f}} \frac{\partial \epsilon}{\partial \hat{I}_{tn}} ,$$

We employed the chain rule to decompose the gradient into independent terms. Below we show the expression for each term.

$$\begin{aligned} \frac{\partial \hat{I}_{tn}}{\partial \tilde{f}} &= \sum_{m=1}^{N_{patches}} H_{tnm}^T \rho_m S_{\downarrow}^T , \\ \frac{\partial \epsilon}{\partial \hat{I}_{tn}} &= 2\omega_{tn}(\hat{I}_{tn} - I_{tn}) , \end{aligned}$$

Finally,

$$\frac{\partial \epsilon}{\partial \tilde{f}} = \sum_{t=1}^{N_{epochs}} \sum_{n=1}^{N_{frames}} \sum_{m=1}^{N_{patches}} 2H_{tnm}^T \rho_m S_{\downarrow}^T \omega_{tn} (\hat{I}_{tn} - I_{tn}) . \quad (\text{A.1})$$

In the broadband case (Chapter 3), the gradient is very similar to Eqn. A.1 with the

addition of some wavelength-dependent terms.

$$\frac{\partial \epsilon}{\partial \tilde{f}_w} = \sum_{t=1}^{N_{epochs}} \sum_{n=1}^{N_{frames}} \sum_{m=1}^{N_{patches}} 2\Delta\lambda H_{tnmw}^T \rho_m S_{\downarrow}^T \omega_{tn} (\hat{I}_{tn} - I_{tn}) . \quad (\text{A.2})$$

This gradient covers both the case of anisoplanatic recoveries and broadband objects.

Next, we will consider the case of mixed Gaussian and Poisson noise, or $\omega_{tn} = s_{tn}^{-1} [\hat{I}_{tn} + \omega_{RN}^2]^{-1}$.

In this case, $\frac{\partial \epsilon}{\partial \hat{I}_{tn}}$ is changed to,

$$\frac{\partial \epsilon}{\partial \hat{I}_{tn}} = 2\omega_{tn}(\hat{I}_{tn} - I_{tn}) - s_{tn} [\omega_{tn}(\hat{I}_{tn} - I_{tn})]^2 ,$$

so that Equation A.2 becomes

$$\frac{\partial \epsilon}{\partial \tilde{f}_w} = \sum_{t=1}^{N_{epochs}} \sum_{n=1}^{N_{frames}} \sum_{m=1}^{N_{patches}} \Delta\lambda H_{tnmw}^T \rho_m S_{\downarrow}^T \left\{ 2\omega_{tn}(\hat{I}_{tn} - I_{tn}) - s_{tn} [\omega_{tn}(\hat{I}_{tn} - I_{tn})]^2 \right\} . \quad (\text{A.3})$$

Wavefront Update

First, we will derive the expression for the analytic gradient of ϵ with respect to the recovered phase sausages $\tilde{\Phi}_{lw}$ in the broadband case, since the monochromatic case can be derived from this.

$$\frac{\partial \epsilon}{\partial \tilde{\Phi}_{lw}} = \frac{\partial \phi_{tnw}}{\partial \tilde{\Phi}_{lw}} \frac{\partial h_{tnw}}{\partial \phi_{tnw}} \frac{\partial \hat{I}_{tn}}{\partial h_{tnw}} \frac{\partial \epsilon}{\partial \hat{I}_{tn}}$$

Again, we've used the chain rule to decompose the gradient into separate terms, all of which are derived below.

$$\begin{aligned}\frac{\partial \phi_{tnw}}{\partial \tilde{\Phi}_{lw}} &= E_{tlw}^T N_G^T M_n^T \\ \frac{\partial h_{tnw}}{\partial \phi_{tnw}} &= -2 \operatorname{Im} \left\{ p_{tnw} F^{-1} \overline{(F^{-1} p_{tnw})} D_w^T \right\} \\ \frac{\partial \hat{I}_{tn}}{\partial h_{tnw}} &= \Delta \lambda X_w^T S_\downarrow^T \\ \frac{\partial \epsilon}{\partial \hat{I}_{tn}} &= 2 \omega_{tn} (\hat{I}_{tn} - I_{tn})\end{aligned}$$

Then,

$$\begin{aligned}\frac{\partial \epsilon}{\partial \tilde{\Phi}_{lw}} &= \sum_{t=1}^{N_{epochs}} \sum_{n=1}^{N_{subaps}} \sum_{m=1}^{N_{patches}} -4 \Delta \lambda E_{tlmw}^T N_G^T M_n^T \\ &\quad \times \operatorname{Im} \left\{ p_{tnmw} F^{-1} \overline{(F^{-1} p_{tnmw})} D_w^T X_m w^T S_\downarrow^T \omega_{tn} (\hat{I}_{tn} - I_{tn}) \right\}.\end{aligned}$$

The extension from phase to OPD \tilde{W}_l is simply

$$\frac{\partial \epsilon}{\partial \tilde{W}_l} = \frac{\partial \tilde{\Phi}_{lw}}{\partial \tilde{W}_l} \frac{\partial \epsilon}{\partial \tilde{\Phi}_{lw}},$$

where the additional term is

$$\frac{\partial \tilde{\Phi}_{lw}}{\partial \tilde{W}_l} = \frac{2\pi}{\lambda_w}$$

Finally,

$$\begin{aligned} \frac{\partial \epsilon}{\partial \tilde{W}_l} = & \sum_{t=1}^{N_{epochs}} \sum_{n=1}^{N_{subaps}} \sum_{m=1}^{N_{patches}} \sum_{w=1}^{N_\lambda} - 8\pi\alpha \frac{\Delta\lambda}{\lambda_w} E_{tlmw}^T N_G^T M_n^T \\ & \times \text{Im} \left\{ p_{tnmw} F^{-1} \overline{(F^{-1} p_{tnmw})} D_w^T X_{mw}^T S_\downarrow^T \omega_{tn} (\hat{I}_{tn} - I_{tn}) \right\}. \end{aligned} \quad (\text{A.4})$$

This gradient can be simplified in many ways, such as in the isoplanatic case ($N_{patches} = 1$) or the monochromatic case ($N_\lambda = 1, \Delta\lambda = 1$). Under mixed Gaussian and Poisson noise, $\frac{\partial \epsilon}{\partial \tilde{W}_l}$ becomes

$$\begin{aligned} \frac{\partial \epsilon}{\partial \tilde{W}_l} = & \sum_{t=1}^{N_{epochs}} \sum_{n=1}^{N_{subaps}} \sum_{m=1}^{N_{patches}} \sum_{w=1}^{N_\lambda} -4\pi\alpha \frac{\Delta\lambda}{\lambda_w} E_{tlmw}^T N_G^T M_n^T \\ & \times \text{Im} \left\{ p_{tnmw} F^{-1} \overline{(F^{-1} p_{tnmw})} D_w^T X_{mw}^T S_\downarrow^T \left[2\omega_{tn} (\hat{I}_{tn} - I_{tn}) - s_{tn} [\omega_{tn} (\hat{I}_{tn} - I_{tn})]^2 \right] \right\}. \end{aligned} \quad (\text{A.5})$$

Phase Diversity

To solve for the static phase $\tilde{\phi}_0$ we must know the gradient of the cost function (Equation 4.1) with respect to $\tilde{\phi}_0$. This is given by

$$\frac{\partial \epsilon}{\partial \tilde{\phi}_0} = \sum_n^{N_{zern}} \frac{\partial \hat{h}_n}{\partial \tilde{\phi}_0} \frac{\partial \epsilon}{\partial \hat{h}_n},$$

and each term is given by

$$\begin{aligned}\frac{\partial \hat{h}_n}{\partial \tilde{\phi}_0} &= 2 \operatorname{Re} \left\{ \frac{\partial p_n}{\partial \tilde{\phi}_0} \cdot F^{-1}(\overline{F^{-1}p_n}) \right\}, \\ \frac{\partial p_n}{\partial \tilde{\phi}_0} &= i \cdot p_n, \\ \frac{\partial \epsilon}{\partial \hat{h}_n} &= 2(\hat{h}_n - h_n).\end{aligned}$$

The final gradient is then given by

$$\frac{\partial \epsilon}{\partial \tilde{\phi}_0} = \sum_{n=1}^{N_{zern}} -4 \operatorname{Im} \left\{ p_n \cdot F^{-1}(\overline{F^{-1}p_n})(\hat{h}_n - h_n) \right\}. \quad (\text{A.6})$$

REFERENCES

- [1] Andy Lawrence, Meredith L. Rawls, Moriba Jah, Aaron Boley, Federico Di Vrundo, Simon Garrington, Michael Kramer, Samantha Lawler, James Lowenthal, Jonathan McDowell, and Mark McCaughrean. The case for space environmentalism. *Nature Astronomy*, 6:428–435, April 2022. doi: 10.1038/s41550-022-01655-6.
- [2] G. H. Rieke, M. Blaylock, L. Decin, C. Engelbracht, P. Ogle, E. Avrett, J. Carpenter, R. M. Cutri, L. Armus, K. Gordon, R. O. Gray, J. Hinz, K. Su, and Christopher N. A. Willmer. Absolute Physical Calibration in the Infrared. *The Astronomical Journal*, 135(6):2245–2263, June 2008. doi: 10.1088/0004-6256/135/6/2245.
- [3] D. L. Fried. Optical resolution through a randomly inhomogeneous medium for very long and very short exposures. *J. Opt. Soc. Am.*, 56(10):1372–1379, Oct 1966. doi: 10.1364/JOSA.56.001372. URL <https://opg.optica.org/abstract.cfm?URI=josa-56-10-1372>.
- [4] R G Lane, A Glindemann, and J C Dainty. Simulation of a kolmogorov phase screen. *Waves in Random Media*, 2(3):209–224, 1992. doi: 10.1088/0959-7174/2/3/003. URL <https://doi.org/10.1088/0959-7174/2/3/003>.
- [5] Norbert Wiener. Generalized harmonic analysis. *Acta Mathematica*, 55(none):117 – 258, 1930. doi: 10.1007/BF02546511. URL <https://doi.org/10.1007/BF02546511>.
- [6] A. L. Patterson. A fourier series method for the determination of the components of interatomic distances in crystals. *Phys. Rev.*, 46:372–376, Sep 1934. doi: 10.1103/

- PhysRev.46.372. URL <https://link.aps.org/doi/10.1103/PhysRev.46.372>.
- [7] C Fienup and J Dainty. Phase retrieval and image reconstruction for astronomy. *Image recovery: theory and application*, 231:275, 1987.
- [8] R. P. Millane. Phase retrieval in crystallography and optics. *J. Opt. Soc. Am. A*, 7(3):394–411, Mar 1990. doi: 10.1364/JOSAA.7.000394. URL <https://opg.optica.org/josaa/abstract.cfm?URI=josaa-7-3-394>.
- [9] R.A. Lewis. Medical phase contrast x-ray imaging: current status and future prospects. *Physics in Medicine & Biology*, 49(16):3573, aug 2004. doi: 10.1088/0031-9155/49/16/005. URL <https://dx.doi.org/10.1088/0031-9155/49/16/005>.
- [10] L. M. Close, K. B. Follette, J. R. Males, A. Puglisi, M. Xompero, D. Apai, J. Najita, A. J. Weinberger, K. Morzinski, T. J. Rodigas, P. Hinz, V. Bailey, and R. Briguglio. Discovery of H α Emission from the Close Companion inside the Gap of Transitional Disk HD 142527. *ApJ*, 781(2):L30, February 2014. doi: 10.1088/2041-8205/781/2/L30.
- [11] A. Zurlo, A. Vigan, R. Galicher, A. L. Maire, D. Mesa, R. Gratton, G. Chauvin, M. Kasper, C. Moutou, M. Bonnefoy, S. Desidera, L. Abe, D. Apai, A. Baruffolo, P. Baudoz, J. Baudrand, J. L. Beuzit, P. Blancard, A. Boccaletti, F. Cantalloube, M. Carle, E. Cascone, J. Charton, R. U. Claudi, A. Costille, V. de Caprio, K. Dohlen, C. Dominik, D. Fantinel, P. Feautrier, M. Feldt, T. Fusco, P. Gigan, J. H. Girard, D. Gisler, L. Gluck, C. Gry, T. Henning, E. Hugot, M. Janson, M. Jaquet, A. M. Lagrange, M. Langlois, M. Llored, F. Madec, Y. Magnard, P. Martinez, D. Maurel, D. Mawet, M. R. Meyer, J. Milli, O. Moeller-Nilsson, D. Mouillet, A. Origné, A. Pavlov,

- C. Petit, P. Puget, S. P. Quanz, P. Rabou, J. Ramos, G. Rousset, A. Roux, B. Salasnich, G. Salter, J. F. Sauvage, H. M. Schmid, C. Soenke, E. Stadler, M. Suarez, M. Turatto, S. Udry, F. Vakili, Z. Wahhaj, F. Wildi, and J. Antichi. First light of the VLT planet finder SPHERE. III. New spectrophotometry and astrometry of the HR 8799 exoplanetary system. *A&A*, 587:A57, March 2016. doi: 10.1051/0004-6361/201526835.
- [12] S. Sallum, K. B. Follette, J. A. Eisner, L. M. Close, P. Hinz, K. Kratter, J. Males, A. Skemer, B. Macintosh, P. Tuthill, V. Bailey, D. Defrère, K. Morzinski, T. Rodigas, E. Spalding, A. Vaz, and A. J. Weinberger. Accreting protoplanets in the LkCa 15 transition disk. *Nature*, 527(7578):342–344, November 2015. doi: 10.1038/nature15761.
- [13] G. Chauvin, S. Desidera, A. M. Lagrange, A. Vigan, R. Gratton, M. Langlois, M. Bonnefoy, J. L. Beuzit, M. Feldt, D. Mouillet, M. Meyer, A. Cheetham, B. Biller, A. Boccaletti, V. D’Orazi, R. Galicher, J. Hagelberg, A. L. Maire, D. Mesa, J. Olofsson, M. Samland, T. O. B. Schmidt, E. Sissa, M. Bonavita, B. Charnay, M. Cudel, S. Daemgen, P. Delorme, P. Janin-Potiron, M. Janson, M. Keppler, H. Le Coroller, R. Ligi, G. D. Marleau, S. Messina, P. Mollière, C. Mordasini, A. Müller, S. Peretti, C. Perrot, L. Rodet, D. Rouan, A. Zurlo, C. Dominik, T. Henning, F. Menard, H. M. Schmid, M. Turatto, S. Udry, F. Vakili, L. Abe, J. Antichi, A. Baruffolo, P. Baudoz, J. Baudrand, P. Blanchard, A. Bazzon, T. Buey, M. Carillet, M. Carle, J. Charlton, E. Cascone, R. Claudi, A. Costille, A. Deboulbe, V. De Caprio, K. Dohlen, D. Fantinel, P. Feautrier, T. Fusco, P. Gigan, E. Giro, D. Gisler, L. Gluck, N. Hubin, E. Hugot, M. Jaquet, M. Kasper, F. Madec, Y. Magnard, P. Martinez, D. Mau-

- rel, D. Le Mignant, O. Möller-Nilsson, M. Llored, T. Moulin, A. Origné, A. Pavlov, D. Perret, C. Petit, J. Pragt, P. Puget, P. Rabou, J. Ramos, R. Rigal, S. Rochat, R. Roelfsema, G. Rousset, A. Roux, B. Salasnich, J. F. Sauvage, A. Sevin, C. Soenke, E. Stadler, M. Suarez, L. Weber, F. Wildi, S. Antoniucci, J. C. Augereau, J. L. Baudino, W. Brandner, N. Engler, J. Girard, C. Gry, Q. Kral, T. Kopytova, E. Lagadec, J. Milli, C. Moutou, J. Schlieder, J. Szulágyi, C. Thalmann, and Z. Wahhaj. Discovery of a warm, dusty giant planet around HIP 65426. *A&A*, 605:L9, September 2017. doi: 10.1051/0004-6361/201731152.
- [14] C. Ginski, T. Stolker, P. Pinilla, C. Dominik, A. Boccaletti, J. de Boer, M. Benisty, B. Biller, M. Feldt, A. Garufi, C. U. Keller, M. Kenworthy, A. L. Maire, F. Ménard, D. Mesa, J. Milli, M. Min, C. Pinte, S. P. Quanz, R. van Boekel, M. Bonnefoy, G. Chauvin, S. Desidera, R. Gratton, J. H. V. Girard, M. Keppler, T. Kopytova, A. M. Lagrange, M. Langlois, D. Rouan, and A. Vigan. Direct detection of scattered light gaps in the transitional disk around HD 97048 with VLT/SPHERE. *A&A*, 595:A112, November 2016. doi: 10.1051/0004-6361/201629265.
- [15] A. Garufi, S. P. Quanz, H. M. Schmid, G. D. Mulders, H. Avenhaus, A. Boccaletti, C. Ginski, M. Langlois, T. Stolker, J. C. Augereau, M. Benisty, B. Lopez, C. Dominik, R. Gratton, T. Henning, M. Janson, F. Ménard, M. R. Meyer, C. Pinte, E. Sissa, A. Vigan, A. Zurlo, A. Bazzon, E. Buenzli, M. Bonnefoy, W. Brandner, G. Chauvin, A. Cheetham, M. Cudel, S. Desidera, M. Feldt, R. Galicher, M. Kasper, A. M. Lagrange, J. Lannier, A. L. Maire, D. Mesa, D. Mouillet, S. Peretti, C. Perrot, G. Salter,

- and F. Wildi. The SPHERE view of the planet-forming disk around HD 100546. *A&A*, 588:A8, April 2016. doi: 10.1051/0004-6361/201527940.
- [16] Henning Avenhaus, Sascha P. Quanz, Antonio Garufi, Sebastian Perez, Simon Casasus, Christophe Pinte, Gesa H. M. Bertrang, Claudio Caceres, Myriam Benisty, and Carsten Dominik. Disks around T Tauri Stars with SPHERE (DARTTS-S). I. SPHERE/IRDIS Polarimetric Imaging of Eight Prominent T Tauri Disks. *ApJ*, 863(1):44, August 2018. doi: 10.3847/1538-4357/aab846.
- [17] S. Antoniucci, L. Podio, B. Nisini, F. Bacciotti, E. Lagadec, E. Sissa, A. La Camera, T. Giannini, H. M. Schmid, R. Gratton, M. Turatto, S. Desidera, M. Bonnefoy, G. Chauvin, C. Dougados, A. Bazzon, C. Thalmann, and M. Langlois. Sub-0.1” optical imaging of the Z CMa jets with SPHERE/ZIMPOL. *A&A*, 593:L13, September 2016. doi: 10.1051/0004-6361/201628968.
- [18] H. M. Schmid, A. Bazzon, J. Milli, R. Roelfsema, N. Engler, D. Mouillet, E. Lagadec, E. Sissa, J. F. Sauvage, C. Ginski, A. Baruffolo, J. L. Beuzit, A. Boccaletti, A. J. Bohn, R. Claudi, A. Costille, S. Desidera, K. Dohlen, C. Dominik, M. Feldt, T. Fusco, D. Gisler, J. H. Girard, R. Gratton, T. Henning, N. Hubin, F. Joos, M. Kasper, M. Langlois, A. Pavlov, J. Pragt, P. Puget, S. P. Quanz, B. Salasnich, R. Siebenmorgen, M. Stute, M. Suarez, J. Szulágyi, C. Thalmann, M. Turatto, S. Udry, A. Vigan, and F. Wildi. SPHERE/ZIMPOL observations of the symbiotic system R Aquarii. I. Imaging of the stellar binary and the innermost jet clouds. *A&A*, 602:A53, June 2017. doi: 10.1051/0004-6361/201629416.

- [19] Adrian M. Price-Whelan, David W. Hogg, Hans-Walter Rix, Nathan De Lee, Steven R. Majewski, David L. Nidever, Nicholas Troup, José G. Fernández-Trincado, Domingo A. García-Hernández, Penélope Longa-Peña, Christian Nitschelm, Jennifer Sobeck, and Olga Zamora. Binary companions of evolved stars in APOGEE DR14: Search method and catalog of \sim 5000 companions. *The Astronomical Journal*, 156(1):18, jun 2018. doi: 10.3847/1538-3881/aac387. URL <https://doi.org/10.3847/1538-3881/aac387>.
- [20] A. Bhattacharya, J. P. Beaulieu, D. P. Bennett, J. Anderson, N. Koshimoto, J. R. Lu, V. Batista, J. W. Blackman, I. A. Bond, A. Fukui, C. B. Henderson, Y. Hirao, J. B. Marquette, P. Mroz, C. Ranc, and A. Udalski. WFIRST Exoplanet Mass-measurement Method Finds a Planetary Mass of 39 ± 8 M_{\oplus} for OGLE-2012-BLG-0950Lb. *AJ*, 156(6):289, December 2018. doi: 10.3847/1538-3881/aaed46.
- [21] Klüter, J., Bastian, U., and Wambsganss, J. Expectations on mass determination using astrometric microlensing by gaia. *A&A*, 640:A83, 2020. doi: 10.1051/0004-6361/201937061. URL <https://doi.org/10.1051/0004-6361/201937061>.
- [22] Awad, P., Chan, J. H. H., Millon, M., Courbin, F., and Paic, E. Probing compact dark matter objects with microlensing in gravitationally lensed quasars. *A&A*, 673: A88, 2023. doi: 10.1051/0004-6361/202245615. URL <https://doi.org/10.1051/0004-6361/202245615>.
- [23] A. Labeyrie. Attainment of diffraction limited resolution in large telescopes by Fourier analysing speckle patterns in star images. *A&A*, 6:85L, January 1970.
- [24] Nicholas J. Scott. The current state of speckle imaging. In *Optical and Infrared Interfer-*

- ometry and Imaging VI*, volume 10701 of *Society of Photo-Optical Instrumentation Engineers (SPIE) Conference Series*, page 1070112, July 2018. doi: 10.1117/12.2314553.
- [25] Douglas Hope, Stuart Jefferies, Gianluca Li Causi, Marco Stangalini, Fernando Pedichini, Massimiliano Mattioli, Simone Antonucci, Vincenzo Testa, and Robert Piazzesi. High-Resolution Imaging of Closely Space Objects with High Contrast Ratios. In *Proceedings of the Advanced Maui Optical and Space Surveillance Technologies Conference*, page 3, September 2019.
- [26] K. T. Knox and B. J. Thompson. Recovery of images from atmospherically degraded short-exposure images. *ApJ*, 193:L45–L48, October 1974.
- [27] A. W. Lohmann, G. Weigelt, and B. Wirnitzer. Speckle masking in astronomy: triple correlation theory and applications. *Appl. Opt.*, 22:4028–4037, December 1983. doi: 10.1364/AO.22.004028.
- [28] Charles L. Matson. A comparison of multi-frame blind deconvolution and speckle imaging energy spectrum signal-to-noise ratios. In Anton Kohnle, Karin Stein, and John D. Ginglewski, editors, *Optics in Atmospheric Propagation and Adaptive Systems XI*, volume 7108, pages 178 – 189. International Society for Optics and Photonics, SPIE, 2008. doi: 10.1117/12.801240. URL <https://doi.org/10.1117/12.801240>.
- [29] R. A. Gonsalves. Phase Retrieval And Diversity In Adaptive Optics. *Optical Engineering*, 21(5):829, October 1982. doi: 10.1117/12.7972989.
- [30] Harry R. Ingleby and Donald R. McGaughey. Real data results with wavelength-diverse blind deconvolution. *Optics Letters*, 30(5):489–491, March 2005. doi: 10.1364/

OL.30.000489.

- [31] Donald McGaughey and Mario Ivanov. Correcting phase distorted images using aperture diversity. In *Adaptive Optics: Analysis and Methods/Computational Optical Sensing and Imaging/Information Photonics/Signal Recovery and Synthesis Topical Meetings on CD-ROM*, page JTxA8. Optical Society of America, 2007. doi: 10.1364/SRS.2007.JTxA8. URL <http://www.osapublishing.org/abstract.cfm?URI=SRS-2007-JTxA8>.
- [32] Douglas A. Hope, Stuart M. Jefferies, Michael Hart, and James G. Nagy. High-resolution speckle imaging through strong atmospheric turbulence. *Optics Express*, 24(11):12116, May 2016. doi: 10.1364/OE.24.012116.
- [33] Laurent M. Mugnier, Clélia Robert, Jean-Marc Conan, Vincent Michau, and Sélim Salem. Myopic deconvolution from wave-front sensing. *J. Opt. Soc. Am. A*, 18(4):862–872, April 2001. doi: 10.1364/JOSAA.18.000862. URL <http://josaa.osa.org/abstract.cfm?URI=josaa-18-4-862>.
- [34] F Roddier, J M Gilli, and J Vernin. On the isoplanatic patch size in stellar speckle interferometry. *Journal of Optics*, 13(2):63, mar 1982. doi: 10.1088/0150-536X/13/2/002. URL <https://dx.doi.org/10.1088/0150-536X/13/2/002>.
- [35] J. W. Goodman. *Introduction To Fourier Optics, 4th Edition*. McGraw-Hill Science, 4th edition, January 2017. ISBN 0974707724.
- [36] G. R. Ayers and J. C. Dainty. Iterative blind deconvolution method and its applications. *Opt. Lett.*, 13(7):547–549, Jul 1988. doi: 10.1364/OL.13.000547. URL

<http://ol.osa.org/abstract.cfm?URI=ol-13-7-547>.

- [37] J. Primot, G. Rousset, and J. C. Fontanella. Deconvolution from wave-front sensing: a new technique for compensating turbulence-degraded images. *J. Opt. Soc. Am. A*, 7(9):1598–1608, Sep 1990. doi: 10.1364/JOSAA.7.001598. URL <http://josaa.osa.org/abstract.cfm?URI=josaa-7-9-1598>.
- [38] Brian J. Thelen, Richard G. Paxman, David A. Carrara, and John H. Seldin. Overcoming turbulence-induced space-variant blur by using phase-diverse speckle. *J. Opt. Soc. Am. A*, 26(1):206–218, Jan 2009. doi: 10.1364/JOSAA.26.000206. URL <http://josaa.osa.org/abstract.cfm?URI=josaa-26-1-206>.
- [39] Richard G. Paxman, Timothy J. Rogne, Brett A. Sickmiller, Daniel A. LeMaster, Jason J. Miller, and Candice G. Vollweiler. Spatial stabilization of deep-turbulence-induced anisoplanatic blur. *Opt. Express*, 24(25):29109–29125, Dec 2016. doi: 10.1364/OE.24.029109. URL <http://www.opticsexpress.org/abstract.cfm?URI=oe-24-25-29109>.
- [40] Johnathan Bardsley, Stuart Jefferies, James Nagy, and Robert Plemmons. A computational method for the restoration of images with an unknown, spatially-varying blur. *Optics express*, 14:1767–82, 04 2006. doi: 10.1364/OE.14.001767.
- [41] James G. Nagy and Dianne P. O’Leary. Restoring images degraded by spatially variant blur. *SIAM Journal on Scientific Computing*, 19(4):1063–1082, 1998. doi: 10.1137/S106482759528507X. URL <https://doi.org/10.1137/S106482759528507X>.
- [42] Nicholas J. Scott. NESSI and ‘Alopeke: Two new dual-channel speckle imaging in-

- struments. In *American Astronomical Society Meeting Abstracts #231*, volume 231 of *American Astronomical Society Meeting Abstracts*, page 361.16, January 2018.
- [43] Stuart M. Jefferies and Julian C. Christou. Restoration of Astronomical Images by Iterative Blind Deconvolution. *ApJ*, 415:862, October 1993. doi: 10.1086/173208.
- [44] T. J. Schulz. Multiframe blind deconvolution of astronomical images. *Journal of the Optical Society of America A*, 10(5):1064–1073, May 1993. doi: 10.1364/JOSAA.10.001064.
- [45] Darryl P. Greenwood. Bandwidth specification for adaptive optics systems*. *J. Opt. Soc. Am.*, 67(3):390–393, Mar 1977. doi: 10.1364/JOSA.67.000390. URL <https://opg.optica.org/abstract.cfm?URI=josa-67-3-390>.
- [46] G. I. Taylor. The spectrum of turbulence. *Proc. R. Soc. Lond.*, 164(919):476–490, 1938. URL <https://doi.org/10.1098/rspa.1938.0032>.
- [47] Stuart M. Jefferies and Michael Hart. Deconvolution from wave front sensing using the frozen flow hypothesis. *Opt. Express*, 19(3):1975–1984, January 2011. doi: 10.1364/OE.19.001975. URL <http://www.opticsexpress.org/abstract.cfm?URI=oe-19-3-1975>.
- [48] Steve B. Howell, Arturo O. Martinez, Douglas A. Hope, David R. Ciardi, Stuart M. Jefferies, Fabien R. Baron, and Michael B. Lund. High-contrast, high-angular-resolution optical speckle imaging: Uncovering hidden stellar companions. *The Astronomical Journal*, 167(6):258, may 2024. doi: 10.3847/1538-3881/ad3df2. URL <https://dx.doi.org/10.3847/1538-3881/ad3df2>.

- [49] Lisa A. Poyneer. Scene-based shack-hartmann wave-front sensing: analysis and simulation. *Appl. Opt.*, 42(29):5807–5815, Oct 2003. doi: 10.1364/AO.42.005807. URL <http://ao.osa.org/abstract.cfm?URI=ao-42-29-5807>.
- [50] B. C. Platt and R. Shack. History and principles of Shack–Hartmann wavefront sensing. *J. Refractive Surg.*, 17:S573–S577, Sept 2001. doi: 10.3928/1081-597X-20010901-13.
- [51] R. K. Tyson. *Principles of Adaptive Optics*. CRC Press, December 2016. ISBN 9780367870485.
- [52] S. Thomas, T. Fusco, A. Tokovinin, M. Nicolle, V. Michau, and G. Rousset. Comparison of centroid computation algorithms in a shack–hartmann sensor. *Monthly Notices of the Royal Astronomical Society*, 371(1):323–336, 2006. doi: <https://doi.org/10.1111/j.1365-2966.2006.10661.x>. URL <https://onlinelibrary.wiley.com/doi/abs/10.1111/j.1365-2966.2006.10661.x>.
- [53] Thomas R. Rimmele and Jose Marino. Solar Adaptive Optics. *Living Reviews in Solar Physics*, 8(2):2, June 2011. doi: 10.12942/lrsp-2011-2.
- [54] Mathieu Aubailly and Mikhail A. Vorontsov. Scintillation resistant wavefront sensing based on multi-aperture phase reconstruction technique. *J. Opt. Soc. Am. A*, 29(8):1707–1716, Aug 2012. doi: 10.1364/JOSAA.29.001707. URL <http://josaa.osa.org/abstract.cfm?URI=josaa-29-8-1707>.
- [55] A. Polo, N. van Marrewijk, S. F. Pereira, and H. P. Urbach. Subaperture phase reconstruction from a Hartmann wavefront sensor by phase retrieval method for application in EUV adaptive optics. In Patrick P. Naulleau and Obert R. Wood II, editors,

- Extreme Ultraviolet (EUV) Lithography III*, volume 8322, pages 386 – 394. International Society for Optics and Photonics, SPIE, 2012. doi: 10.1117/12.916154. URL <https://doi.org/10.1117/12.916154>.
- [56] Brian Kern, Ted A. Laurence, Chris Martin, and Paul E. Dimotakis. Temporal coherence of individual turbulent patterns in atmospheric seeing. *Appl. Opt.*, 39(27):4879–4885, Sep 2000. doi: 10.1364/AO.39.004879. URL <http://ao.osa.org/abstract.cfm?URI=ao-39-27-4879>.
- [57] Nazim Ali Bharmal. Frozen flow or not? investigating the predictability of the atmosphere. *Journal of Physics: Conference Series*, 595:012003, apr 2015. doi: 10.1088/1742-6596/595/1/012003. URL <https://doi.org/10.1088/1742-6596/595/1/012003>.
- [58] Qing Chu, Stuart Jefferies, and James G. Nagy. Iterative wavefront reconstruction for astronomical imaging. *SIAM Journal on Scientific Computing*, 35(5):S84–S103, 2013. doi: 10.1137/120882603. URL <https://doi.org/10.1137/120882603>.
- [59] J. Vernin and F. Roddier. Experimental determination of two-dimensional spatiotemporal power spectra of stellar light scintillation evidence for a multilayer structure of the air turbulence in the upper troposphere. *J. Opt. Soc. Am.*, 63(3):270–273, Mar 1973. doi: 10.1364/JOSA.63.000270. URL <http://www.osapublishing.org/abstract.cfm?URI=josa-63-3-270>.
- [60] Noriaki Miura, Ayumu Oh-ishi, Susumu Kuwamura, Naoshi Baba, Satoru Ueno, and Kiyoshi Ichimoto. Application of solar scidar technique to measuring wind velocity. In

- Imaging and Applied Optics*, page JTU4A.6. Optical Society of America, 2013. URL <http://www.osapublishing.org/abstract.cfm?URI=QMI-2013-JTu4A.6>.
- [61] R. W. Wilson. SLODAR: measuring optical turbulence altitude with a Shack–Hartmann wavefront sensor. *Monthly Notices of the Royal Astronomical Society*, 337(1):103–108, 11 2002. ISSN 0035-8711. doi: 10.1046/j.1365-8711.2002.05847.x. URL <https://doi.org/10.1046/j.1365-8711.2002.05847.x>.
- [62] Michael Hart, Stuart Jefferies, and Douglas Hope. Tomographic wave-front sensing with a single guide star. In Jean J. Dolne, Thomas J. Karr, and David C. Dayton, editors, *Unconventional Imaging and Wavefront Sensing XII*, volume 9982, page 998207. International Society for Optics and Photonics, SPIE, 2016. doi: 10.1117/12.2257358. URL <https://doi.org/10.1117/12.2257358>.
- [63] Matthew Willson, Stuart Jefferies, and Douglas Hope. Tomographic Wave Front Sensing using an Imaging Shack-Hartmann Wave Front Sensor and Multi-Frame Blind Deconvolution. In *The Advanced Maui Optical and Space Surveillance Technologies Conference*, page 70, September 2018.
- [64] J. Fienup. Fourier modulus image construction. Final Technical Report, 7 Sep. 1979 - 30 Sep. 1980 Environmental Research Inst. of Michigan, Ann Arbor. Radar and Optics Div., May 1981.
- [65] David L. Fried. Probability of getting a lucky short-exposure image through turbulence*. *J. Opt. Soc. Am.*, 68(12):1651–1658, Dec 1978. doi: 10.1364/JOSA.68.001651. URL <https://opg.optica.org/abstract.cfm?URI=josa-68-12-1651>.

- [66] Michael Hirsch, Suvrit Sra, Bernhard Schölkopf, and Stefan Harmeling. Efficient filter flow for space-variant multiframe blind deconvolution. In *2010 IEEE Computer Society Conference on Computer Vision and Pattern Recognition*, pages 607–614, 2010. doi: 10.1109/CVPR.2010.5540158.
- [67] Kathryn E Hartley, Oliver J D Farley, Matthew J Townson, James Osborn, and R W Wilson. First on-sky demonstration of a scintillation correction technique using tomographic wavefront sensing. *Monthly Notices of the Royal Astronomical Society*, 520(3):4134–4146, 02 2023. ISSN 0035-8711. doi: 10.1093/mnras/stad420. URL <https://doi.org/10.1093/mnras/stad420>.
- [68] Lewis C. Roberts and L. William Bradford. Improved models of upper-level wind for several astronomical observatories. *Opt. Express*, 19(2):820–837, Jan 2011. doi: 10.1364/OE.19.000820. URL <https://opg.optica.org/oe/abstract.cfm?URI=oe-19-2-820>.
- [69] Zhou Wang, A.C. Bovik, H.R. Sheikh, and E.P. Simoncelli. Image quality assessment: from error visibility to structural similarity. *IEEE Transactions on Image Processing*, 13(4):600–612, 2004. doi: 10.1109/TIP.2003.819861.
- [70] Allison H. Baker, Alexander Pinard, and Dorit M. Hammerling. DSSIM: a structural similarity index for floating-point data. *arXiv e-prints*, art. arXiv:2202.02616, February 2022. doi: 10.48550/arXiv.2202.02616.
- [71] Stuart M. Jefferies, Michael Lloyd-Hart, E. Keith Hege, and James Georges. Sensing wave-front amplitude and phase with phase diversity. *Appl. Opt.*, 41(11):2095–2102,

- Apr 2002. doi: 10.1364/AO.41.002095. URL <http://ao.osa.org/abstract.cfm?URI=ao-41-11-2095>.
- [72] A. Berdja and J. Borgnino. Modelling the optical turbulence boiling and its effect on finite-exposure differential image motion. *Monthly Notices of the Royal Astronomical Society*, 378(3):1177–1186, 06 2007. ISSN 0035-8711. doi: 10.1111/j.1365-2966.2007.11853.x. URL <https://doi.org/10.1111/j.1365-2966.2007.11853.x>.
- [73] Daniel Gabay and Bertrand Mercier. A dual algorithm for the solution of nonlinear variational problems via finite element approximation. *Computers & Mathematics with Applications*, 2(1):17–40, 1976. ISSN 0898-1221. doi: [https://doi.org/10.1016/0898-1221\(76\)90003-1](https://doi.org/10.1016/0898-1221(76)90003-1). URL <https://www.sciencedirect.com/science/article/pii/0898122176900031>.
- [74] Fred Moolekamp and Peter Melchior. Block-Simultaneous Direction Method of Multipliers: A proximal primal-dual splitting algorithm for nonconvex problems with multiple constraints. *arXiv e-prints*, art. arXiv:1708.09066, August 2017. doi: 10.48550/arXiv.1708.09066.
- [75] Daniel P. Engelhart, Elena A. Plis, Dale Ferguson, W. Robert Johnston, Russell Cooper, and Ryan C. Hoffmann. Space plasma interactions with spacecraft materials. In Haikel Jelassi and Djamel Benredjem, editors, *Plasma Science and Technology*, chapter 12. IntechOpen, Rijeka, 2018. doi: 10.5772/intechopen.78306. URL <https://doi.org/10.5772/intechopen.78306>.
- [76] Elena Plis, Miles T. Bengtson, Daniel P. Engelhart, Gregory Badura, Heather Cow-

- ardin, Ryan C. Hoffmann, Alexey Sokolovskiy, Jacqueline Reyes, Dale C. Ferguson, Jainisha Shah, Sydney Collman, and Timothy Scott. Spacecraft materials degradation under space-simulated low earth orbit (leo) environment. In *AIAA SCITECH 2023 Forum*, 2023. doi: 10.2514/6.2023-1956. URL <https://arc.aiaa.org/doi/abs/10.2514/6.2023-1956>.
- [77] Kim K. Degroh, Bruce A. Banks, Joyce A. Dever, Donald A. Jaworske, Sharon K.R. Miller, Edward A. Seckar, and Scott R. Panko. Nasa glenn research center's materials international space station experiments (misce 1-7). Technical report, NASA Glenn Research Center, 2008. URL <https://api.semanticscholar.org/CorpusID:108024209>.
- [78] Elena A. Plis, Daniel P. Engelhart, Russell Cooper, Dale C. Ferguson, and Ryan Hoffmann. Effect of environment on charge transport properties of polyimide films damaged by high-energy electron radiation. *Journal of Vacuum Science & Technology B*, 36(5):052906, 09 2018. ISSN 2166-2746. doi: 10.1116/1.5044184. URL <https://doi.org/10.1116/1.5044184>.
- [79] I. Robinson and A. Klier. Wideband Hyperspectral Imaging for Space Situational Awareness. In S. Ryan, editor, *The Advanced Maui Optical and Space Surveillance Technologies Conference*, page E25, January 2006.
- [80] Harrison Krantz, Eric Pearce, Louis Avner, and Kris Rockowitz. Chimera: A High-Speed Three-Color Photometer for Satellite Characterization. In S. Ryan, editor, *The Advanced Maui Optical and Space Surveillance Technologies Conference*, page 19,

September 2018.

- [81] Eric Pearce, Benjamin Weiner, Adam Block, Harrison Krantz, Kris Rockowitz, Brad Sease, Greg Hennessy, and Michelle Wilson. Examining the Effects of On-Orbit Aging of SL-12 Rocket Bodies using Visible Band Spectra with the MMT Telescope and 5-Color Photometry with the UKIRT/WFCAM. In S. Ryan, editor, *Advanced Maui Optical and Space Surveillance Technologies Conference*, page 69, September 2019.
- [82] Nathan Hagen and Michael W. Kudenov. Review of snapshot spectral imaging technologies. *Optical Engineering*, 52:090901, September 2013. doi: 10.1117/1.OE.52.9.090901.
- [83] Ryan Hall and Stuart M. Jefferies. Hyper-Spectral Speckle Imaging for Space Situational Awareness. *Journal of the Astronautical Sciences*, 69(2):581–592, April 2022. doi: 10.1007/s40295-022-00306-2.
- [84] F. Baron, S.M. Jefferies, D. Shcherbik, R. Hall, D. Johns, and D. Hope. Hyper-Spectral Speckle Imaging of Resolved Targets. In S. Ryan, editor, *Proceedings of the Advanced Maui Optical and Space Surveillance (AMOS) Technologies Conference*, page 46, September 2023.
- [85] L. W. Bradford. Maui4: a 24 hour Haleakala turbulence profile. In *The Advanced Maui Optical and Space Surveillance Technologies Conference*, 2010.
- [86] Benjamin L. McGlamery. Computer Simulation Studies Of Compensation Of Turbulence Degraded Images. In John C. Urbach, editor, *Image Processing*, volume 0074, pages 225 – 233. International Society for Optics and Photonics, SPIE, 1976. doi:

- 10.1117/12.954724. URL <https://doi.org/10.1117/12.954724>.
- [87] Lewis C. Roberts and L. William Bradford. Improved models of upper-level wind for several astronomical observatories. *Opt. Express*, 19(2):820–837, Jan 2011. doi: 10.1364/OE.19.000820. URL <https://opg.optica.org/oe/abstract.cfm?URI=oe-19-2-820>.
 - [88] Noah Van Zandt, Jack McCrae, Mark Spencer, Michael Steinbock, Milo Hyde, and Steven Fiorino. Polychromatic wave-optics models for image-plane speckle. 1. well-resolved objects. *Applied Optics*, 57:4090–4102, 05 2018. doi: 10.1364/AO.57.004090.
 - [89] D. Johns, D. Hope, S.M. Jefferies, F. Baron, and D. Shcherbik. Performance of an Imaging Shack-HartmannWavefront Sensor for Space Domain Awareness Observations. In S. Ryan, editor, *Proceedings of the Advanced Maui Optical and Space Surveillance (AMOS) Technologies Conference*, page 120, September 2023.
 - [90] B. Calef. Private Communication, 2024.
 - [91] Andrew Hind and Marcus Schulz. Measuring the optical properties of photovoltaic cells using the agilent cary 5000 uv-vis-nir spectrophotometer and the external dra-2500, March 2011.
 - [92] Miles Bengtson, Jordan Maxwell, Ryan Hoffmann, Russell Cooper, Stephanie Schieffer, Dale Ferguson, W. Robert Johnston, Heather Cowardin, Elena Plis, and Daniel Engelhart. Optical Characterization of Commonly Used Thermal Control Paints in a Simulated GEO Environment. In S. Ryan, editor, *The Advanced Maui Optical and Space Surveillance Technologies Conference*, page 33, September 2018.

- [93] Jaeheung Park, Kyoung Wook Min, Hoonkyu Seo, Eo-Jin Kim, Kwangsun Ryu, Jongdae Sohn, Jongho Seon, Ji-Hyeon Yoo, Seunguk Lee, Brian Kress, Junchan Lee, Changho Woo, and Dae-Young Lee. Multi-year statistics of leo energetic electrons as observed by the korean nextsat-1. *Space Weather*, 19(8):e2021SW002787, 2021. doi: <https://doi.org/10.1029/2021SW002787>. URL <https://agupubs.onlinelibrary.wiley.com/doi/abs/10.1029/2021SW002787>. e2021SW002787 2021SW002787.
- [94] C. D. Coleman, W. R. Bozman, and W. F. Meggers. Table of wavelnumbers: 7000 a to 1000 μ . Technical report, U.S. Department of Commerce, National Bureau of Standards, 1960.
- [95] A. V. Filippenko. The importance of atmospheric differential refraction in spectrophotometry. *Publications of the Astronomical Society of the Pacific*, 94:715–721, August 1982. doi: 10.1086/131052.
- [96] G. I. Taylor. The spectrum of turbulence. *Proc. R. Soc. Lond.*, 164(919):476–490, 1938. URL <https://doi.org/10.1098/rspa.1938.0032>.
- [97] Stuart M. Jefferies and Julian C. Christou. Restoration of Astronomical Images by Iterative Blind Deconvolution. *The Astrophysical Journal*, 415:862, October 1993. doi: 10.1086/173208.
- [98] Timothy J. Schulz. Multiframe blind deconvolution of astronomical images. *J. Opt. Soc. Am. A*, 10(5):1064–1073, May 1993. doi: 10.1364/JOSAA.10.001064. URL <https://opg.optica.org/josaa/abstract.cfm?URI=josaa-10-5-1064>.
- [99] J. Mason, M. Bold, and J. Wirth. Simultaneous Track and Multi-Spectral Instrument

- for Satellite Identification. In S. Ryan, editor, *Proceedings of the Advanced Maui Optical and Space Surveillance (AMOS) Technologies Conference*, page 138, September 2023.
- [100] L. B. Lucy. Statistical Limits to Super Resolution. *Astronomy & Astrophysics*, 261: 706, August 1992.
- [101] Stuart M. Jefferies and Michael Hart. Deconvolution from wave front sensing using the frozen flow hypothesis. *Opt. Express*, 19(3):1975–1984, Jan 2011. doi: 10.1364/OE.19.001975. URL <https://opg.optica.org/oe/abstract.cfm?URI=oe-19-3-1975>.
- [102] Douglas A. Hope, Stuart M. Jefferies, Michael Hart, and James G. Nagy. High-resolution speckle imaging through strong atmospheric turbulence. *Opt. Express*, 24(11):12116–12129, May 2016. doi: 10.1364/OE.24.012116. URL <https://opg.optica.org/oe/abstract.cfm?URI=oe-24-11-12116>.
- [103] S.M. Jefferies, A. Knox, A. Dhada, C. Abbott, and D. Hope. Dynamic Aperture Diversity. In S. Ryan, editor, *Advanced Maui Optical and Space Surveillance (AMOS) Technologies Conference*, page 92, January 2017.
- [104] Eric P. Magee and Byron M. Welsh. Characterization of laboratory-generated turbulence by optical phase measurements. In Soyoung S. Cha and James D. Trolinger, editors, *Optical Diagnostics in Fluid and Thermal Flow*, volume 2005 of *Society of Photo-Optical Instrumentation Engineers (SPIE) Conference Series*, pages 50–61, December 1993. doi: 10.1117/12.163751.
- [105] Sandrine Thomas. A simple turbulence simulator for adaptive optics. In Domenico Bonaccini Calia, Brent L. Ellerbroek, and Roberto Ragazzoni, editors, *Advancements*

- in Adaptive Optics*, volume 5490 of *Society of Photo-Optical Instrumentation Engineers (SPIE) Conference Series*, pages 766–773, October 2004. doi: 10.1117/12.549858.
- [106] Stefan Hippler, Felix Hormuth, David J. Butler, Wolfgang Brandner, and Thomas Henning. Atmosphere-like turbulence generation with surface-etched phase-screens. *Opt. Express*, 14(22):10139–10148, Oct 2006. doi: 10.1364/OE.14.010139. URL <https://opg.optica.org/oe/abstract.cfm?URI=oe-14-22-10139>.
- [107] A. Kolmogorov. The Local Structure of Turbulence in Incompressible Viscous Fluid for Very Large Reynolds' Numbers. *Akademiia Nauk SSSR Doklady*, 30:301–305, January 1941.
- [108] Samuel V. Mantravadi, Troy A. Rhoadarmer, and Robert S. Glas. Simple laboratory system for generating well-controlled atmospheric-like turbulence. In John D. Ginglewski, Mark T. Gruneisen, and Michael K. Giles, editors, *Advanced Wavefront Control: Methods, Devices, and Applications II*, volume 5553, pages 290 – 300. International Society for Optics and Photonics, SPIE, 2004. doi: 10.1117/12.559933. URL <https://doi.org/10.1117/12.559933>.
- [109] David C. Dayton and Mark F. Spencer. Scaled-laboratory demonstrations of deep-turbulence conditions. *Appl. Opt.*, 63(16):E54–E63, Jun 2024. doi: 10.1364/AO.520208. URL <https://opg.optica.org/ao/abstract.cfm?URI=ao-63-16-E54>.
- [110] Irwin Sobel. An isotropic 3x3 image gradient operator. *Presentation at Stanford A.I. Project 1968*, 02 2014.
- [111] Pei-Guang Zhang, Chengliang Yang, Xu Zihao, Zhaoliang Cao, Quanquan Mu, and

- li Xuan. High-accuracy wavefront sensing by phase diversity technique with bisymmetric defocuses diversity phase. *Scientific Reports*, 7, 11 2017. doi: 10.1038/s41598-017-15597-x.
- [112] Z. Wang, A. C. Bovik, H. R. Sheikh, and E. P. Simoncelli. Image Quality Assessment: From Error Visibility to Structural Similarity. *IEEE Transactions on Image Processing*, 13(4):600–612, April 2004. doi: 10.1109/TIP.2003.819861.
- [113] L. Seifert, J. Liesener, and H.J. Tiziani. The adaptive shack-hartmann sensor. *Optics Communications*, 216(4):313–319, 2003. ISSN 0030-4018. doi: [https://doi.org/10.1016/S0030-4018\(02\)02351-9](https://doi.org/10.1016/S0030-4018(02)02351-9). URL <https://www.sciencedirect.com/science/article/pii/S0030401802023519>.
- [114] Jan Liesener, Lars Seifert, Hans J. Tiziani, and Wolfgang Osten. Active wavefront sensing and wavefront control with SLMs. In Wolfgang Osten and Erik Novak, editors, *Interferometry XII: Applications*, volume 5532, pages 147 – 158. International Society for Optics and Photonics, SPIE, 2004. doi: 10.1117/12.558689. URL <https://doi.org/10.1117/12.558689>.
- [115] Daniel Lechner, Andreas Zepp, Marc Eichhorn, and Szymon Gladysz. Adaptable shack-hartmann wavefront sensor with diffractive lenslet arrays to mitigate the effects of scintillation. *Opt. Express*, 28(24):36188–36205, Nov 2020. doi: 10.1364/OE.410217. URL <https://opg.optica.org/oe/abstract.cfm?URI=oe-28-24-36188>.
- [116] Megan Birch, Leticia Garcíá Varela, and Fabien Baron. A Benchtop Simulator for Evaluating Astronomical Observations with Object Generation and Point Spread Function

Engineering. In *The Advanced Maui Optical and Space Surveillance Technologies Conference*, 2024.

- [117] R. K. Piña and R. C. Puetter. Incorporation of Spatial Information in Bayesian Image Reconstruction: The Maximum Residual Likelihood Criterion. *PASP*, 104:1096, November 1992. doi: 10.1086/133095.
- [118] A. Tokovinin, R. Cantarutti, R. Tighe, P. Schurter, N. van der Bliek, M. Martinez, and E. Mondaca. High-Resolution Imaging at the SOAR Telescope. *PASP*, 122(898):1483, December 2010. doi: 10.1086/657903.
- [119] Donald Gavel and Andrew Norton. Woofer-tweeter deformable mirror control for closed-loop adaptive optics: theory and practice. In Enrico Marchetti, Laird M. Close, and Jean-Pierre Vran, editors, *Adaptive Optics Systems IV*, volume 9148 of *Society of Photo-Optical Instrumentation Engineers (SPIE) Conference Series*, page 91484J, August 2014. doi: 10.1117/12.2056937.